NASA-CR-196122

Technical Report # 5-32753
Contract Number NAS8-38609
Delivery Order No. 6

P- 197

Spray Combustion Model Improvement Study -- I (5-32753)

Final Technical Report for the Period
11 September 1991 through 11 December 1991

March 1993

Prepared by:

C. P. Chen *
Y. M. Kim
H. M. Shang
* Authors listed alphabetically

Prepared for:

NASA Marshall Space Flight Center
Attn: Klause Gross
Propulsion Laboratory
Marshall Space Flight Center, AL 32512

(NASA-CR-196122) SPRAY COMBUSTION MODEL IMPROVEMENT STUDY, 1 Final Technical Report, 11 Sep. - 11 Dec. 1991 (Alabama Univ.) 197 p

N94-37250

Unclas

G3/25 0014090

Contents

List of Figures

List of Tables

List of Symbols

a	radius of liquid jet or blob
B_0, B_1	breakup model constants
B_m	mass transfer number
B_t	heat transfer number
C_1, C_2, C_μ	turbulence model constants
C_p	heat capacity of gas
$C_{p,d}$	heat capacity of droplet
C_D	drag coefficient
d_p	droplet diameter
D	diffusion coefficient in Fick's law
Fb_i	particle body force
g	gravity
G	generation term in $k-\epsilon$ equations
h_l	fuel enthalpy
H	mean enthalpy of gas phase
H_{com}	fuel vapor combustion heat
H_t	total gas enthalpy
k	turbulent kinetic energy

K	undersampling correction factor or gas thermal conductivity
l_e	eddy length scale
L	latent heat of droplet vaporization
$\dot{m}_{ev}$	droplet evaporation rate
N_p	number of droplets for each computational particle p
NP	number of computational particles
Nu	Nusselt number
P	mean pressure or cumulative probability
Pr_t	turbulent Prandtl number
r_p	droplet radius
R_{che}	chemically controlled reaction rate
R_{fu}	fuel reaction rate [$= \min(R_{mix}, R_{che})$]
R_{mix}	mixing controlled reaction rate
R_{pi}	particle-gas momentum interaction splitting term
Re_p	particle Renolds number
s	stoichiometric ratio
S	source terms
S_p	particle-gas momentum interaction splitting term
Sc_t	turbulent Schmidt number
Sh	Sherwood number
SMD	Sauter mean diameter
SMR	Sauter mean radius
t	time
t_d	particle time scale in modulation model

t_e	eddy life time
t_{int}	particle-eddy interaction time
t_l	eddy time scale in modulation model
t_{per}	turbulence persistence time
t_{tr}	particle transition time in eddy
T	gas temperature
T_{cr}	droplet critical temperature
T_d	droplet temperature
u_i	instantaneous gas velocity component in i-direction
U_i	mean gas velocity component in i-direction
v_i	instantaneos droplet velocity component in i-direction
W	molecular weight or gas velocity at z-direction
We	droplet Weber number
x	coordinate in the streamwise direction
y	coordinate normal to the streamwise direction or droplet distortion parameter in TAB breakup model
Y	mass fraction

Greek Letters

δ_{ij}	Kronecker delta tensor
δt_{ev}	droplet evaporation sub time-step

ρ	density of gases
ρ_f	fuel vapor density
ρ_d	droplet density
ν	collision frequency in collision model
μ	viscosity
μ_t	turbulent eddy viscosity
ϕ	instantaneous scalar for gases
ϵ	turbulent energy dissipation rate
τ	particle relaxation time
τ_b	droplet breakup time
σ	standard deviation of PDF
Λ	wavelength of fastest growing rate
Ω	maximum wave growth rate

Subscripts

$()_f$	fuel
$()_g$	gas phase
$()_i$	time step index in an eddy or index for tensor
$()_k$	eddy index
$()_l$	liquid phase
$()_o$	oxidizer

$()_p$	particle or parcel
$()_{pr}$	product
$()_{rms}$	root mean square
$()_s$	droplet surface condition
$()_t$	turbulent
$()_\infty$	ambient condition

Superscripts

$\overline{()}$	density-averaged
$()'$	fluctuating
$()^*$	intermediate field at predictor stage
$()^{**}$	intermediate field at first corrector stage
$()^{***}$	intermediate field at second corrector stage

I

ABSTRACT

Under the NASA Contract NAS8-38609,D.O.6, which is the first year effort of the current model improvement efforts for predicting spary combustion processes in liquid-fueled rockets, four major tasks including atomization models, PDF droplet dispersion models, coalescence and breakup models, as well as dense-spray turbulence modulation effects have been incorporated into the CFD code MAST (Multiphase All-Speed Transient program).

The atomization model implemented is the "blob injection" model of Reitz involving secondary breakup mechanism. Two breakup models using the Taylor Analogy Breakup (TAB) concept and a wave instability concept were compared with simultaneous incorporation of an existing stochastic collision-coalescence model. Two dense modulation models based on the continuum approach of Chen and Fashola, and the stochastic approach of the Los Alamos group were also implemented and compared. To improve the computational efficiency, a parcel probability dense function(PDF) tracking method accounting for the dispersion within the numerical particles was improved and implemented.

Detailed formulations as well as validation studies are described in this report.

II

Governing Equations and Physical Models

II.1 Introduction

In this Chapter, all governing equations used to describe the spray combustions are presented. The gas-phase and liquid-phase processes are modeled by a system of unsteady, two-dimensional (axisymmetric) equations. The gas-phase equations are written in an Eulerian coordinate whereas the liquid-phase is presented in Lagrangian coordinates. The two-way coupling between the two phases is described by the interaction source terms which represent the rates of momentum, mass and heat exchange. A two-equation $k - \epsilon$ turbulence model with particle modulation effect is used to characterize the gas phase flow properties. Particle motion equation is the simplified B-B-O equation. Poly dispersed particle dynamics and particle turbulent dispersion are modelled using a Mote Carlo method. Parcel PDF model is used to improve computational efficiency. Droplet evaporation and heat transfer are calculated using Frossling correlation and Ranz-Marshall correlation respectively. A turbulent diffusion flame and single step chemical reaction model is used for spray combustion. Dense spray effects are accounted for by droplet breakup and collision models.

II.2 Gas Phase Equations

II.2.1 Mean Flow Equation

The density-weighted conservation equations of mass, momentum, energy and mass fraction variables in an Eulerian coordinate can be written as followings:

$$\frac{\partial \rho}{\partial t} + \frac{\partial}{\partial x_i}(\rho U_i) = S_{m,l} \tag{II.1}$$

$$\frac{\partial \rho U_i}{\partial t} + \frac{\partial}{\partial x_j}(\rho U_j U_i) = -\frac{\partial P}{\partial x_i} - \frac{\partial \tau_{ij}}{\partial x_j} + S_{u_i} + S_{u_i,l} \tag{II.2}$$

$$\frac{\partial \rho H_t}{\partial t} + \frac{\partial}{\partial x_j}(\rho U_j H_t) = \frac{\partial P}{\partial t} - \frac{\partial Q_j}{\partial x_j} + S_h + S_{h,l} + R_{fu} H_{com} \tag{II.3}$$

$$\frac{\partial \rho Y_f}{\partial t} + \frac{\partial}{\partial x_j}(\rho U_j Y_f) = -\frac{\partial N_{f,j}}{\partial x_j} + S_{m,l} - R_{fu} \tag{II.4}$$

$$\frac{\partial \rho Y_{o_2}}{\partial t} + \frac{\partial}{\partial x_j}(\rho U_j Y_{o_2}) = -\frac{\partial N_{o_2,j}}{\partial x_j} - s \cdot R_{fu} \tag{II.5}$$

In the above equations, ρ is the ensemble averaged density of the mixture, U_i is the i component of the density-weighted (Favre) mean velocity, $H_t = H + \frac{1}{2}U_i U_i$ is the density-weighted mean gas total enthalpy and H is the gas static enthalpy, Y_f and Y_{o_2} are the density-weighted mean mass fractions of fuel and oxidizer, and P is the mean pressure. $S_{m,l}$, $S_{u_i,l}$ and $S_{h,l}$ represent interaction terms (or source terms) of spray to be defined later. R_{fu} is the combustion rate in eddy breakup model, H_{com} is the combustion heat of fuel vapor and s is stoichiometric coefficient for oxidizer and fuel. S_h is the energy dissipation term and diffusion enthalpy is neglected in energy equation for multi-species flow, corresponding to unit Lewis number.

To account for turbulent flows, an eddy viscosity type model was employed. Thus

$$\tau_{ij} = -(\mu + \mu_t)(\frac{\partial U_i}{\partial x_j} + \frac{\partial U_j}{\partial x_i}) \tag{II.6}$$

$$Q_j = -(\frac{\mu}{Pr} + \frac{\mu_t}{Pr_t})\frac{\partial H}{\partial x_j} \tag{II.7}$$

$$N_{f,j} = -(\frac{\mu}{Sc} + \frac{\mu_t}{Sc_t})\frac{\partial Y_f}{\partial x_j} \tag{II.8}$$

$$N_{o_2,j} = -(\frac{\mu}{Sc} + \frac{\mu_t}{Sc_t})\frac{\partial Y_{o_2}}{\partial x_j} \tag{II.9}$$

$$S_{ui} = -\frac{2}{3}(\mu + \mu_t)\frac{\partial}{\partial x_i}(\frac{\partial U_j}{\partial x_j}) \tag{II.10}$$

$$\begin{aligned} S_h &= \frac{\partial}{\partial x_j}\{[(1 - \frac{1}{\mathrm{Pr}})\mu + (1 - \frac{1}{\mathrm{Pr}_t})\mu_t]\frac{\partial \frac{1}{2}U_iU_i}{\partial x_j}\} \\ &+ \frac{\partial}{\partial x_j}(\mu_t U_i \frac{\partial U_j}{\partial x_i}) - \frac{2}{3}\frac{\partial}{\partial x_i}(\mu_t U_i \frac{\partial U_j}{\partial x_j}) \end{aligned} \tag{II.11}$$

in which μ_t is described by the $k - \epsilon$ two-equation model. The last two terms in S_h are neglected conveniently with little error.

II.2.2 Equation of State

In this study, the gas phase is assumed to be the mixture of ideal gases. The equation of state for the mixture is

$$P = \rho RT \tag{II.12}$$

The gas constant R is related to the universal gas constant R_{con} ($8.3143\ J/gmol/K$), species molecular weight W_i and mass fraction Y_i :

$$R = \frac{R_{con}}{W_m} \tag{II.13}$$

And the average molecular weight W_m is defined as:

$$\frac{1}{W_m} = \sum_{i=1}^{m} \frac{Y_i}{W_i} \tag{II.14}$$

II.2.3 Turbulence Model

The two-equation effective diffusivity model is used to represent the turbulent characteristics. In the eddy diffusivity models, the turbulent fluxes, $\overline{u_i' u_j'}$ and $\overline{u_i' \phi'}$, are related to the mean flow gradients through the assumption of an isotropic eddy viscosity and a constant turbulent Prandtl or Schmidt number:

$$\rho\overline{u_i' u_j'} = -\mu_t\left(\frac{\partial U_i}{\partial x_j} + \frac{\partial U_j}{\partial x_i}\right) + \frac{2}{3}\delta_{ij}\left(\rho k + \mu_t \frac{\partial U_k}{\partial x_k}\right) \tag{II.15}$$

$$\rho\overline{u_i' \phi'} = -\frac{\mu_t}{\sigma_t}\frac{\partial \phi}{\partial x_i} \tag{II.16}$$

The eddy viscosity (μ_t) appearing in equations (II.15) and (II.16) is defined in terms of a characteristic turbulence length scale($k^{3/2}/\epsilon$) and a velocity scale ($k^{1/2}$), so that μ_t is given by

$$\mu_t = C_\mu \rho \frac{k^2}{\epsilon} \tag{II.17}$$

The turbulent kinetic energy, k, and its dissipation rate, ϵ, can be modeled from the turbulent transport equations:

$$\frac{\partial \rho k}{\partial t} + \frac{\partial}{\partial x_j}(\rho U_j k) = \frac{\partial}{\partial x_j}(\mu + \frac{\mu_t}{\sigma_k})\frac{\partial k}{\partial x_j} + \mu_t G - \rho\epsilon + S_{k,l} \qquad \text{(II.18)}$$

$$\frac{\partial \rho \epsilon}{\partial t} + \frac{\partial}{\partial x_j}(\rho U_j \epsilon) = \frac{\partial}{\partial x_j}(\mu + \frac{\mu_t}{\sigma_\epsilon})\frac{\partial \epsilon}{\partial x_j} + \frac{\epsilon}{k}(C_1 \mu_t G - C_2 \rho\epsilon) + S_{\epsilon,l} \qquad \text{(II.19)}$$

where the production term $\mu_t G$ takes the form

$$\begin{aligned} \mu_t G &= -\rho\overline{u_i' u_j'}\frac{\partial U_i}{\partial x_j} - \frac{\mu_t}{\rho^2}\frac{\partial \rho}{\partial x_j}\frac{\partial P}{\partial x_j} \\ &= \mu_t(\frac{\partial U_i}{\partial x_j} + \frac{\partial U_j}{\partial x_i})(\frac{\partial U_i}{\partial x_j}) - \frac{\mu_t}{\rho^2}\frac{\partial \rho}{\partial x_j}\frac{\partial P}{\partial x_j} - \frac{2}{3}(\rho k + \mu_t \frac{\partial U_i}{\partial x_i})\frac{\partial U_j}{\partial x_j} \end{aligned} \qquad \text{(II.20)}$$

The last term of equation (II.20) will be zero for incompressible flow due to continuity equation.

Table II.1: Turbulence model constants

$C_1 = 1.45$	$C_2 = 1.92$	$C_\mu = 0.09$	$\sigma_k = 1.0$	$\sigma_\epsilon = 1.3$	$\sigma_t = 0.9$

These are $k-\epsilon$ equations [70] with some added particle modulation terms. Here, term involving $\frac{\partial \rho}{\partial x_j}$ in equations (II.20) is inserted to account for variable-density effects [57]. These terms originally come from the pressure-velocity correlation in the Reynolds stress equation. For reacting flows, these terms should account partially for the expansion effect on the flow field due to heat release from combustion.

The added terms $S_{k,l}$ and $S_{\epsilon,l}$ accounting for the influence of particles on the turbulence structure will be discussed later.

II.2.4 Combustion Model

Combustion of liquid fuel droplets in a spray is governed by the diffusion of fuel vapor and oxidizer species. Both premixed and diffusion flame theories can be used for spray combustion processes. Sometimes premixed-flame theories can be applied to some cases, where very small droplets of a high- volatility fuel may be completely evaporated in the heat-up processes.

On the other hand, diffusion flame theories can be applied to many practical spray combustion processes. For these cases the fuel vapor evaporated from the droplet surface has to mix with the ambient oxidizer before chemical reaction can occur. In this study, it is assumed that liquid fuel droplets act as distributed sources of fuel which evaporate to form a cloud of vapor and the combustion process in spray flames can be treated as turbulent gaseous diffusion flames. Experimental evidence for this assumption can be found in [117]. An idealized approach for physically-controlled diffusion flames is to invoke a fast-chemistry assumption which the chemistry is sufficiently fast and intermediate species do not play a significant role. In the turbulent diffusion flame model, the influence of turbulence on combustion is taken into account by relating the fluctuations of mass fractions. This implies that fuel and oxidizer can coexist in the same place but at a different time.

A modified eddy breakup model [76] is incorporated in the present study. Using this model, the reaction rate is determined as follows: in an irreversible single-step chemical reaction, the mixing-controlled reaction rate [76] is given by

$$R_{mix} = A_{mix}\rho\frac{\epsilon}{k}min(Y_f, \frac{Y_{O2}}{s}) \qquad \text{(II.21)}$$

where $A_{mix} = 4$ is a model constant; s is the stoichiometric oxidant/fuel ratio; Y_f

and Y_{O2} are the mass fractions of the fuel and the oxidizer. To account for the ignition delay time, the chemical kinetics need to be considered. The chemically controlled reaction rate, R_{che}, is given by the usual Arrhenius formula [119].

$$R_{che} = A(\frac{\rho Y_f}{W_f})^a(\frac{\rho Y_{O2}}{W_{O2}})^b exp(-\frac{E}{RT}) \tag{II.22}$$

The reaction rate, R_{fu} is determined from either of the mixing rate of the reactants or the chemical reaction rate, whichever slower.

$$R_{fu} = min(R_{mix}, R_{che}) \tag{II.23}$$

The irreversible single-step reaction of the hydrocarbon-air mixtures is expressed as follows:

$$C_xH_y + (x + \frac{y}{4})(O_2 + nN_2) \rightarrow xCO_2 + \frac{y}{2}H_2O + (x + \frac{y}{4})nN_2 \tag{II.24}$$

Here, n is 3.76 for air. In the given reaction process, five species (fuel,O_2, N_2, CO_2, and H_2O) are participating the mixture composition. Once the mass fraction of fuel and oxidizer have been determined from the solutions of the transport equations, the mass fraction of the remaining species can be obtained from the following stoichiometric relations.

$$Y_{H_2O} = K_2(1 - K_1Y_{O2} - Y_{fu}) \tag{II.25}$$

$$Y_{CO_2} = K_3Y_{H_2O} \tag{II.26}$$

$$Y_{N_2} = 1 - (Y_{H_2O} + Y_{CO_2} + Y_{O_2} + Y_{fu}) \tag{II.27}$$

where

$$K_1 = 1 + n\frac{W_{N_2}}{W_{O_2}} \tag{II.28}$$

$$K_2 = \frac{\frac{y}{2}W_{H_2O}}{\frac{y}{2}W_{H_2O} + (x + \frac{y}{4})nW_{n_2} + xW_{CO_2}} \tag{II.29}$$

$$K_3 = \frac{xW_{CO_2}}{\frac{y}{2}W_{H_2O}} \tag{II.30}$$

II.3 Basic Lagrangian Equations

In this study, the spray is described by a discrete particle method formulated on a Lagrangian frame. This is essentially a statistical approach and requires tracking a sufficiently large number of computational particles. Each computational particle represents a number of droplets having equal location, velocity, size, and temperature. The particle characteristics are governed by equation of motion, equation of evaporation and equation of heat transfer. These ordinary differential equations will be integrated along the particle trajectories.

II.3.1 Droplet Motion Equation

The equation of motion of a particle within a fluid continuum was originally derived by Basset, Boussinesq and Oseen for a fluid at rest, hence the B-B-O equation, and extended by Tchen [114] to the case of a fluid moving with variable velocity.

$$\begin{aligned}\frac{\pi}{6}{d_p}^3\rho_p\frac{dv_i}{dt} &= \frac{\pi}{8}{d_p}^2\rho C_D|v_i-u_i|(v_i-u_i) - \frac{\pi}{6}{d_p}^3\frac{\partial p}{\partial x_i} + \frac{\pi}{12}{d_p}^3\rho(\frac{du_i}{dt}-\frac{dv_i}{dt}) \\ &\quad + \frac{3}{2}{d_p}^2\sqrt{\pi\rho\mu}\int_{t_0}^{t}dt'\frac{\frac{du_i}{dt'}-\frac{dv_i}{dt'}}{\sqrt{t-t'}} + \frac{\pi}{6}{d_p}^3\rho_p F_{bi}\end{aligned} \tag{II.31}$$

where t_0 is the particle starting time; the sub index p refers to the particle; v_i and u_i are the velocities of the particle and the surrounding fluid respectively. The fluid velocity u_i should be defined at a distance far enough to the discrete particle not to be disturbed by the relative motion of the particle.

The term on the left hand side of equation(II.31) is the inertial force of the particle. The first term on right hand side of equation(II.31) is the drag force on the particle. The second term is the force on the particle due to the static pressure gradient in the flow field. The third term is the force due to the inertia of fluid displaced by the particle motion, or virtual mass term. The fourth term is the so-called "Basset" term, which comes from the effect of the deviation of the flow pattern from steady state. The last term F_{bi} represents the body force terms such as the gravity force and the centrifugal force.

For the particular case of the motion of solid or liquid spheres in gas phase, where the particle density is much higher than the gas density, effects of static pressure gradient, virtual mass term and Basset force can be neglected. The drag term is treated empirically, assuming quasi-steady flow for single spherical particle.

The approximate form of the B-B-O equation of motion is

$$\frac{dv_i}{dt} = \frac{U_i + u_i' - v_i}{\tau} + F_{bi} \tag{II.32}$$

In equation (II.32), F_{bi} represents the body force terms acting on the particle per unit mass in i-direction, and u_i' is included to represent gas fluctuating velocity effect.

The particle relaxation time τ can be expressed as:

$$\tau^{-1} = \frac{3}{8}\frac{\rho}{r_p} C_D |U_i + u_i' - v_i| \tag{II.33}$$

C_D is the drag coefficient given by

$$C_D = \begin{cases} \frac{24}{Re_p}(1 + \frac{1}{6}Re_p{}^{\frac{2}{3}}) & \text{if} \quad Re_p \leq 1000 \\ 0.424 & \text{if} \quad Re_p > 1000 \end{cases} \tag{II.34}$$

In which the particle Reynolds number Re_p is defined as

$$Re_p = \frac{|U_i + u_i' - v_i|\rho d_p}{\mu} \tag{II.35}$$

where μ is the gas phase laminar viscosity.

The particle position for each group can be obtained by integrating:

$$\frac{dx_i}{dt} = v_i \tag{II.36}$$

II.3.2 Droplet Evaporation Model

Droplet size and temperature are governed by the mass and energy conservation law for each droplet. They are:

$$\frac{dr_p}{dt} = -\frac{\dot{m}_{ev}}{4\pi {r_d}^2 \rho_d} \tag{II.37}$$

and

$$\frac{dT_d}{dt} = \frac{\dot{Q}_L}{m_p C_{p,d}} \tag{II.38}$$

In equation (II.37), the droplet evaporation rate is given by the Frossling correlation [37] :

$$\dot{m}_{ev} = 2\pi d_p(\rho D)(1 + 0.3{Re_p}^{\frac{1}{2}}{Sc_p}^{\frac{1}{3}})ln(1 + B_m) \tag{II.39}$$

In equation (2.16), the droplet temperature T_d, which is assumed to be constant within the droplet, is found by using the heat energy Q_L :

$$\dot{Q}_L = 4\pi {r_p}^2 \dot{Q}_c - \dot{m}_{ev} L \tag{II.40}$$

where L is the latent heat of vaporization, and $\dot{Q}_c$ is the heat conduction rate to the droplet surface per unit area given by the Ranz-Marshall correlation [33]

$$\dot{Q}_c = \frac{2K(T - T_d)}{d_p}(1 + 0.3{Re_p}^{\frac{1}{2}}{Pr_p}^{\frac{1}{3}})\frac{ln(1 + B_m)}{B_m} \tag{II.41}$$

The Schmidt number Sc_p, Prandtl number Pr_p, and mass transfer number B_m are defined respectively as

$$Sc_p = \frac{\mu}{\rho D} \tag{II.42}$$

$$Pr_p = \frac{\mu C_p}{K} \tag{II.43}$$

and

$$B_m = \frac{Y_s - Y_\infty}{1 - Y_s}; \quad Y_\infty = \frac{\rho_f}{\rho} \tag{II.44}$$

The values of thermodynamical properties of gas such as K, C_p, D etc. are highly dependent on the temperature and fuel vapor mass fraction at which they are evaluated. A "one-third rule" [32] that utilizes a reference temperature equal to the droplet surface temperature plus one-third of the difference between the surrounding gas and droplet surface temperature is used. The same procedure is applied to the reference value for the fuel vapor mass fraction, in which Y_s is obtained from

$$Y_s = [1 + (\frac{P}{P_v} - 1)\frac{W_m}{W_f}]^{-1} \tag{II.45}$$

Here Y_s and P_v are the mass fraction and the fuel vapor pressure at the droplet surface, and W_f and W_m are the molecular weights of fuel and mixture, respectively. For a given T_d, P_v is estimated from the $JANAF$ data bank [116].

The above Frossling correlation is valid only for dilute spray evaporation process. Radiative heat transfer and near critical and supercritical behavior are not included in this model. Also, more sophisticated evaporation models, such as Bellan's group evaporation model [10, 11, 13, 12, 14] or Chiu's group combustion model [26, 53, 52, 51, 25] should be incorporated in future studies to consider the dense spray effect.

II.3.3 Droplet Size Distribution Model

In a spray combustion chamber, sprays are generated by atomizers. These practical sprays generally consist of a series of non-uniform size droplets, or a spectrum of droplet sizes. Such a distribution of drop size varies under different liquid injections and operating conditions. Many experimental studies [72] were carried out to provide

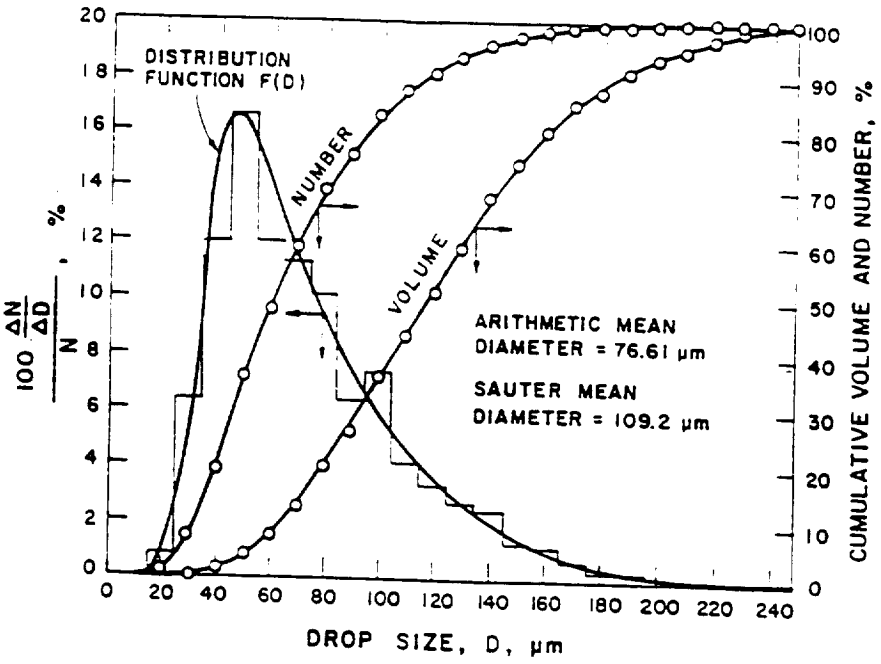

Figure II.1: Drop size distribution curves for a water spray in an air stream

correlations for engineering designers and researches. A lot of mathematical models can also be used without the detail distribution information.

Overall drop size characteristics are represented by their distribution curves which related to the cumulative percentage of droplet number (N), surface area (A), or volume (Q) as a function of droplet size (D), as shown in Figure II.1 [79].

In the analysis of many spray dynamics, evaporating or combustion processes, only an average droplet size is desirable instead of the complete droplet size distribution. This droplet size is usually chosen as a mean or median diameter. General definition of a mean droplet diameter D_{ab} raised to a power (a-b) is

$$(D_{ab})^{a-b} = \frac{\int_0^\infty D^a f(D) dD}{\int_0^\infty D^b f(D) dD} \tag{II.46}$$

where

$$f(D) = \frac{dN}{dD} \tag{II.47}$$

is a number distribution function, dN and N are the number of droplets in the size range from D to $D+dD$ and the total droplet number respectively. Its corresponding cumulative function F(D) is defined as

$$F(D) = \int_0^D f(D)dD \tag{II.48}$$

The commonly used mean diameter for approximate analysis of spray evaporation and combustion as an equivalent monodisperse spray is the so-call "Sauter Mean Diameter" (SMD or D_{32}), which is defined as the ratio of entire spray's volume to its surface area.

The dilute spray model assumes that the fuel is injected into the combustion chamber as a fully atomized spray which consists of spherical droplets. The droplet-size distribution within the spray is represented by a finite number of size ranges. Several empirical distribution functions have been proposed to characterize the distribution of drop sizes in a spray [72]. None of these is universally better than others. Model constants are adjusted to match the given set of data.

χ -Squared Distribution

The normalized number distribution function for χ -squared distribution is given:

$$f(R) = \frac{R^3}{6\overline{R}^4} exp(-\frac{R}{\overline{R}}) \tag{II.49}$$

where $\overline{R}$ is the number-averaged drop radius, which for this distribution is related to Sauter Mean Radius (SMR) by

$$\overline{R} = \frac{1}{3} SMR \tag{II.50}$$

The corresponding cumulative distribution function is

$$F(D) = 1 - exp(-\frac{R}{\overline{R}})[1 + \frac{R}{\overline{R}} + \frac{1}{2}(\frac{R}{\overline{R}})^2 + \frac{1}{6}(\frac{R}{\overline{R}})^3] \tag{II.51}$$

This correlation needs only one constant (SMD or SMR) and is used in KIVA-II code [4].

Nukiyama-Tanasawa Distribution

$$\frac{dN}{N} = A(\frac{D}{SMD})^{\alpha} exp[(-B(\frac{D}{SMD})^{\beta}]\frac{dD}{SMD} \tag{II.52}$$

where α, β, A, and B are experimentally determined constants. This expression is relative simple and adequately describes the actual distribution.

Rosin-Rammler Distribution

$$1 - Q = exp[-(\frac{D}{X})^{q}] \tag{II.53}$$

or differential expression:

$$\frac{dQ}{dD} = \frac{qD^{q-1}}{X^{q}} exp[-(\frac{D}{X})^{q}] \tag{II.54}$$

$$\frac{X}{SMD} = \Gamma(1 - \frac{1}{q}) \tag{II.55}$$

where Q is the fraction of the total volume contained in drops of diameter less than D, and X and q are correlation constants. The relationship between X, SMD and q is established through the Gamma function Γ [72]. At present, this is the most widely used expression for spray drop size distribution.

II.3.4 Particle Turbulent Dispersion

Numerical modeling of particle turbulent dispersion based on the Lagrangian particle tracking method was first proposed by Dukowicz [31] using a stochastic method, where particle turbulence was modeled by arbitrarily assuming gas turbulent kinetic energy and particle-eddy interaction time. It was further developed by Gosman and

Ioannides [39] and Shuen et al. [109] to include $k-\epsilon$ turbulence model and estimate gas turbulent kinetic energy and eddy life-time. Main differences in the implementations are the methods used to specify turbulence eddy properties and the methods for choosing the interaction time of a particle with a particular eddy. A two equation turbulence model, $k-\epsilon$, is used to characterize flow field turbulence quantities, such as turbulence fluctuation, eddy life time and length scale. Turbulence effects on particles are modeled by adding to the mean gas velocity U_i a fluctuating velocity u_i' when tracking particles through a continuous succession of turbulent eddies. Theoretically, this simulation requires knowledge of the full time history of the turbulent flow by direct solution of unaveraged Navier-Stokes equation. Since this is impossible at present for most of flows of practical interest, the turbulence is simulated by means of a stochastic process or the Monte Carlo method. The instantaneous velocities for the gas phase are given by $U_i + u_i'$. Assuming an isotropic turbulence, each component of u_i' is randomly chosen from a Gaussian distribution with standard deviation $\sqrt{\frac{2}{3}k}$, where k is the specific turbulent kinetic energy of the gas phase in the computational cell in which particle is located. This assumption represents a significant simplification for actual complex turbulent flows where anisotropic turbulence will be expected, thus requiring a non-Gaussian distribution of turbulence intensity in three dimensional space domain.

Adding fluctuating velocity u' to droplet motion equation (II.32), we have

$$\frac{dv_i}{dt} = \frac{U_i + u_i{}' - v_i}{\tau} + Fb_i \qquad \text{(II.56)}$$

This equation represents particle-eddy interaction along its trajectory. The sum $U_i + u_i{}'$ is the gas phase velocity that transfers momentum to the particle which "sees" the eddy. It is this fluctuating velocity $u_i{}'$ produces particle turbulent dispersion,

which keeps a piecewise constant function of time, changing discontinuously after passage of one particle-eddy interaction. The interaction time depends on the eddy life time t_e and the particle transit time t_{tr} within each eddy.

To derive the eddy life time t_e, we can choose a particle small enough that will fluctuate following the gas fluctuating velocity u_i'. We can expect in this particular case,

$$v_i' = u_i' \tag{II.57}$$

where v_i' is the particle fluctuating velocity. Recall the assumption of the gas fluctuating velocity u_i', also v_i' this time, obeying a Gaussian distribution with a standard deviation $\sigma_{u'}$

$$\sigma_{u'} = \sqrt{\frac{2}{3}k} \tag{II.58}$$

After one particle-eddy interaction the deviation of the dispersed particle position will be

$$\sigma_{x'} = \sigma_{u'} t_e \tag{II.59}$$

A distribution that follows a diffusion law has the following relation,

$$\sigma_{x'}^2 = 2Dt_e \tag{II.60}$$

In the limit of small particles, we expect that the particles will fully follow the fluid motion and their diffusivity D should be same as the eddy kinetic viscosity ν_t, which means gas-phase momentum diffusion,

$$D = \nu_t = C_\mu \frac{k^2}{\epsilon}. \tag{II.61}$$

The last relation coming from the $k - \epsilon$ turbulence model used here. After some algebraic arrangements, we can obtain the eddy life time

$$t_e = 3C_\mu \frac{k}{\epsilon} \tag{II.62}$$

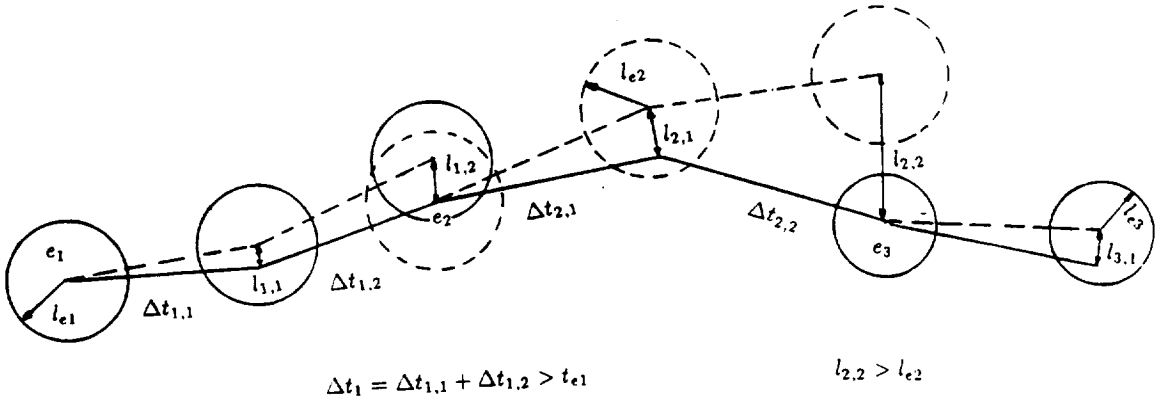

Figure II.2: Shetch of the particle-eddy interaction

Based on $k-\epsilon$ turbulence model, an eddy dissipation length scale is proportional to $k^{\frac{3}{2}}/\epsilon$ and it has been used as the following

$$l_e = 1.65 C_\mu^{\frac{3}{4}} \frac{k^{\frac{3}{2}}}{\epsilon} \tag{II.63}$$

where the proportional constant is chosen by fitting the experimental data of Snyder and Lumley [113].

In this study, the particle-eddy interaction time t_{int} is controlled by the eddy life time t_e and length scale l_e. If a particle interacts with the eddy over a time t_e or the displacement from the moving eddy center is larger than l_e, the particle will interact with a new eddy and a new gas fluctuating velocity u_i' will be generated as mentioned before. This process is shown in Figure II.2.

Here, we do not estimate t_{int} as suggested by Shuen et al. [31] in which t_{tr} was calculated from a linearized equation (II.56) by keeping τ a constant and without

the body force effect. Instead, we follow a similar stochastic procedure suggested by Nichols [86] and trace particle trajectories as time progresses. The turbulent fluctuating velocities u_i' at three directions are generated with a Gaussian distribution when an eddy is created and remain constant in the particle-eddy interaction period. At each time step, the summations of the interaction time and the distance between eddy center and particle are stored at two arraies and compared with the eddy life time t_e and length scale l_e, which are calculated from equations (II.62, II.63) based on the local gas-phase turbulence properties. If either of the eddy life time and length scale is exceeded, a new eddy will be generated at the particle's location and the particle begins to interact with this new eddy.

Figure II.2 graphically shows an example of the particle-eddy interaction process. The particle first interacts with eddy e_1 and begins moving with the eddy center. The eddy time scale and length scale are t_{e1} and l_{e1} respectively. With time progressing, the particle remains in this eddy until the interaction time Δt_1 exceeds t_{e1} regardless $l_{1,2} < l_{e1}$ at that time. The particle begins interaction with a new eddy e_2. After two interactions, the distance $l_{2,2}$ between the particle and eddy e_2 exceeds the length scale l_{e2} of this eddy and a new eddy e_3 is generated again.

This method has the flexibility of taking into account both the gravity effect (crossing trajectory effect) and the non-Stokesian drag law and gives more satisfactory results for medium and heavy particle dispersions comparing with the experimental data of Snyder and Lumley [113].

The above procedure for solving equation(II.56) requires the calculation time step Δt being smaller than the particle-eddy interaction time t_{int}, otherwise the particle will "see" more than one turbulent fluctuating velocity u_i' on the current cycle.

Possibly, we can use a smaller time step or subcycle time step for the particle phase. These methods are not computationally efficient, however, when t_{int} is much smaller than Δt. O'Rourke [88] derived the particle velocity and position changes based on the assumptions of the Gaussian distribution of turbulent fluctuating velocity u_i' and constant particle relaxation time τ, turbulent kinetic energy k and particle-eddy interaction time t_{int} for the given particle on the current time step. O'Rourke's approach [88] is inaccurate for the effects of the fluctuating velocity u_i' on heat and mass exchange and droplet breakup and collision processes.

The assumption of a linear drag law simplifies the analysis, therefore each component of the velocity and position changes can be treated independently. It has been shown[88] that for each component the distributions are Gaussian when the gas phase turbulent fluctuating velocity is Gaussian. The particle velocity distribution has variance

$$\sigma_{v'}^2 = \frac{1 - exp(-t_{int}/\tau)}{1 + exp(-t_{int}/\tau)}[1 - exp(-2\Delta t/\tau)]\sigma_{u'}^2 \tag{II.64}$$

and its position distribution has variance

$$\sigma_{x'}^2 = \{t_{int}\Delta t - 2t_{int}\tau[1 - exp(-t_{int}/\tau)] + \frac{\sigma_{v'}^2}{\sigma_{u'}^2}\tau^2\}\sigma_{u'}^2 \tag{II.65}$$

where $\sigma_{u'}^2 = \frac{2}{3}k$.

When $\delta t > t_{int}$ the particle velocity and position are updated using

$$\frac{v_i^* - v_i^n}{\Delta t} = \frac{(U_i - v_i^*)}{\tau} + Fb_i + \frac{\delta v_i'}{\Delta t} \tag{II.66}$$

and

$$\frac{x_i^* - x_i^n}{\Delta t} = v_i^n + \frac{\delta x'}{\Delta t} \tag{II.67}$$

where $\delta x'$ and $\delta v'$ are the particle turbulent position and velocity changes. $\delta x'$ is

calculated from

$$\delta x' = t_{per}\delta v' + \delta x'_b \tag{II.68}$$

Each component of $\delta v'$ and $\delta x'_b$ is chosen from a Gaussian distribution with variance $\sigma^2_{v'}$ and $\sigma^2_{x'} - t^2_{per}\sigma^2_{v'}$ respectively. t_{per} is a so-called turbulence persistence time and enters due to the independent distribution of turbulent particle velocity and position changes.

$$t_{per} = \frac{t_{int}[1 - exp(-\Delta t/\tau)] - \frac{\sigma^2_{v'}}{\sigma^2_{u'}}\tau}{\frac{\sigma^2_{v'}}{\sigma^2_{u'}}} \tag{II.69}$$

II.3.5 PDF of Particle Turbulent Dispersion

Assuming isotropic turbulence properties and a Gaussian distribution for gas turbulent kinetic energy, particle fluctuating velocity and position also obey this Gaussian distribution as seen from the above discussion. The particle PDF (Probability Density Function) in two dimension form is

$$p(x,y) = \frac{1}{2\pi\sigma^2}exp(-\frac{x^2+y^2}{2\sigma^2}) \tag{II.70}$$

or in cylindrical coordinate

$$p(r,\theta) = \frac{1}{2\pi\sigma^2}exp(-\frac{r^2}{2\sigma^2}) \tag{II.71}$$

where particles disperse from a point source (0,0).

When calculations are performed in a cylindrical coordinate with constant properties in tangential direction, any particle dispersion from a point (x_0, y_0) in a transverse plane represent one from a circle with radius r_0, where $r_0 = \sqrt{x_0^2 + y_0^2}$. This PDF can be obtained by integration along the circle (see Appendix A),

$$p(r,\theta) = \frac{exp[-(r^2+r_0^2)/(2\sigma^2)]}{2\pi\sigma^2}\sum_{n=0}^{\infty}[\frac{(\frac{rr_0}{2\sigma^2})^n}{n!}]^2 \tag{II.72}$$

This PDF $p(r,\theta)$ represents particle probability in an area $rd\theta\ dr$ and is independent of θ. If we integrate the above equation over θ domain, we will obtain particle probability in rdr,

$$p(r) = \frac{exp[-(r^2+r_0^2)/(2\sigma^2)]}{\sigma^2} \sum_{n=0}^{\infty} [\frac{(\frac{rr_0}{2\sigma^2})^n}{n!}]^2 \tag{II.73}$$

In stochastic modeling of particle dispersion in two dimensional flows, usually we track particles in both x- and y-directions.

$$\frac{dv_x}{dt} = \frac{U_x + u_x{}' - v_x}{\tau} + F_{bx} \tag{II.74}$$

$$\frac{dv_y}{dt} = \frac{U_y + u_y{}' - v_y}{\tau} + F_{by} \tag{II.75}$$

$$v_z = 0 \tag{II.76}$$

The equations (II.74, II.75, II.76) are true for two dimensional plane flows and incorrect for axisymmetric flows due to the neglect of turbulent fluctuation in z-direction. To account for this three dimensional fluctuating phenomena, we solve particle momentum equation in z-direction instead of keeping it as zero for axisymmetric flows,

$$\frac{dv_z}{dt} = \frac{u_z' - v_z}{\tau} \tag{II.77}$$

and particle trajectory

$$\frac{dz}{dt} = v_z \tag{II.78}$$

Note that mean gas velocity and body force have been set to zero. Particle position in radial direction is calculated as

$$r = \sqrt{y^2 + z^2} \tag{II.79}$$

To test the present stochastic procedure, 10,000 particles are calculated at three different locations for each different circle, as shown in Figure II.3, where particles

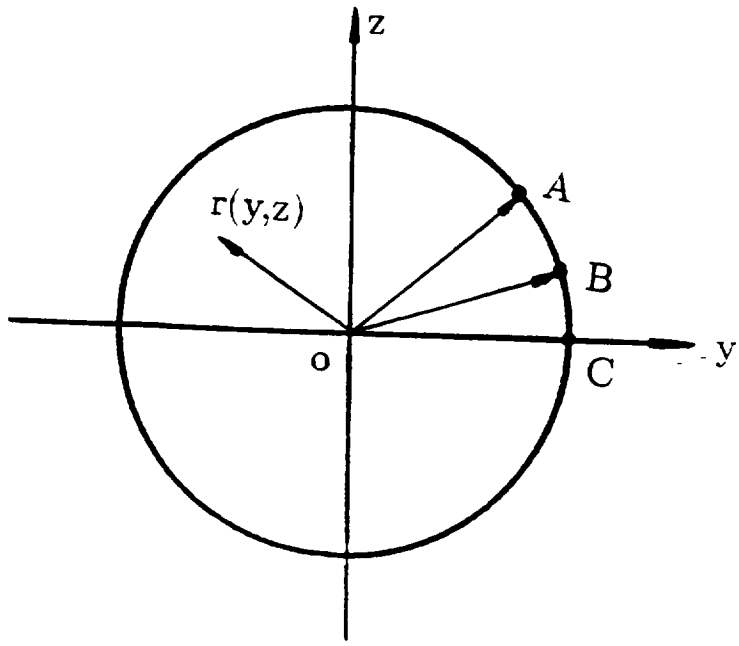

Figure II.3: Particle dispersion from a circle

begin to disperse. Particle distribution variance is assumed to be 1, which can be considered as particle position being normalized by the variance. Four circle radii (0.5, 1, 2 and 3) have been used to cover a large variation of radius-variance ratio.

We can see from Figures II.4 and II.5 that this stochastic procedure results an equivalent particle distribution as described by equation (II.73) for an isotropic particle turbulent dispersion, and the distribution function is independent of the starting locations. Figures II.4 and II.5 also show the simplified PDF of Litchford and Jeng [75], that will be discussed in the next section, is in reasonable agreement with the present exact solution and good agreement as expected is reached for small and large radius-variance ratios.

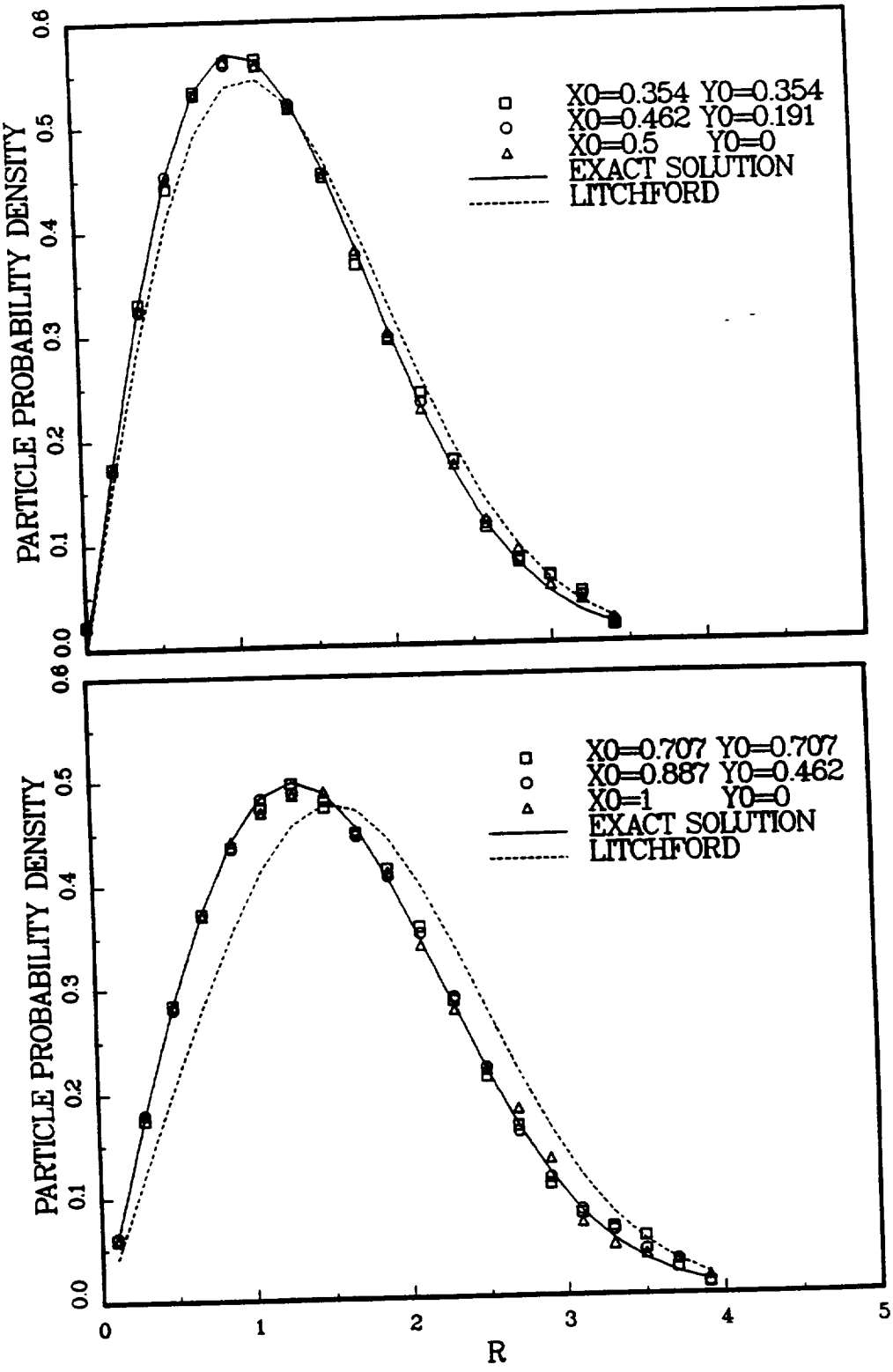

Figure II.4: PDF of particle dispersion from a circle (a)

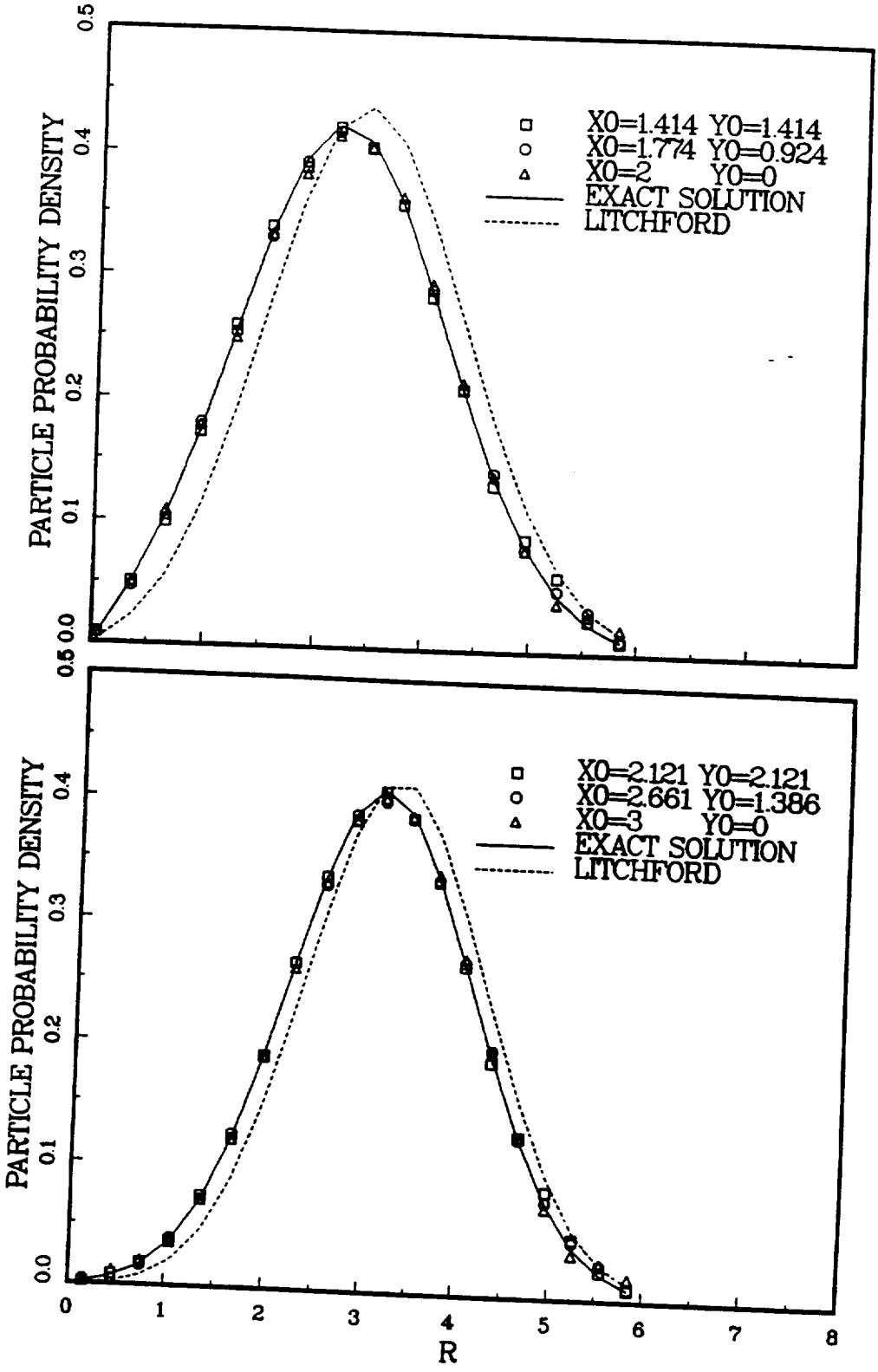

Figure II.5: PDF of particle dispersion from a circle (b)

II.3.6 Parcel PDF Model

In this study, the spray is described by a discrete particle method formulated on a Lagrangian frame. The turbulence effects on droplet dispersion are simulated by a Monte Carlo method in the sense that a fluctuating velocity u'_k, where each component of u'_k is randomly chosen from a Gaussian distribution with standard deviation $\sqrt{\frac{2}{3}k}$, is added to the mean gas velocity. Thus the turbulence is assumed to be isotropic. This type of simulation for the turbulent dispersion of droplets has been extensively used previously [39, 36, 110] for statistically stationary turbulent dispersed flows and is called stochastic separated flow (SSF) model. In previous SSF model, computational particle position is characterized by a delta function in space. This computational particle represents a group of real physical particles which are assumed to stay at the center of the cluster. It does not consider the particle turbulent dispersion or probability function distribution within the cluster. When an insufficient number of particles are tracked and the two phase interaction source terms are evaluated, shot noise or over predicted flow field fluctuations will be generated in computational space and time domain. The shot noise will also increase in fine grid calculation. One of the important effects may occur in the spray combustion instability analysis when feedback responses to local transient flow field perturbation are over disturbed. Therefore, statistically meaningful calculations will require a large number of particle trajectories and, consequently, very long computational time or reduced spatial resolution of the analysis.

To account for droplet turbulent dispersion, we follow the concept of Litchford and Jeng [75], and Zhou and Yao [124] of combining a normal (Gaussian) probability distribution for each computational particle. The instantaneous location of each

computational particle is calculated by a stochastic Lagrangian tracking scheme.

The governing equation for each computational particle is

$$\frac{dv_k}{dt} = \frac{u_k - v_k}{\tau_k} + F_{bk} \tag{II.80}$$

$$\frac{dx_k}{dt} = v_k \tag{II.81}$$

with

$$\tau_k^{-1} = \frac{3}{8}\frac{\rho}{\rho_p}\frac{C_D}{d_p}|u_k - v_k| \tag{II.82}$$

When u and v are taken as the instantaneous properties, the location calculated by the above equations only represents the mean of each particle's corresponding probability function. The variance of each parcel PDF has to be calculated and the combined PDFs then represent the statistical distribution of particles with turbulent dispersion effects. To estimate the variance of the parcel PDF due to the turbulent particle dispersion, the turbulence-induced displacement and velocity can be splitted from equations (II.81, II.82):

$$\frac{dv'_k}{dt} = \frac{u'_k - v'_k}{\tau_k} \tag{II.83}$$

$$\frac{dx'_k}{dt} = v'_k \tag{II.84}$$

With the isotropic turbulence assumption, each component of u'_k is randomly chosen from a Gaussian distribution with standard deviation $u'_{krms} = \sqrt{\frac{2}{3}k}$. We first choose $\triangle t_{ki}$ as the time step of the particle i^{th} interaction within the k^{th} eddy, which is smaller than its eddy life time t_{ek}, and integrate equations (II.83, II.84) in that sequence to update particle fluctuating locations and velocities.

$$x'_{ki} = u'_{krms}\triangle t_{ki} + (v'_{k(i-1)} - u'_{krms})\tau_{k(i-1)}(1 - exp(-\frac{\triangle t_{ki}}{\tau_{k(i-1)}})) \tag{II.85}$$

$$v'_{ki} = u'_{krms} + (v'_{k(i-1)} - u'_{krms})exp(-\frac{\triangle t_{ki}}{\tau_{k(i-1)}}) \tag{II.86}$$

We then sum up the m steps for which the particle fully interact with the k^{th} eddy,

$$\sum_{i=1}^{m} \triangle t_{ki} = \triangle t_k = t_{ek} \tag{II.87}$$

The change of variance of a computational particle PDF within the k^{th} eddy is represented by a characteristic mean squared dispersion in the form:

$$\sigma_k{}^2 = \sigma_{k-1}{}^2 + (\sum_{i=1}^{m} x'_{ki})^2 \tag{II.88}$$

In equation(II.88), σ_{k-1} is the existing variance of the particle PDF at the beginning of the interaction within the k^{th} eddy. Since the time step within each turbulent eddy is fixed, the number of interaction within the eddy, m, varies across the calculation domain, the choice of time step $\triangle t_{ki}$ and the related issues are discussed in detail in [74]. Figure II.6 describes this eddy interaction with the particles.

The present procedure is easy to program and requires less computer memory. For each computational particle, we just need to store x'_{ki}, u'_{krms},v'_{ki}, and $\sigma_k{}^2$. This procedure when implemented in the current time-marching numerical method is somewhat different from the method of Litchford and Jeng [75] in which the calculation of the current variance of each particle PDF is summed over the entire history of the effective time constants. In their recent study, truncation of unnecessary time history terms and the associated errors were discussed and additional computational efficiency was obtained [74].

When convoluting PDF for a group of computational particles with their trajectories calculated by SSF model, the variances of equation (II.88) must be normalized according to the total number of particles. The normalized particle variance can be

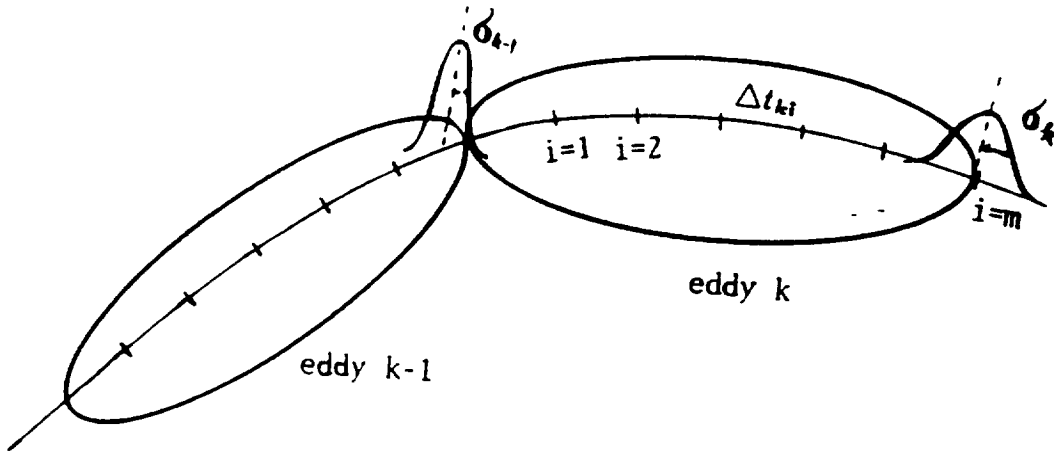

Figure II.6: Eddy interaction with the particles

written as

$$\hat{\sigma}_{yk} = K\frac{\sigma_{yk}}{\sqrt{N_t}} \tag{II.89}$$

Here, $\frac{\sigma_{yk}}{\sqrt{N_t}}$ represents the statistical uncertainty in the mean particle position, K is the correction factor to account for undersampling, and N_t is the total number of computational particles. When symmetry and reflective boundary condition exist in the calculation domain, a cumulative PDF distribution at any point in coordinate y, which is the distance from the particle to the axis or the reflective boundary, can be defined for plane and axial symmetric coordinates respectively.

Plane Symmetric

$$P(y) = \int_{-y}^{y} \frac{1}{\sqrt{2\pi}\hat{\sigma}_{yk}} exp[-\frac{(y-y_p)^2}{2\hat{\sigma}_{yk}^2}]dy \tag{II.90}$$

Here, y_p is the instantaneous location of computational particles. After integration,

the symmetric cumulative distribution function takes the form,

$$P(y) = 0.5[erf(\frac{y - y_p}{\sqrt{2}\hat{\sigma}_{yk}}) + erf(\frac{y + y_p}{\sqrt{2}\hat{\sigma}_{yk}})] \tag{II.91}$$

where the error function is defined as

$$erf(x) = \frac{2}{\sqrt{\pi}} \int_o^x exp(-\zeta^2) d\zeta \tag{II.92}$$

The corresponding PDF is

$$p(y) = \frac{0.5}{\sqrt{2\pi}\hat{\sigma}_{yk}} \{exp[-\frac{(y - y_p)^2}{2\hat{\sigma}_{yk}^2}] + exp[-\frac{(y + y_p)^2}{2\hat{\sigma}_{yk}^2}]\} \tag{II.93}$$

Axial Symmetric

Particle PDF distribution at this case should be equation (II.73), but it is too complex to integrate. A simplified axisymmetric cumulative distribution function introduced by Litchford and Jeng [75] takes the form

$$P(r) = \frac{F(r)}{F(r \to \infty)} \tag{II.94}$$

where

$$\begin{aligned} F(r) &= \sqrt{2\pi}\hat{\sigma}_r \{2exp(-\frac{r_p^2}{2\hat{\sigma}_r^2}) - exp[-\frac{(r - r_p)^2}{2\hat{\sigma}_r^2}] - exp[-\frac{(r + r_p)^2}{2\hat{\sigma}_r^2}]\} \\ &+ \pi r_p [erf(\frac{r - r_p}{\sqrt{2}\hat{\sigma}_r}) - erf(\frac{r + r_p}{\sqrt{2}\hat{\sigma}_r}) + 2erf(\frac{r_p}{\sqrt{2}\hat{\sigma}_r})] \end{aligned} \tag{II.95}$$

and

$$F(r \to \infty) = 2\sqrt{2\pi}\hat{\sigma}_r exp(-\frac{r_p^2}{2\hat{\sigma}_r^2}) + 2\pi r_p erf(\frac{r_p}{\sqrt{2}\hat{\sigma}_r}) \tag{II.96}$$

In accordance with the approach of Litchford and Jeng [75], when the mean positions of computational particles are calculated by the deterministic tracking (u_k in equations (II.80 - II.82) is the mean gas velocity), this approach is described as the deterministic dispersion width transport(DDWT) model. For tracking with

stochastic sampling of gas-phase turbulent velocity fluctuations (u_k in equations (II.80 - II.82) is the instantaneous gas velocity), the approach is described as a stochastic dispersion width transport (SDWT) model.

II.3.7 Turbulence Modulation Model

Turbulence modulation effect appears with the presence of the dispersed particle phase. This effect comes into the governing equations (II.18 and II.19) of turbulent kinetic energy and its dissipation rate through the source terms $S_{k,l}$ and $S_{\epsilon,l}$. Shuen [107] derived the expressions based on the gas-phase momentum equation (II.2) with the interphase source term $S_{ui,l}$. These terms can be written as

$$S_{k,l} = \overline{u_i S_{ui,l}} - U_i \overline{S_{ui,l}} \tag{II.97}$$

$$S_{\epsilon,l} = 2\mu \overline{\frac{\partial u_i'}{\partial x_j} \frac{\partial S'_{ui,l}}{\partial x_j}} \tag{II.98}$$

Within the framework of discrete particle stochastic approach using Lagrangian tracking, u'_i follows the Gaussian distribution and the instantaneous properties of two-phase interaction force $S_{ui,l}$ takes the form

$$S_{ui,l} = \frac{1}{dV} \sum_{p=1}^{NP} [N_p \dot{m}_{ev,p} (v_i)_p - m_p N_p (\frac{U_i + u_i' - v_i}{\tau})_p] \tag{II.99}$$

where v_i is the instantaneous particle velocity, τ is the particle relaxation time, m_p is the droplet mass and $\dot{m}_{ev}$ is the droplet evaporation rate as defined before. Equation (II.97) can also be written as

$$S_{k,l} = \overline{u_i' S_{ui,l}} \tag{II.100}$$

Thus $\overline{u_i' S_{ui,l}}$ can be calculated directly without modeling in equation (II.18). This is the approach used in [110, 4]. For ϵ equation, the modulation term must be modeled.

The proposed model of Amsden and O'Rourke [4] will be used here in association with the k equation. This model is assigned *Model* 2 in this study in which the extra term in ϵ equation is

$$S_{\epsilon,l} = C_3 \frac{\epsilon}{k} S_{k,l} \tag{II.101}$$

with $C_3 = 1.5$.

Substitution of equation (II.99) into (II.100) and taking average, we obtain the modulation term

$$S_{k,l} = \frac{1}{dV} \sum_{p=1}^{NP} [N_p \dot{m}_{ev,p} \overline{u_i'(v_i')_p} - m_p N_p \overline{u_i'(\frac{u_i' - v_i'}{\tau})_p}] \tag{II.102}$$

Mostafa and Mongia [80] as well as Fashola and Chen [36] have proposed a simplified approach in which the interaction term $S_{ui,l}$ is linearized followed by multiplication of the fluctuation velocity u_i'. The turbulence modulation term then only involves the gas/droplet velocity fluctuation correlation $\overline{u_i'(u_i' - v_i')}$ in equation (II.102) for non-evaporating sprays. This correlation is then modeled through gas kinetic energy k, and eddy and particle time scales, t_l and t_d,

$$\overline{u_i'(u_i' - v_i')} = 2k \ f(t_l, t_d) \tag{II.103}$$

In Mostafa and Mongia's model [80] (*Model* 1 in this study), the correction function f takes the form

$$f(t_l, t_d) = 1 - \frac{t_l}{t_l + t_d} \tag{II.104}$$

where t_l is the gas phase Lagrangian time scale given by

$$t_l = 0.35 \ \frac{k}{\epsilon} \tag{II.105}$$

and t_d is same as the particle relaxation time τ defined in equation (II.33).

Following approach of Chen and Wood [22] (*Model* 3 in this study) employed in their two-fluid model, we use the function

$$f(t_l, t_d) = 1 - exp(-\frac{t_d}{t_l}) \tag{II.106}$$

where

$$t_l = 0.5\ \frac{k}{\epsilon} \tag{II.107}$$

and

$$t_d = \frac{\rho_d\ d_p^2}{18\rho\mu} \tag{II.108}$$

The extra term in k equation is summarized as followings for non-evaporating spray,

$$S_{k,l} = -\sum_{p=1}^{NP} \frac{3}{4}\frac{\rho}{d_p} C_D |u_i - v_i|_p\ \frac{4}{3}\pi {r_p}^3 N_p\ 2k\ f(t_l, t_d)/dV \tag{II.109}$$

The corresponding extra term $S_{\epsilon,l}$ in ϵ equation is modeled as equation (II.101) with constant $C_3 = 1.0$. In *Model* 1 and 3, effects of different turbulence time scales with respect to particle relaxation times are incorporated in the modulation terms. Furthermore, this model simplifies evaluation of the dispersed-phase source terms in two-phase flows.

Based on the above modulation models, the modulation terms appearing in k equation, $S_{k,l}$, have negative values all the time, hence the presence of particle-phase will damp the gas-phase kinetic energy and affect the turbulence structure.

II.3.8 Droplet Breakup Model

The present study employs two breakup models including Reitz's wave instability model [95] and TAB (Taylor Analogy Breakup) model of O'Rourke and Amsden [89].

Reitz's model

Based on the concept that the atomization of the injected liquid and subsequent breakup of drops are indistinguishable processes within a dense spray [96], Reitz and Diwaker developed a droplet breakup model. This model was extended by Reitz [95] with adding new parcels containing fine product drops to the computation as the blobs break up. Atomization is modeled using injected "blobs", which have the same sizes as the nozzle exit diameter. The breakup of the blobs and the resulting drops are modeled using a wave stability analysis for liquid jets. The wavelength of fastest growing wave, Λ and the maximum wave growth rate, Ω can be determined by the curve-fitted formula which are obtain from the numerical solutions of the surface wave dispersion equation for a round jet.

$$\frac{\Lambda}{a} = 9.02\frac{(1+0.45Z^{0.5})(1+0.40T^{0.7})}{(1+0.87We_g^{1.67})^{0.6}} \tag{II.110}$$

$$\Omega\left(\frac{\rho_d a^3}{\alpha}\right)^{0.5} = \frac{0.34+0.38We_g^{1.5}}{(1+Z)(1+1.4T^{0.6})} \tag{II.111}$$

where

$W = |U + u' - v|$ — gas-droplet relative velocity

$Z = \frac{\sqrt{We_l}}{Re_l}$ — liquid Ohnesorge number

$We_l = \frac{\rho_d a W^2}{\alpha}$ — liquid Weber number

$We_g = \frac{\rho a W^2}{\alpha}$ — gas Weber number

$Re_l = \frac{\rho_d a\ W}{\mu_l}$ — liquid Reynolds number

$T = Z\sqrt{We_g}$

a — liquid jet radius ; α — droplet surface tension

The mean product drop size and drop breakup rate are given by

$$r = \begin{cases} B_o\Lambda & \text{if } B_o\Lambda \leq a \\ min \begin{cases} (3\pi a^2 W/2\Omega)^{0.33} \\ (3a^2\Lambda/4)^{0.33} \end{cases} & \text{if } B_o\Lambda > a \end{cases} \tag{II.112}$$

and

$$\frac{da}{dt} = -\frac{(a-r)}{\tau_b} \tag{II.113}$$

where

$$\tau_b = 3.726 B_1 a/\Lambda\Omega \tag{II.114}$$

Here, B_o is 0.61 and B_1 is the breakup time constant. a is the radius of the liquid jet or the blob. The secondary breakup is assumed to be governed by the same equations for the primary jet breakup. The finer drop parcel is generated when its mass reaches 20 % of the parent drop mass. The breakup constant $B_1 = 10$ is used for atomization process, and as suggested by O'Rourke and Amsden [89] $B_1 = 1.73$ is employed for droplet secondary breakup.

TAB Model

The TAB model of O'Rourke and Amsden [89] is based on an analogy between an oscillating and distorting droplet and a spring-mass system. The restoring force of the spring is analogous to the surface tension forces. The external force on the mass is analogous to the gas aerodynamic force. The damping forces due to liquid viscosity are introduced to this analogy.

Based on the TAB model, the equation for the acceleration of the droplet distortion parameter is

$$\frac{d^2y}{dt^2} = \frac{2}{3}\frac{\rho}{\rho_d}\frac{(U+u'-v)^2}{r^2} - \frac{8\alpha(T_d)}{\rho_d r^3}y - \frac{5\mu_l(T_d)}{\rho_d r^2}\frac{dy}{dt} \tag{II.115}$$

where the quantity y is proportional to the displacement of the droplet's surface from its equilibrium position, divided by the droplet radius. α and μ_l are the liquid surface tension coefficient and viscosity respectively at the droplet temperature. After integrating equation (II.115), we have

$$y(t) = \frac{We}{12} + exp(-\frac{t}{t_d})[(y(0) - \frac{We}{12}\cos\omega t + \frac{1}{\omega}(\dot{y}(0) + \frac{y(0) - \frac{We}{12}}{t_d})\sin\omega t] \quad \text{(II.116)}$$

where

$$We = \frac{\rho(U + u' - v)^2 r}{\alpha} \quad \text{(II.117)}$$

is the Weber number,

$$t_d = \frac{2}{5}\frac{\rho_d r^2}{\mu_l} \quad \text{(II.118)}$$

is the viscous damping time, and

$$\omega^2 = 8\frac{\alpha}{\rho_d r^3} - \frac{1}{t_d^2} \quad \text{(II.119)}$$

is the square of the oscillation frequency.

The droplet oscillation and breakup calculations require two normalized particle arrays(y, deformation and $\frac{dy}{dt}$, oscillation) which can be determined by the above equations. Droplet breakup occurs if and only if $y(t)$ is greater than unity. Occurrence of droplet breakup, the Sauter mean radius(SMR), and oscillation velocity for the product drop depend on these two parameters and Weber number. The radius of the product drops is then chosen randomly from a χ -squared distribution with calculated SMR, which is given by the following relation:

$$SMR = \frac{r}{\frac{7}{3} + \frac{1}{8}\frac{\rho_d r^3}{\alpha}(\frac{dy}{dt})^2} \quad \text{(II.120)}$$

where r is the parent droplet radius and α is the droplet surface tension. Following breakup, the product drop has the same temperature with the parent drop, and its deformation and oscillating parameters are set to zero.

II.3.9 Droplet Collision Model

The drop collision model suggested by O'Rourke [87] is employed to calculate collision and coalescence among the dispersed liquid phase. The collision routine is operating for the pair of particles if, and only if, they are in the same computational cell. For the collision calculation, the drops associated with each computational parcel are considered to be uniformly distributed throughout the computational cell where they are located. For all parcels in each computational cell, a collision frequency between the parcel($parcel_1$) of larger drop radius(r_1) and the parcel($parcel_2$) of smaller drop radius(r_2) is obtained from the relationship in terms of the number of drops in $parcel_2$, the relative velocity between $parcel_1$ and $parcel_2$, the area based on $r_1 + r_2$, and the volume of computational cell. Such a frequency ν is expressed as

$$\nu = \frac{N_2^n}{dV^n}\pi(r_1^n + r_2^n)^2|v_1 - v_2| \tag{II.121}$$

The probability P for n collisions is assumed to follow a Poisson distribution based on a collision frequency and the computational time step Δt.

$$P_n = e^{-\overline{n}}\frac{\overline{n}^n}{n!} \tag{II.122}$$

where the mean value $\overline{n} = \nu\Delta t$ and the collision frequency is defined in equation (II.121).

Using the probability informations, the collision impact parameters are stochastically calculated. If the collision impact parameter is less than a critical impact parameter, the outcome of every collision is coalescence. Otherwise, each collision is a grazing collision. The critical impact parameter depends on the drop radii, the relative velocity between drops, and the liquid surface tension coefficient.

Suppose the outcome of the collision is coalescence. For each collector drop, n droplets are subtracted from their associated parcel, and the size, velocity, and temperature of the collector parcel are appropriately modified. If there is not enough number of droplet to have n coalescences with each collector, then n is recalculated so that all N_2^n droplets coalesce, and the parcel associated with these droplets is destroyed.

If the outcome of each collision is a grazing collision, only one collision is calculated for each parcel. Grazing collisions usually occur between drops of nearly equal size and are calculated between N pairs of drops, where

$$N = min(N_1^n, N_2^n) \tag{II.123}$$

The droplets maintain their sizes and temperatures but undergo velocity changes.

II.4 Summary of Two-Phase Interaction Source Terms

The two-phase interaction source terms in the governing equations can be summarized as :

$$S_{m,l} = \frac{1}{dV}\sum_{p=1}^{NP} N_p \dot{m}_{ev,p} \tag{II.124}$$

$$S_{ui,l} = \frac{1}{dV}\sum_{p=1}^{NP}[N_p \dot{m}_{ev,p}(v_i)_p - m_p N_p(\frac{U_i + u_i' - v_i}{\tau})_p] \tag{II.125}$$

$$S_{h,l} = \frac{1}{dV}\sum_{p=1}^{NP}\{N_p \dot{m}_{ev,p}(h_p - L + \frac{1}{2}v_i^2) - m_p N_p(C_{p,d}\frac{dT_p}{dt} + \frac{dv_i}{dt}v_i)\} \tag{II.126}$$

where

$$(\frac{dv_i}{dt})_p = \frac{U_i + u_i' - v_i}{\tau} + F_{bi} \tag{II.127}$$

and the particle mass

$$m_p = \frac{4}{3}\pi r_p^3 \rho_d \tag{II.128}$$

The droplet evaporation rate can be expressed as:

$$\dot{m}_{ev} = \frac{4}{3}\pi \rho_d \frac{(r_p^{n+1})^3 - (r_p^n)^3}{\Delta t} \tag{II.129}$$

Turbulence modulation terms in k and ϵ equations take the following forms,

Model 2 (Amsden and O'Rourke [4]):

$$S_{k,l} = \overline{u_i' S_{ui,l}} \tag{II.130}$$

$$S_{\epsilon,l} = 1.5\frac{\epsilon}{k} S_{k,l} \tag{II.131}$$

Model 1 (Mostafa and Mongia [80]) and *Model* 3 (Chen and Wood [22]):

$$S_{k,l} = -\sum_{i=1}^{NP}\frac{3}{4}\frac{\rho}{d_p}C_D|u_i - v_i|_p \ \frac{4}{3}\pi {r_p}^3 N_p \ 2k \ f(t_l, t_d)/dV \tag{II.132}$$

$$S_{\epsilon,l} = 1.0\frac{\epsilon}{k}S_{k,l} \tag{II.133}$$

The velocity fluctuation correlation function is defined in section (II.3.7).

Here, dV denotes the volume of the computational cell and h_p and L are the droplet enthalpy and the latent heat of the droplet, respectively.

III

Numerical Procedure

III.1 Introduction

The governing equations of the gas phase are solved using a control-volume based finite-difference method on an unsteady fashion. Spatial differences are formed on a curvilinear general coordinate with all gas field variables stored at the same grid point. Second order accurate central differencing scheme is used for the diffusion terms and high order Chakravarthy-Osher scheme [19] with damping is used for the convection terms. The transient solution is marched forward in a sequence of finite time increments. The implicitly coupled pressure and velocity equations are solved by the $M - PISO$ algorithm[55], with individual equations being solved by the conjugate gradient squared(CGS) [29] method. In the PISO algorithm, each time step is divided into a one-predictor two-corrector sequence.

The strong coupling terms between particle and gas are evaluated by the same time splitting technique. Implicit coupling procedures are used to treat momentum exchanges to avoid the the limitation of small time-steps.

Accurate calculation of mass and heat transfer is achieved by automatic reductions in the timestep when the exchange rate becomes large. For droplet/turbulence interaction calculations, integration time step is compared to the turbulent eddy life

time. If the time step is smaller than the eddy life time, a fluctuating component is added to the local mean gas velocity when calculating each particles mass, momentum, and energy exchange with the gas. If the time step exceeds the eddy life time, changes in droplet position and velocity due to turbulence are chosen randomly from the probability distributions for these changes as described by O'Rourke[88].

The unsteady solution procedure described above is different from the conventional *PSIC* (Particle Source In Cell) procedure [28] in which global iterations are required between two phases. The method used here is time-accurate and is very computational efficient. This unsteady procedure can also be used for steady state calculations where the statistically steady solutions are sought. Detailed descriptions of the current method are given in section (III.5).

III.2 Statistical Particle Model

In this model, spray is represented by discrete particles, rather than by continuous distributions. A finite number of computational particles are used to predict a sample of total population of particles. Using the statistical or Monte Carlo formulation, each computational particle is considered to represent a group of particles having the same characteristics such as number N_p, size r_p, velocity v_p, location x_p and temperature T_d. The discrete particle distribution function f is used to approximate the continuous distribution,

$$f = \sum_{p=1}^{NP} N_p \delta(x - x_p)\delta(v - v_p)\delta(r - r_p)\delta(T - T_d)/dV \qquad \text{(III.1)}$$

Particle trajectories are integrated using its motion and momentum equations (II.32,II.36) and particles exchange mass, momentum and energy with the gas within the computational cell in which they are located. By re-arrangement of two phase

momentum interaction terms, this method consists of a fully-interacting combination of Eulerian fluid and Lagrangian particle calculations. The interaction calculations are performed simultaneously and eliminate global iteration for the two-phase momentum exchange. This procedure improves numerical stability and is efficient for transient calculation. Dukowicz [31] firstly proposed this numerical procedure and used a random turbulence model to simulate unsteady spray jets.

In the stochastic particle method, a Monte Carlo technique is employed for direct simulation of spray characteristics. Droplets are sampled randomly from assumed probability distribution functions that govern droplet properties and droplet behavior subsequent to injection. The sampling procedures include injection droplet size and velocity, gas turbulent fluctuating velocity, droplet breakup and droplet collision. This procedure is summarized as following.

In the direct simulation of Monte Carlo procedures, first we need to find a table of successive random fractions R_f that are uniformly distributed between 0 and 1. This random number can be generated as a standard function on computers or from some algorithms.

Suppose we are given the droplet number distribution function $f(r)$ corresponding to the random radius r ($r_1 \leq r \leq r_2$). The droplet number dN in the interval dr about the radius r will be

$$dN = f(r)\ dr \tag{III.2}$$

We define the random variable

$$r_f = \int_{r_1}^{r} f(r')dr' \tag{III.3}$$

and we know that $dN = dr_f$. So, the number of droplets is uniformly distributed

with respect to the variable r_f. If we normalize function r_f by

$$\int_{r_1}^{r_2} f(r')dr' \tag{III.4}$$

and define

$$R_f = \int_{r_1}^{r} f(r')dr' / \int_{r_1}^{r_2} f(r')dr' \tag{III.5}$$

Hence, R_f will be distributed also from zero to one, and then we invert R_f to obtain r, which then will be distributed according to $f(r)$. If the form of the distribution function $f(r)$ is easy to integrate and its integration is easy to invert, we can perform this process analytically. Otherwise, we have to use a numerical method.

The following examples illustrate how these processes work. Consider the droplet radius r distributed between 0 and a such that the probability of r is proportional to r. Now

$$f(r) = r \tag{III.6}$$

and

$$r_f = \int_0^r r dr = \frac{1}{2}r^2 \tag{III.7}$$

Normalized function R_f will be

$$R_f = \frac{r^2}{a^2} \tag{III.8}$$

Its inversion is

$$r = a\sqrt{R_f} \tag{III.9}$$

Unfortunately, the above procedure can only be used when it is possible to obtain an explicit function for r.

Let us consider gas turbulent fluctuating velocity component u'. Due to the hypothesis of isotropic gas phase turbulence, u' is distributed according to the Gaussian

distribution

$$f(u') = \frac{1}{\sqrt{2\pi}\sigma} exp(-\frac{u'^2}{2\sigma^2}) \tag{III.10}$$

where, σ is the standard deviation given by:

$$\sigma = \sqrt{\frac{2}{3}k} \tag{III.11}$$

and k is the gas turbulent kinetic energy. Its integration will be

$$R_f = \int_{-\infty}^{u'} \frac{1}{\sqrt{2\pi}\sigma} exp(-\frac{u'^2}{2\sigma^2}) du' = \frac{1}{2} + \frac{1}{2} erf(u'/\sqrt{4k/3}) \tag{III.12}$$

It follows that the error function erf must be inverted to obtain u',

$$u' = \sqrt{4k/3} erf^{-1}(2R_f - 1) \tag{III.13}$$

or

$$u' = \sqrt{4k/3} sign(2R_f - 1) erf^{-1}(|2R_f - 1|) \tag{III.14}$$

where *sign* is a FORTRAN function which takes the sign of a variable.

We store the values of the inverse error function $erf^{-1}(R_f)$ in an array with an intervals of 0.05 from $R_f = 0.0$ to $R_f = 1.0$. The maxima value of $erf^{-1}(R_f)$, $erf^{-1}(1.0)$, is infinite and approximated to be $erf^{-1}(0.99532) = 2.0$ without significant effect on calculation of u', because values of uniform distribution random function R_f exceeding 0.99532 have very small probability. Values of $erf^{-1}(R_f)$ at intermediate values of R_f are obtained by linear interpolation. A new u' is only sampled once every particle-eddy interaction time t_{int}.

III.3 Splitting of Two-Phase Momentum Interaction Source Term

To improve the convergence and the numerical stability, the momentum interaction source term, $S_{ui,l}$ can be treated implicitly. The particle momentum equation (II.32)

can be discretized as

$$\frac{v_i^{n+1}-v_i^n}{\Delta t}=\frac{U_i^{n+1}+u_i'-v_i^{n+1}}{\tau^{n+1}}+F_{bi} \tag{III.15}$$

and v_i^{n+1} can be analytically solved from the above equation,

$$v_i^{n+1}=\frac{v_i^n+(U_i^{n+1}+u_i'+F_{bi}\tau^{n+1})\frac{\Delta t}{\tau^{n+1}}}{1+\frac{\Delta t}{\tau^{n+1}}} \tag{III.16}$$

Thus,

$$\begin{aligned} U_i^{n+1}+u_i'-v_i^{n+1} &= \frac{(U_i^{n+1}+u_i')(1+\frac{\Delta t}{\tau^{n+1}})-[v_i^n+(U_i^{n+1}+u_i'+F_{bi}\tau^{n+1})\frac{\Delta t}{\tau^{n+1}}]}{1+\frac{\Delta t}{\tau^{n+1}}} \\ &= \frac{U_i^{n+1}+u_i'-F_{bi}\Delta t-v_i^n}{1+\frac{\Delta t}{\tau^{n+1}}} \end{aligned} \tag{III.17}$$

Two-phase momentum coupling term (II.125) can be obtained by substituting the above relation (III.17)

$$\begin{aligned} S_{ui,l}^{n+1} &= \frac{1}{dV}\sum_{p=1}^{NP}[N_p\dot{m}_{ev,p}(v_i)^n{}_p-m_pN_p(\frac{U_i^{n+1}+u_i'-v_i^{n+1}}{\tau^{n+1}})_p] \\ &= \frac{1}{dV}\sum_{p=1}^{NP}\frac{4}{3}\pi\rho_dN_p[\frac{(r_p^n)^3-(r_p^{n+1})^3}{\Delta t}(v_i)^n{}_p-\frac{\frac{1}{\tau^{n+1}}}{1+\frac{\Delta t}{\tau^{n+1}}}(r_p^{n+1})^3 \\ &\quad \cdot(U_i^{n+1}+u_i'-F_{bi}\Delta t-v_i^n)] \\ &= \frac{1}{dV}\sum_{p=1}^{NP}\frac{\frac{4}{3}\pi\rho_dN_p}{\Delta t}\{(r_p^n)^3(v_i)^n{}_p-\frac{(r_p^{n+1})^3}{1+\frac{\Delta t}{\tau^{n+1}}} \\ &\quad \cdot[(U_i^{n+1}+u_i'-F_{bi}\Delta t)\frac{\Delta t}{\tau^{n+1}}+v_i^n]\} \end{aligned} \tag{III.18}$$

We then split $S_{ui,l}^{n+1}$ into the following expression,

$$S_{ui,l}^{n+1}=-S_{pi}U_i^{n+1}+R_{pi} \tag{III.19}$$

Here, S_p and R_p are obtained by comparing equation(III.18) and equation(III.19),

$$S_{pi}=\frac{1}{dV}\sum_{p=1}^{NP}\frac{\frac{4}{3}\pi\rho_dN_p}{\tau^{n+1}}\frac{(r_p^{n+1})^3}{1+\frac{\Delta t}{\tau^{n+1}}} \tag{III.20}$$

$$R_{pi} = \frac{1}{dV}\sum_{p=1}^{NP}\frac{\frac{4}{3}\pi\rho_d N_p}{\Delta t}\{(r_p^n)^3(v_i)^n{}_p - \frac{(r_p^{n+1})^3}{1+\frac{\Delta t}{\tau^{n+1}}}[(u_i' - F_{bi}\Delta t)\frac{\Delta t}{\tau^{n+1}} + v_i^n]\} \quad \text{(III.21)}$$

The parameters S_p and R_p are momentum control volume quantities depending on available particle information at previous and present timestep, and S_p is independent of directions. This splitting was firstly proposed by Dukowicz [31] for non-evaporating two-phase flows. It implicitly accounts for the present gas phase velocity to the two-phase coupling source term and enhances two-phase interactions. In strong two-way coupling calculations, its efficiency and numerical stability have been shown by Dukowicz [31] and the present study. For transient calculations, we combine this splitting and gas phase operator splitting together to obtain time accuracy solutions. This splitting enhances diagonal dominance of the momentum equation due to the positive S_p, and hence improves the numerical stability.

III.4 Droplet Evaporation Calculation

One of the advantages of Lagrangian method for liquid phase is its feasibility to handle polydispersed spray. Evaporation rates of various sizes of spray droplets can be calculated for each droplet, and then the two-phase interactions can be coupled by source terms. Droplet radius and temperature changes are calculated by evaporating droplets sequentially at constant pressure. In highly evaporating processes, such the high ambient temperature or for more volatile fuel, droplets will evaporate very quickly and small time step will be required to get reasonable numerical solution. To improve computational efficiency, following the numerical treatment of KIVA-II [4] a hybrid method is used in this study. Evaporation calculation of droplet is implicit in its temperature but explicit in the gas temperature and mass fraction.

Droplet evaporations are calculated one by one along their trajectories when they travel through the grid cells and gas phase temperature, pressure and mass fraction at the grid point are used as ambient properties. This sequential droplet evaporation and explicitness can produce unphysical results and numerical instability when heat and mass transfer rates to a single droplet are too large. In the KIVA-II's procedure, an evaporation sub time step δt_{ev} is estimated based on heat and mass transfer rates for each parcel of droplets and the evaporation calculation is subcycled with δt_{ev} to main time step Δt.

The choice for δt_{ev} is based on the idea that the heat or mass transfer between a computational particle and its surrounding gas phase at the same grid point in one time step should not exceed some fraction of energy or mass available for transfer. This fraction is specified to be 0.5 here. This criterion can be expressed as

$$\delta t_{ev} \leq \frac{\rho dV}{\mu Sh\ 4\pi r_p N_p} \tag{III.22}$$

Rearranging equation (II.39), we have droplet size change equation

$$\frac{dr_p^2}{dt} = -\frac{(\rho D) Sh\ ln(1+B_m)}{\rho_d} \tag{III.23}$$

and temperature change equation

$$\frac{dT_d}{dt} = \frac{K(T-T_d)Nu\frac{ln(1+B_m)}{B_m} - L(\rho D)Sh\ ln(1+B_m)}{\rho_d \frac{2}{3} r_p^2 C_{p,d}} \tag{III.24}$$

Where, Nusselt number Nu and Sherwood number Sh are given by

$$Nu = 2 + 0.6 Re_p{}^{\frac{1}{2}} Sc_d{}^{\frac{1}{3}} \tag{III.25}$$

and

$$Sh = 2 + 0.6 Re_p{}^{\frac{1}{2}} Pr_d{}^{\frac{1}{3}} \tag{III.26}$$

First, droplet energy equation is solved implicitly to update its temperature. The finite-difference approximation to equation(III.24) is

$$\frac{T_d^{\nu+1} - T_d^{\nu}}{\delta t_{ev}} = \frac{K^{\nu}(T - T_d^{\nu+1})(Nu)^{\nu}\frac{ln(1+B_m^{\nu+1})}{B_m^{\nu+1}} - L^{\nu}(\rho D)^{\nu}(Sh)^{\nu}ln(1+B_m^{\nu+1})}{\rho_d \frac{2}{3}(r_p^{\nu})^2 C_{p,d}^{\nu}} \tag{III.27}$$

where the superscript ν denotes the value of a quantity after ν evaporation subcycles. The Spalding number or mass transfer number B_m is calculated from the formula,

$$B_m^{\nu} = \frac{Y_s(T_d^{\nu+1}) - Y_{\infty}}{1 - Y_s(T_d^{\nu+1})} \tag{III.28}$$

Y_{∞} in equation (III.28) and T in equation (III.27) are intermediate values of ambient vapor mass fraction and gas temperature of the grid cell in which the droplet is located. They were explicitly updated due to evaporation of droplets with subscripts less than current particle index p and evaporation of this droplet on subcycle less than ν. The gas phase thermal conductivity K^{ν} and mass diffusivity $(\rho D)^{\nu}$ are calculated using T and T_d^{ν}. The droplet Reynolds number Re_p, Schmidt number Sc_p, and Prandtl number Pr_p are calculated using r_p^{ν}, T_d^{ν} and the intermediate gas temperature T. The finite difference equation (III.27) requires iterations since mass transfer number or droplet surface vapor mass fraction Y_s is a nonlinear function of droplet temperature T_d.

The droplet size change will be calculated following the implicit solution of equation (III.27) for $T_d^{\nu+1}$. The finite difference equation is

$$\frac{(r_p^{\nu+1})^2 - (r_p^{\nu})^2}{\delta t_{ev}} = -\frac{(\rho D)^{\nu}}{\rho_d} Sh^{\nu} \frac{ln(1+B_m^{\nu}) + ln(1+B_m^{\nu+1})}{2} \tag{III.29}$$

If the newly calculated droplet size $r_p^{\nu+1}$ is smaller than zero or temperature $T_d^{\nu+1}$ is greater than its critical temperature, the droplet radius will be set to zero and we will terminate the evaporation calculation for this droplet.

The intermediate gas temperatures and vapor mass fractions are calculated explicitly with droplet evaporation progressing. Three arrays related to gas mass, fuel vapor mass and gas enthalpy in grid cells are initialized as:

$$M_{ij} = \rho_{ij} dV_{ij} \tag{III.30}$$

$$(M_f)_{ij} = (\rho_f)_{ij} dV_{ij} \tag{III.31}$$

$$(\overline{MH})_{ij} = \rho_{ij} dV_{ij} h_{ij}. \tag{III.32}$$

Then as each droplet evaporating the above arrays are updated as

$$M_{ij} \leftarrow M_{ij} - \frac{4}{3}\pi\rho_d[(r_p^{\nu+1})^3 - (r_p^{\nu})^3]N_p \tag{III.33}$$

$$(M_f)_{ij} \leftarrow (M_f)_{ij} - \frac{4}{3}\pi\rho_d[(r_p^{\nu+1})^3 - (r_p^{\nu})^3]N_p \tag{III.34}$$

$$(\overline{MH})_{ij} \leftarrow (\overline{MH})_{ij} - \frac{4}{3}\pi\rho_d[(r_p^{\nu+1})^3 h_l^{\nu+1} - (r_p^{\nu})^3 h_l^{\nu}]N_p \tag{III.35}$$

$$+\frac{4}{3}\pi\rho_d[(r_p^{\nu+1})^3 - (r_p^{\nu})^3]N_p L^{\nu+1} \tag{III.36}$$

for the droplet located in the cell (i,j). Finally, the intermediate vapor mass fraction and gas temperature are calculated,

$$(Y_\infty)_{ij} = \frac{(M_f)_{ij}}{M_{ij}} \tag{III.37}$$

$$T_{ij} = T_{ij}^n + \frac{\frac{(\overline{MH})_{ij}}{M_{ij}} - H_{ij}^n}{(C_p)_{ij}^n}. \tag{III.38}$$

These new intermediate values are then used for the next calculation of droplet temperature and radius changes. We can get droplet evaporation rates and their contributions to energy equation due to evaporation after evaporation calculation is completed. Droplet mass evaporated is

$$dM_{ij} = \sum_{p=1}^{NP} \frac{4}{3}\pi\rho_d[(r_p^n)^3 - (r_p^{n+1})^3]N_p \tag{III.39}$$

Energy contribution is

$$\begin{aligned} dH_{ij} &= \sum_{p=1}^{NP}\{\frac{4}{3}\pi\rho_d[(r_p^n)^3(H_l)_{ij}^n - (r_p^{n+1})^3(H_l)_{ij}^{n+1}]N_p \\ &- \sum_{\nu}\frac{4}{3}\pi\rho_d[(r_p^\nu)^3 - (r_p^{\nu+1})^3]N_pL^{\nu+1}\} \end{aligned} \tag{III.40}$$

In the above equation (III.40), $\sum_\nu$ denotes that the summation is taken over all of the sub-time step δt_{ev}. Because the latent heat L^ν depends on the droplet temperature T_d^ν, we do not have such a relation:

$$\sum_{\nu}\frac{4}{3}\pi\rho_d[(r_p^\nu)^3 - (r_p^{\nu+1})^3]N_pL^{\nu+1} = \frac{4}{3}\pi\rho_d[(r_p^n)^3 - (r_p^{n+1})^3]N_pL^{n+1} \tag{III.41}$$

When implemented in the two-phase calculation, the droplet mass evaporation term $S_{m,l}$ and energy exchange term $S_{h,l}$ are employed as:

$$S_{m,l} = \frac{1}{dV}\sum_{p=1}^{NP}\frac{\frac{4}{3}\pi\rho_dN_p}{\Delta t}[(r_p^n)^3 - (r_p^{n+1})^3] \tag{III.42}$$

$$\begin{aligned} S_{h,l} &= \frac{1}{dV}\sum_{p=1}^{NP}\{\frac{\frac{4}{3}\pi\rho_dN_p}{\Delta t}[(r_p^n)^3(H_l)_{ij}^n - (r_p^{n+1})^3(H_l)_{ij}^{n+1}] \\ &- \sum_{\nu}\frac{\frac{4}{3}\pi\rho_dN_p}{\Delta t}[(r_p^\nu)^3 - (r_p^{\nu+1})^3]L^{\nu+1}\} \end{aligned} \tag{III.43}$$

III.5 Two-Phase Numerical Model

Due to the strong coupling and stiff source terms in the two-phase flow, successful numerical schemes must be stable, accurate and efficient. The spirits of Issa's [47] *PISO* algorithm and Dukowicz's [31] statistical and splitting techniques are combined and a new two-phase coupling scheme is proposed in the following sections.

III.5.1 The PISO Algorithm

The *PISO* (Pressure-Implicit with Splitting of Operators) algorithm [47] is a non-iterative method for handling the coupling of the implicitly discretized time-dependent single phase fluid flow and heat transfer equations. The method is based on the use of pressure and velocity as primitive variables and hence can be applied for the solutions of both incompressible and compressible versions of the transport equations. The main feature of the technique is to split the solution process into a series of predictor and corrector steps whereby operations on pressure are decoupled from those on velocity at each time step. Due to the splitting, the set of equations can be solved sequentially. At each time-step, time accurate solutions can be obtained by prescribed predictor and corrector steps. The accuracy of this splitting procedure is based on a linearized form of the discretized equations, and the analysis indicates that the numerical solution differs from the exact solution of the difference equations by terms proportional to the powers of the time-step- size. By virtue of this, it is possible to dispense with iterations and work faster for transient flow calculations. This efficient implicit scheme retains simplicity of implementation relative to block simultaneous methods which require much more computer memory and are not flexible to include extra physical models.

III.5.2 M-PISO and Gas Phase Solver

As pointed out by Jiang [55], the original *PISO* algorithm suffers some problems in splitting procedure and is not applicable to supersonic flows. A newly modified $M-$ *PISO* algorithm proposed by Jiang et al. [55, 56] has been successfully carried out for incompressible, transonic and supersonic flow calculations. The benchmark test

cases[55] include incompressible channel flow, driven cavity flow, vortex shedding, both laminar and turbulent backward facing step flows, and compressible flows over a bump and a spherical cylinder, nozzle flow and multiple shock reflections. $M-PISO$ algorithm is employed and improved in the present gas phase solver. The numerical details can be found in Jiang [55]. Main features are summarized as following,

1. General two-dimensional body-fitted coordinates.
2. Time accurate transient capability.
3. Conjugate Gradient Squared matrix solver.
4. All speed flow capability.
5. Pressure based method.
6. $k-\epsilon$ two equation turbulence model with wall functions.
7. Non-staggered grid arrangement.
8. Third order pressure damping term for face velocity calculation.
9. TVD scheme with damping term.
10. Cartesian velocity components solved.

III.5.3 Two-Way Coupling Scheme

The present study extended $M-PISO$ algorithm with more consistent updating in density variable and employed the concept of weak form transport equation [121]. The new procedure converged faster than our previous one [56] for compressible flows. A two-way coupling scheme is incorporated and presented in the following.

The implicit finite difference form of the gas phase governing equations described in Chapter II can be written as:

$$\frac{1}{\Delta t}(\rho^{n+1} - \rho^n) + \Delta_i(\rho U_i)^{n+1} = S_{m,l}^{n+1} \tag{III.44}$$

$$\frac{1}{\Delta t}[(\rho U_i)^{n+1} - (\rho U_i)^n] = H(U_i^{n+1}) - \Delta_i p^{n+1} + S_{u_i}^{n+1} + S_{u_i,l}^{n+1} \tag{III.45}$$

$$\frac{1}{\Delta t}[(\rho H_t)^{n+1} - (\rho H_t)^n] = G(H_t^{n+1}) + \frac{P^{n+1} - P^n}{\Delta t} + S_h^{n+1} + S_{h,l}^{n+1} + R_{fu}^{n+1} H_{com} \tag{III.46}$$

$$\frac{1}{\Delta t}[(\rho k)^{n+1} - (\rho k)^n] = K(k^{n+1}) + S_k^{n+1} + S_{k,l}^{n+1} \tag{III.47}$$

$$\frac{1}{\Delta t}[(\rho \epsilon)^{n+1} - (\rho \epsilon)^n] = L(\epsilon^{n+1}) + S_\epsilon^{n+1} + S_{\epsilon,l}^{n+1} \tag{III.48}$$

$$\frac{1}{\Delta t}[(\rho Y_f)^{n+1} - (\rho Y_f)^n] = I(Y_f^{n+1}) + S_{m,l}^{n+1} - R_{fu}^{n+1} \tag{III.49}$$

and

$$\frac{1}{\Delta t}[(\rho Y_{o_2})^{n+1} - (\rho Y_{o_2})^n] = J(Y_{o_2}^{n+1}) - s \cdot R_{fu}^{n+1} \tag{III.50}$$

where, the operators H, G, K, L, I and J stand for the finite-difference representations of the spatial convective and diffusive fluxes of momentum U_i, total enthalpy H_t, turbulence kinetic energy k, its dissipation rate ϵ, species mass fraction Y_f and Y_{o_2} respectively, and the operator Δ_i is the finite- difference equivalent of $\partial/\partial x_i$. The droplet source terms and combustion source terms are listed in section (II.4) and (III.4), and the splitting of momentum source term in section (III.3).

The operator H can be constructed from C-O TVD schemes with damping term for the convection terms [55] and the central difference scheme for diffusion terms.

Generally, it takes the form

$$H(U_i) = \sum_{m=1}^{nb} A_m U_{i,m} - A_p U_i \tag{III.51}$$

where suffix m is a grid node identifier and the summation is over all the neighboring nodes involved in the formulation of the finite-difference representation of the spatial fluxes. Suffix p is for the central point. To ensure better accuracy and stability of the overall scheme, the central (i.e., diagonal) element A_p of the operator H is separated and shifted to the left-hand side of the equation where it can be treated implicitly. The rest of the elements are retained on the right-hand side where they are treated explicitly in corrector stage equations. A new operator H' is defined as

$$H'(U_i) = H(U_i) + A_p U_i = \sum_{m=1}^{nb} A_m U_{i,m} \tag{III.52}$$

Thus, a general implicit discretized transport equation can be written as

$$(\frac{\rho^{n+1}}{\Delta t} + A_p)\Phi_p^{n+1} = \sum_{m=1}^{nb} A_m \Phi_m^{n+1} + \frac{(\rho\Phi_p)^n}{\Delta t} + S_\Phi \tag{III.53}$$

The link coefficients A_m and A_p are constructed so that all of them are positive and they are related as

$$A_p = \sum_{m=1}^{nb} A_m + (C_e^{n+1} - C_w^{n+1} + C_n^{n+1} - C_s^{n+1}) \tag{III.54}$$

where C_e^{n+1}, C_w^{n+1}, C_n^{n+1} and C_s^{n+1} are face mass fluxes divided by the cell volume at east, west, north and south side respectively. A weak form of the transport equation suggested by Yang et al. [121] is obtained by adding the continuity equation multiplied by the dependent variable,

$$-[\frac{\rho^{n+1} - \rho^n}{\Delta t} + (C_e^{n+1} - C_w^{n+1} + C_n^{n+1} - C_s^{n+1})] \cdot \Phi_p^{n+1} = -S_{m,l}\Phi_p^{n+1} \tag{III.55}$$

to the transport equation (III.53). If A_p is replaced by

$$A_p = \sum_{m=1}^{nb} A_m + S_{m,l} \tag{III.56}$$

the resultant weak form of the transport equation becomes:

$$(\frac{\rho^n}{\Delta t} + A_p)\Phi_p^{n+1} = \sum_{m=1}^{nb} A_m \Phi_m^{n+1} + \frac{(\rho\Phi_p)^n}{\Delta t} + S_\Phi \tag{III.57}$$

This weak form eliminates ρ^{n+1} term in the coefficient of Φ_p, hence ρ_i^{n+1} and Φ_i^{n+1} are decoupled. The weak form is very helpful for constructing pressure correction equation due to this decoupling. The possible reason is that the term $(\rho U_i)^{n+1}$ in the coefficient of U_i^{n+1} in the non-weak form represents a non-linear relation and may result numerical instability. Our previous numerical experiences with variable density calculations also show that the stability is enhanced for scalar transport equations by setting ρ^{n+1} term to ρ^n in the coefficient of Φ_p for steady state calculations.

Present discretization is based on the explicit treatment of convective mass fluxes in transport equation,

$$\frac{\partial(\rho\Phi)}{\partial t} + \frac{\partial}{\partial x_j}[(\rho U_j)^n \Phi^{n+1}] = \frac{\partial}{\partial x_i}(\Gamma \frac{\partial \Phi^{n+1}}{\partial x_i}) + S_\Phi \tag{III.58}$$

This explicit treatment avoids frequent calculation of coefficients, results a simple pressure correction equation and is numerically efficient. More investigations should be done for convection term treatment especially in time accurate transient calculation of compressible flow and combustion process. The first term in the above equation is discretized as

$$\frac{\partial(\rho\Phi)}{\partial t} = \frac{\rho^n \Phi^{n+1} - \rho^{n-1}\Phi^n}{\Delta t} \tag{III.59}$$

to keep equation (III.58) satisfy Galilean transformation when a constant velocity or temperature is added.

The weak form equation (III.53) of the explicit convective flux treatment becomes:

$$(\frac{\rho^{n-1}}{\Delta t} + A_p)\Phi_p^{n+1} = \sum_{m=1}^{nb} A_m \Phi_m^{n+1} + \frac{\rho^{n-1}\Phi_p^n}{\Delta t} + S_\Phi \qquad \text{(III.60)}$$

The two-phase momentum coupling source terms are listed again,

$$S_p^{n+1} = \frac{1}{dV}\sum_{p=1}^{NP} \frac{\frac{4}{3}\pi\rho_d N_p}{\tau^{n+1}} \frac{(r_p^{n+1})^3}{1+\frac{\Delta t}{\tau^{n+1}}} \qquad \text{(III.61)}$$

$$R_{pi}^{n+1} = \frac{1}{dV}\sum_{p=1}^{NP} \frac{\frac{4}{3}\pi\rho_d N_p}{\Delta t}\{(r_p^n)^3 (v_i)^n{}_p - \frac{(r_p^{n+1})^3}{1+\frac{\Delta t}{\tau^{n+1}}}[(u_i' - F_{bi}\Delta t)\frac{\Delta t}{\tau^{n+1}} + v_i^n]\} \qquad \text{(III.62)}$$

and noting here, S_p is independent of directions.

Predictor Step

Momentum equation is solved implicitly in this step, using pressure, density and two-way coupling source term quantities evaluated at the previous time step.

$$(\frac{\rho^{n-1}}{\Delta t} + A_p)U_i^* = H'(U_i^*) - \Delta_i P^n + S_{ui} + \frac{\rho^{n-1}U_i^n}{\Delta t} - S_p^n U_i^* + R_{pi}^n \qquad \text{(III.63)}$$

Droplet injection, wall interaction, evaporation, breakup and collision can be activated. Sub-time scale δt_{ev} is used for droplet evaporation calculation. Due to the nonlinear relationship of mass transfer number B_m and droplet temperature T_d, droplet temperature T_d is solved iteratively using

$$\frac{T_d^{\nu+1} - T_d^\nu}{\delta t_{ev}} = \frac{K^\nu (T - T_d^{\nu+1}) Nu^\nu \frac{ln(1+B_m^{\nu+1})}{B_m^{\nu+1}} - L^\nu (\rho D)^\nu Sh^\nu ln(1+B_m^{\nu+1})}{\rho_d \frac{2}{3}(r_p^\nu)^2 C_{p,d}^\nu} \qquad \text{(III.64)}$$

The droplet size change will be calculated following the implicit solution of equation (III.64) for $T_p^{\nu+1}$,

$$(r_p^{\nu+1})^2 = (r_p^{\nu})^2 - \frac{(\rho D)^{\nu}}{\rho_d} Sh^{\nu} \frac{ln(1+B_m^{\nu}) + ln(1+B_m^{\nu+1})}{2} \delta t_{ev} \qquad \text{(III.65)}$$

At the same time, the source terms $S_{m,l}$ and $S_{h,l}$ are evaluated using equations (III.42) and (III.43). Particle velocity is updated,

$$v_i^* = \frac{v_i^n + (U_i^* + u_i' + F_{bi}\tau^n)\frac{\Delta t}{\tau^n}}{1 + \frac{\Delta t}{\tau^n}} \qquad \text{(III.66)}$$

These values of U_i^* and v_i^* are used to evaluate τ^*,S_p^* and R_p^* .

First Corrector Step

We calculate temperature T^* from relation

$$H_t^* = H^*(T) + \frac{1}{2} U_i^* U_i^* \qquad \text{(III.67)}$$

where total enthalpy H_t is obtained from energy equation. Density is updated using the equation of state,

$$\rho^{nT} = \frac{P^n}{RT^*} \qquad \text{(III.68)}$$

We approximate continuity equation as

$$\frac{\rho^* - \rho^n}{\Delta t} + \Delta_i(\rho^{nT} U_i^{**}) + \Delta_i(\rho' U_i^*) = S_{m,l} \qquad \text{(III.69)}$$

where

$$\rho^* = \frac{P^*}{RT^*} \qquad \text{(III.70)}$$

$$\rho' = \rho^* - \rho^{nT} = \frac{P^* - P^n}{RT^*} \qquad \text{(III.71)}$$

The momentum equation is approximated by

$$(\frac{\rho^{n-1}}{\Delta t} + A_p) U_i^{**} = H'(U_i^*) - \Delta_i P^* + S_i + \frac{\rho^{n-1} U_i^n}{\Delta t} - S_p^* U_i^{**} + R_{pi}^* \qquad \text{(III.72)}$$

By subtracting equation (III.63) from equation (III.72), we have

$$(\frac{\rho^{n-1}}{\Delta t} + A_p + S_p^*)(U_i^{**} - U_i^*) = -\Delta_i(P^* - P^n) - (S_p^* - S_p^n)U_i^* + R_{pi}^* - R_{pi}^n \quad \text{(III.73)}$$

Define the short notation

$$D_u^* = (\frac{\rho^{n-1}}{\Delta t} + A_p + S_p^*)^{-1} \quad \text{(III.74)}$$

Velocity U^{**} will be

$$U_i^{**} = U_i^* - D_u^*\Delta_i(P^* - P^n) - D_u^*[(S_p^* - S_p^n)U_i^* - (R_{pi}^* - R_{pi}^n)] \quad \text{(III.75)}$$

Substitution of equations (III.70,III.71,III.75) into equation (III.69) yields pressure correction equation,

$$\begin{aligned}[\frac{1}{\Delta t RT^*} + \Delta_i(\frac{U_i^*}{RT^*}) \quad - \quad \Delta_i(\rho^{nT} D_u^* \Delta_i)](P^* - P^n) = -[\frac{\rho^{nT} - \rho^n}{\Delta t} + \Delta_i(\rho^{nT} U_i^*)] \\ + \quad S_{m,l} + \Delta_i\{\rho^{nT} D_u^*[(S_p^* - S_p^n)U_i^* - (R_{pi}^* - R_{pi}^n)]\}\end{aligned} \quad \text{(III.76)}$$

The particle velocity at this level is then

$$v_i^{**} = \frac{v_i^n + (U_i^{**} + u_i' + F_{bi}\tau^*)\frac{\Delta t}{\tau^*}}{1 + \frac{\Delta t}{\tau^*}} \quad \text{(III.77)}$$

The values obtained at this level are used to calculate τ^{**}, S_p^{**}, R_p^{**}. At this stage, the mean velocity field satisfies the continuity constraint.

Second Corrector Step

To further satisfy the momentum conservation, a second corrector step is used. We again calculate temperature T^{**} from the relation

$$H_t^{**} = H^{**}(T) + \frac{1}{2}U_i^{**}U_i^{**} \quad \text{(III.78)}$$

Density is updated using the equation of state,

$$\rho^{*T} = \frac{P^*}{RT^{**}} \tag{III.79}$$

We approximate continuity equation as

$$\frac{(\rho^{**} - \rho^n)}{\Delta t} + \Delta_i(\rho^{*T} U_i^{***}) + \Delta_i(\rho' U_i^{**}) = S_{m,l} \tag{III.80}$$

where

$$\rho^{**} = \frac{P^{**}}{RT^{**}} \tag{III.81}$$

$$\rho' = \rho^{**} - \rho^{*T} = \frac{P^{**} - P^*}{RT^{**}} \tag{III.82}$$

The momentum equation is approximated by

$$(\frac{\rho^{n-1}}{\Delta t} + A_p)U_i^{***} = H'(U_i^{**}) - \Delta_i P^{**} + S_i + \frac{\rho^{n-1}U_i^n}{\Delta t} - S_p^{**}U_i^{***} + R_{pi}^{**} \tag{III.83}$$

By subtracting equation (III.72) from equation (III.83),

$$\begin{aligned}(\frac{\rho^{n-1}}{\Delta t} + A_p + S_p^{**})(U_i^{***} - U_i^{**}) &= H'(U_i^{**} - U_i^*) - \Delta_i(P^{**} - P^*) \\ &- (S_p^{**} - S_p^*)U_i^{**} + R_{pi}^{**} - R_{pi}^*\end{aligned} \tag{III.84}$$

Define the short notation

$$D_u^{**} = (\frac{\rho^{n-1}}{\Delta t} + A_p + S_p^{**})^{-1} \tag{III.85}$$

Velocity U^{***} will be

$$U_i^{***} = U_i^{**} - D_u^{**}\Delta_i(P^{**} - P^*) - D_u^{**}[(S_p^{**} - S_p^*)U_i^{**} - (R_{pi}^{**} - R_{pi}^*)] \tag{III.86}$$

Substitution of equations (III.81, III.82, III.86) into equation (III.80) yields pressure correction equation,

$$\begin{aligned}[\frac{1}{\Delta t RT^{**}} &+ \Delta_i(\frac{U_i^{**}}{RT^{**}}) - \Delta_i(\rho^{*T} D_u^{**}\Delta_i)](P^{**} - P^*) = -[\frac{\rho^{*T} - \rho^n}{\Delta t} + \Delta_i(\rho^{*T} U_i^{**})] \\ &+ S_{m,l} - \Delta_i[\rho^{*T} D_u^{**} H'(U_i^{**} - U_i^*)] \\ &+ \Delta_i\{\rho^{*T} D_u^{**}[(S_p^{**} - S_p^*)U_i^{**} - (R_{pi}^{**} - R_{pi}^*)]\}\end{aligned} \tag{III.87}$$

At this stage, the mean velocity field satisfies the continuity constraint.

Following [47], it can be shown that the errors introduced by the operator- splitting procedure is less than the truncation errors of the finite difference scheme used in the governing equations (III.45) and (III.15). Note that the effective relaxation time τ depends on the drag function which should contain the effects of turbulence. We therefore calculate $(u_i')^*$ at this stage by a stochastic method with the $k-\epsilon$ turbulence model. An one-predictor (implicit)/one-correction (explicit) procedure for k and ϵ equations suggested by Issa [47] has been used in this study. We then let U_i^{***} and P^{**} be the value at t^{n+1} level and add the $(u_i')^*$ to update the final time level particle velocities using the equation :

$$v_i^{n+1} = v_i^{***} = \frac{v_i^n + [U_i^{***} + (u_i')^* + F_{bi}\tau^{**}]\frac{\Delta t}{\tau^{**}}}{1+\frac{\Delta t}{\tau^{**}}} \tag{III.88}$$

The particle location is updated,

$$x_i^{n+1} = x_i^n + v_i^{n+1}\Delta t \tag{III.89}$$

This brings all variables to the new time level. The time is then incremented and the new predictor-corrector procedure is repeated with the new velocities. This algorithm is used for simulation of transient phenomena. If only a statistically steady solution is desired, then the time steps for gas phase and particle phase can be made unequal ; also the corrector stages of v_i (III.77 and III.88) may be neglected.

Scalar Equations

After continuity equation

$$\frac{1}{\Delta t}(\rho^{n+1} - \rho^n) + \Delta_i(\rho U_i)^{n+1} = S_{m,l}^{n+1} \tag{III.90}$$

is satisfied, we use the following weak form equation for scalars, such as energy, species mass fraction and turbulent kinetic energy and its dissipation rate,

$$\frac{\rho^{n+1}\Phi^{n+1}-\rho^{n}\Phi^{n}}{\Delta t}+\frac{\partial}{\partial x_j}[(\rho U_j)^{n+1}\Phi^{n+1}]=\frac{\partial}{\partial x_i}(\Gamma\frac{\partial\Phi^{n+1}}{\partial x_i})+S_\Phi \tag{III.91}$$

Its discretized weak form is

$$(\frac{\rho^n}{\Delta t}+A_p)\Phi^{n+1}=\sum_{m=1}^{nb}A_m\Phi_m^{n+1}+\frac{\rho^n}{\Delta t}\Phi^n+S_\Phi \tag{III.92}$$

where the central point coefficient

$$A_p=\sum_{m=1}^{nb}A_m+S_{m,l} \tag{III.93}$$

The k and ϵ discrete equations in the weak form are

$$(\frac{\rho^n}{\Delta t}+C_p)k^{n+1}=K'(k^{n+1})+\frac{\rho^n k^n}{\Delta t}+(\mu_t G)^{n+1}-(\rho\epsilon)^{n+1}+S_{k,l} \tag{III.94}$$

and

$$(\frac{\rho^n}{\Delta t}+D_p)\epsilon^{n+1}=L'(\epsilon^{n+1})+\frac{\rho^n\epsilon^n}{\Delta t}+(C_1\mu_t G\epsilon/k)^{n+1}-(C_2\rho\epsilon^2/k)^{n+1}+S_{\epsilon,l} \tag{III.95}$$

where

$$K'(k^{n+1})=\sum_{m=1}^{nb}C_m k_m^{n+1} \tag{III.96}$$

$$L'(\epsilon^{n+1})=\sum_{m=1}^{nb}D_m\epsilon_m^{n+1} \tag{III.97}$$

$$C_p=\sum_{m=1}^{nb}C_m+S_{m,l} \tag{III.98}$$

$$D_p=\sum_{m=1}^{nb}D_m+S_{m,l} \tag{III.99}$$

By invoking the eddy viscosity formulation:

$$\mu_t=C_\mu\rho\frac{k^2}{\epsilon} \tag{III.100}$$

the source terms S_k and S_ϵ are transformed into the forms

$$S_k = (\mu_t G)^{n+1} - (\frac{\rho^2 C_\mu}{\mu_t} k^2)^{n+1} \tag{III.101}$$

and

$$S_\epsilon = (C_1 C_\mu G \rho k)^{n+1} - (C_2 C_\mu \rho^2 \frac{k}{\mu_t} \epsilon)^{n+1} \tag{III.102}$$

Substitution of those changes, k and ϵ equations become

$$(\frac{\rho^n}{\Delta t} + C_p + \frac{\rho^2 C_\mu}{\mu_t^{n+1}} k^{n+1}) k^{n+1} = K'(k^{n+1}) + \frac{\rho^n k^n}{\Delta t} + (\mu_t G)^{n+1} + S_{k,l} \tag{III.103}$$

and

$$(\frac{\rho^n}{\Delta t} + D_p + C_2 C_\mu \rho^2 \frac{k^{n+1}}{\mu_t^{n+1}}) \epsilon^{n+1} = L'(\epsilon^{n+1}) + \frac{\rho^n \epsilon^n}{\Delta t} + (C_1 C_\mu G \rho k)^{n+1} + S_{\epsilon,l} \tag{III.104}$$

Predictor Step

Decoupling the above equation as

$$(\frac{\rho^n}{\Delta t} + C_p + \frac{\rho^2 C_\mu}{\mu_t^n} k^n) k^* = K'(k^*) + \frac{\rho^n k^n}{\Delta t} + \mu_t^n G + S_{k,l} \tag{III.105}$$

and

$$(\frac{\rho^n}{\Delta t} + D_p + C_2 C_\mu \rho^2 \frac{k^*}{\mu_t^n}) \epsilon^* = L'(\epsilon^*) + \frac{\rho^n \epsilon^n}{\Delta t} + C_1 C_\mu G \rho^{n+1} k^* + S_{\epsilon,l} \tag{III.106}$$

Equations (III.103) and (III.104) are to be solved in that sequence and implicitly in k^* and ϵ^* respectively. Turbulent viscosity μ_t is then calculated from

$$\mu_t^* = C_\mu \rho^{n+1} \frac{k^{*2}}{\epsilon^*} \tag{III.107}$$

Corrector Step

The corrector equations for k and ϵ are explicit and can be written as

$$(\frac{\rho^n}{\Delta t} + C_p + \frac{\rho^2 C_\mu}{\mu_t^*} k^*) k^{**} = K'(k^*) + \frac{\rho^n k^n}{\Delta t} + \mu_t^* G + S_{k,l} \tag{III.108}$$

and

$$(\frac{\rho^n}{\Delta t} + D_p + C_2 C_\mu \rho^2 \frac{k^{**}}{\mu_t^*})\epsilon^{**} = L'(\epsilon^*) + \frac{\rho^n \epsilon^n}{\Delta t} + C_1 C_\mu G \rho^{n+1} k^{**} + S_{\epsilon,l} \qquad \text{(III.109)}$$

Subtracting equations (III.108 and III.109) from equations (III.105 and III.106) respectively, we have

$$k^{**} = (\frac{\rho^n}{\Delta t} + C_p + \frac{\rho^2 C_\mu}{\mu_t^*} k^*)^{-1}[(\frac{\rho^n}{\Delta t} + C_p + \frac{\rho^2 C_\mu}{\mu_t^n} k^n)k^* + (\mu_t^* - \mu_t^n)G] \qquad \text{(III.110)}$$

and

$$\begin{aligned} \epsilon^{**} &= (\frac{\rho^n}{\Delta t} + D_p + C_2 C_\mu \rho^2 \frac{k^{**}}{\mu_t^*})^{-1}[(\frac{\rho^n}{\Delta t} + D_p + C_2 C_\mu \rho^2 \frac{k^*}{\mu_t^n})\epsilon^* \\ &+ C_1 C_\mu G \rho^{n+1}(k^{**} - k^*)] \end{aligned} \qquad \text{(III.111)}$$

The new turbulent viscosity is obtained by

$$\mu_t^{**} = C_\mu \rho^{n+1} \frac{k^{**2}}{\epsilon^{**}} \qquad \text{(III.112)}$$

III.5.4 Summary of Solution Procedure

The numerical procedure implemented in the present MAST code is summarized as following,

- Predict gas-phase velocities.
- Calculate particle-phase properties.
    1. Inject particles.
    2. Find particle index with respect to grid points.
    3. Reflect particles if they cross the boundaries.
    4. Repeal particles which are out of calculation domain.

5. Calculate particle turbulent dispersion.
6. Calculate droplet breakup and collision.
7. Calculate droplet evaporation.
8. Calculate two-way coupling source terms.

- Correct momentum and temperature (two-steps).
- Update particle velocities and trajectories.
- Calculate species mass fractions.
- Calculate total enthalpy.
- Predict and correct turbulent kinetic energy and its dissipation rate.
- Modify boundary conditions.
- Go to the next time-step calculation.

III.6 Boundary Conditions

For two-phase flows, both boundary conditions for gas-phase and droplet-phase must be specified to complete the solutions.

III.6.1 Gas Phase Boundary Conditions

Inlet boundary condition

All dependent variables need to be specified at the inlet boundary. For incompressible flows, only pressure difference is required in calculations. Inlet pressure is obtained by linear extrapolation from inner point assuming same gradient. For

compressible flows, we need to specify pressure or stagnation pressure depending on subsonic or supersonic inlet. Detailed discussions can be found in Ref.[55].

Outlet boundary condition

All of the variables are extrapolated at outlet boundary except velocity components in incompressible flow. Outlet velocity components are corrected based on the law of mass conservation, and inlet mass and droplet evaporation mass for incompressible flows.

Symmetric boundary condition

There is no flow across the symmetric line or axisymmetric axis and the gradients of solution variables are specified to be zero.

Wall boundary condition

No-slip condition is applied at impermeable walls. All gas velocity component and species gradients are specified to be zero. Temperature or heat flux can be implemented at walls for energy equation. For turbulent flow, almost all of the solution variables change sharply at near wall region. There are two alternatives to treat this stiff boundary condition. One is to use very fine grid in the laminar sublayer and buffer zone regions resulting in massive increase for computation time and computer memory, this method can be found in the low Reynolds number model of Jones and Launder [58] . The efficient method is the wall function treatment of Launder and Spalding [70], which is employed in the present study.

Open boundary condition

Only pressure is specified at open boundary. The other variables are obtained from linear extrapolation.

III.6.2 Particle Phase Boundary Conditions

When particles are injected from a nozzle or atomizer, particle radius, temperature, density, velocity and mass flow rate need to be specified by experimental data, empirical correlations or testing data according to its operating conditions. These initial conditions are very important for spray dynamics, evaporation and combustion simulations. A lot of experimental studies have been conducted for various atomizers to establish empirical correlations for spray flow rate, cone angle, size distribution, and penetration length [72], which are effected by liquid properties, atomizer and running condition etc..

Injecting particle size

For dilute polydispersed sprays, particle radii are chosen from particle size distribution correlations, such as $\chi - squard$, Nukiyama-Tanasawa, or Rosin-Rammler distributions as described in Chapter II of Ref.[72]. If the injected computational particles and particle Sauter mean diameter, SMD or the related parameters are specified, we use the Monte Carlo method as described in section (III.2) to choose each computational particle size. Calculation of each physical particle in a practical spray is impossible for current computer power. Based on the present statistical model, each computational particle represents a group of physical particles which have the same characteristic values, such as radius, temperature and velocity. Only

a limited computational particles are traced and calculated. Usually there are two kinds of method to represent physical particles if particle mass flow rate, size and computational particle number are specified. The first one specifies the physical particle number N_p represented by each computational particle, and each computational particle has different mass

$$m_{cp} = \frac{4}{3}\pi(r_p)^3\rho_d N_p \tag{III.113}$$

Then, r_p is generated using the drop number distribution function. In the second method, each computational particle has the same mass and represents different physical particle number. The mass can be obtained as

$$m_{cp} = \frac{FLOWP \cdot \Delta t}{NPTS} \tag{III.114}$$

where $FLOWP$ is the particle mass flow rate and $NPTS$ is the computational particle number injected per time step. Then physical particle number can be calculated with the following relation,

$$N_p = \frac{\frac{4}{3}\pi(r_p)^3\rho_d}{m_{cp}} \tag{III.115}$$

and r_p is generated from the drop volume distribution function. The second method is adopted in this study.

For dense spray case, droplet breakup has to be considered. In the present study, both TAB model of O'Rourke and Amsden [89] and Reitz's [95] breakup model are incorporated. In these models, the injecting particle sizes are the same as nozzle characteristical size. Droplet breakup occurrence depends on slip velocity, oscillation velocity and Weber number.

In case of the droplet passage through the plane of symmetry, the mirror image of the droplet with the same instantaneous properties, physical dimensions and velocity vector, is injected into the flow field.

Droplet Wall Impingement

The wall impingement model adopts the jet treatment[38] and the empirical correlation approach [84]. The experimental data of Wachters and Westerling [118] can be numerically fitted in terms of the droplet Weber number before and after impact.

$$We_o = 0.678 We_i \; exp(-0.004415 We_i) \tag{III.116}$$

For $We_i \leq 80.0$, the drops do not disintegrate during impact and bounce from the surface while for $We_i > 80.0$, the disintegration produces a dispersion of the small drops on the surface. Thus, in case of $We_i > 80.0$, the jet model is used; in case of $We_i \leq 80.0$, the drops bounce from the surface and the normal velocity after impact can be calculated from the following equation,

$$V_o = V_i (We_o / We_i)^{0.5} \tag{11}$$

This wall impingement model is based on several assumptions such as extrapolation of the results with water drops at atmospheric conditions and at higher wall temperature, no breakup at impact, the neglect of the wall heat transfer, and the neglect of droplet interaction with a possible liquid wall film. Despite these limitations, the qualitative agreement for $We_i \leq 80.0$ and the good quantitative agreement for $We_i > 80.0$ have been reported.

Injecting Particle velocity

Ordinary atomizers produce a spray which is distributed in some cone angles with θ_1 and θ_2. Let θ_1 and θ_2 represent inner cone angle and outer angle respectively, so we have $\theta_1 \leq \theta_2$. If $\theta_1 = 0$, particles are distributed throughout its volume and we call this kind of spray as $solid - cone$ spray. Otherwise, if particles are concentrated at

the outer edge of a conical spray pattern with $\theta_1 \neq 0$ we call it $hollow - cone$ spray. If particle injection velocity V_{inj} and cone angles are specified from experimental data or empirical correlations and no more information can be used, we assume particles are uniformly distributed in the given cone angles. Axial velocity V_x and radial velocity V_r are chosen randomly from following expression,

$$\begin{aligned} \theta &= \theta_1 + (\theta_2 - \theta_1) R_f \\ V_x &= V_{inj} cos\theta \\ V_r &= V_{inj} sin\theta \end{aligned} \tag{III.117}$$

where R_f is a uniform distribution random function. For a swirling atomizer, particle velocity V_z at tangential direction also need to be specified.

IV

Results and Discussions

In this chapter several benchmark problems involving particle dispersions in homogeneous and inhomogeneous turbulent flows are studied to calibrate the stochastic method for particle-turbulence interactions, and to evaluate the present parcel PDF model. Non-evaporating transient and steady solid-cone sprays are used to test the models of dense spray effects including droplet breakup and collision. Turbulence modulation effect and the efficiency of parcel PDF model for a dense spray case are tested at a steady solid-cone spray. A transient hollow-cone spray shows complicated two-phase interactions. Transient evaporating and burning sprays incorporating droplet breakup model, evaporation model and eddy-breakup combustion model demonstrates the sophisticated structures of such polydispersed spray combustion. The predictions show reasonably agreements with available experimental results.

IV.1 Particle Turbulent Dispersion

IV.1.1 Nearly-Homogeneous Turbulent Dispersion

The particle dispersion experimental setup of Snyder and Lumley [113] in a grid-generated turbulent flow was used for evaluating the present particle dispersion model and parcel PDF model. The mean flow was uniform in the test region and

turbulence was also found to be nearly isotropic. Individual particles were isokinetically injected by air flow through the sampling tube and carried to the center of the tunnel. The particle concentration was so low that mean gas flow properties were not effected. The turbulence energy decay curves were presented as a function of axial position. In the present study, turbulent kinetic energy was obtained by averaging axial and transverse fluctuating velocity and was fitted to the measured correlation as:

$$k(x) = \frac{1.5U^2}{54.88 \cdot (\frac{x}{M} - 14)} \tag{IV.1}$$

where $U = 6.55m/s$ is the mean axial velocity, x is axial distance from the mesh, and $M = 0.0254m$ is the mesh size. The dissipation rate ϵ is calculated by differentation of the above relationship,

$$\epsilon(x) = -U\frac{dk}{dx} = \frac{1.5U^3}{54.88M \cdot (\frac{x}{M} - 14)^2} \tag{IV.2}$$

Particle pictures were taken at ten stations in the experiment, spaced logarithmically from $x/M = 68.4$ to 168.

Generally, particle motion in turbulent flow is governed by the coupled effects of the turbulent flow field, particle inertia and crossing trajectory. All the three effects could happen for the dispersion of heavy particles, while the dispersion of light particle is dominated by the effect of turbulent flow field where light particle is fully correlated with turbulent fluctuating. For the motion of heavy particles, due to the influence of the Earth's gravitational field, a particle's free fall velocity increases with its inertia, which results the crossing trajectory effects. So, both effects of inertia and crossing trajectory are coupled together and hard to separate. In this experiment, particle densities and sizes are chosen to examine the three effects. For the light particle (hollow glass) with the effect of turbulent flow, the eddy lifetime

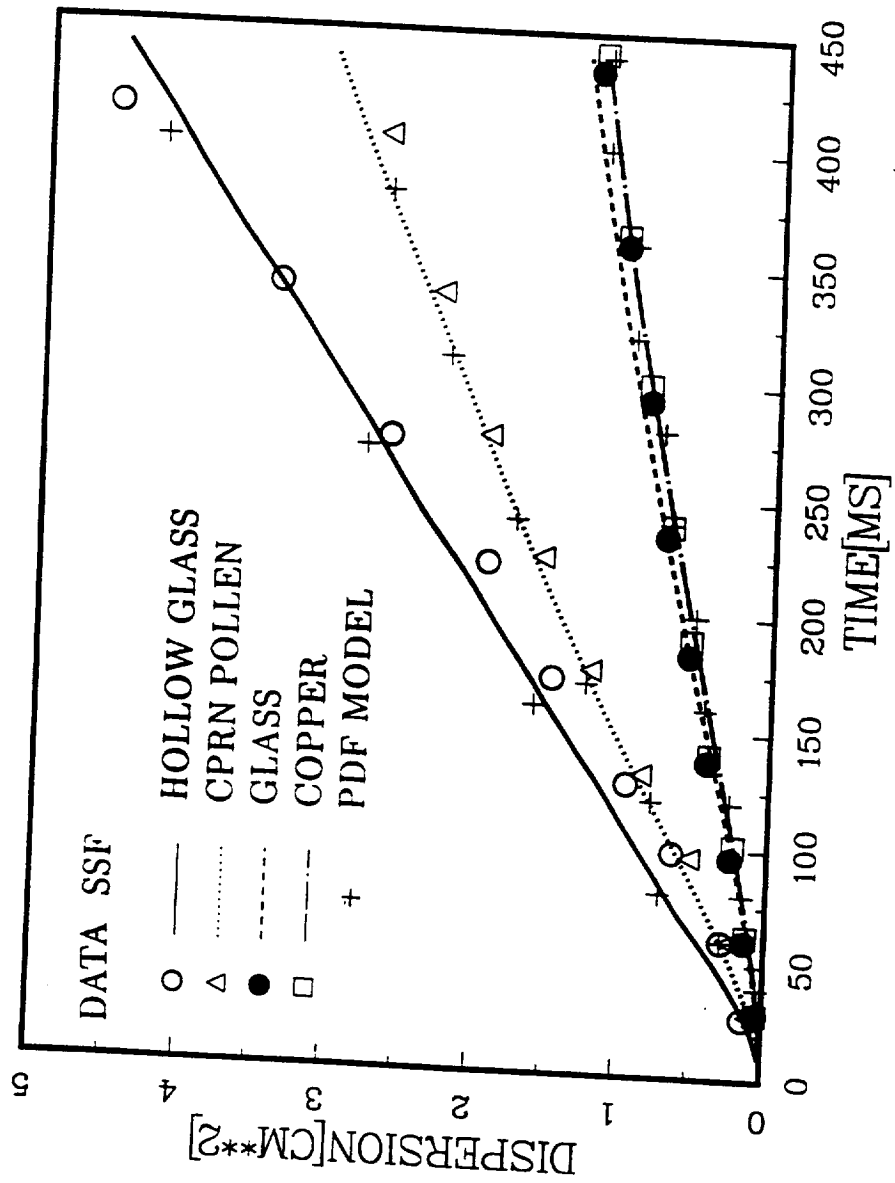

Figure IV.1: Particle dispersion of a nearly-homogeneous flow for SSF model (5000 particles) and PDF model.

Table IV.1: Particle Parameters

Parameter	Hollow glass	Solid glass	Corn	Copper
Diameter (μm)	46.5	87.0	87.0	46.5
Density (g/cc)	0.26	2.5	1.0	8.9

controls the interaction times . For the medium particle (solid glass), the particle inertia or the transit time controls the interaction times. But for the heavy particles (corn pollen and copper), the crossing trajectory effect dominates this dispersion.

In this experiment, the concentration of particle is so dilute that only one-way coupling is of main concern. In the calculation, the experimentally determined fluid turbulence kinetic energy and its dissipation rate are used. The eddy life time $t_e = 3C_\mu \frac{k}{\epsilon}$ was derived in Section (II.3.4) and the eddy length scale $l_e = 1.65 C_\mu^{\frac{3}{4}} \frac{k^{\frac{3}{2}}}{\epsilon}$ was tuned to fit the experimental data. The particle calculations were started at the experimental particle injection point of $x/M = 20$. The particle velocities were assumed equal to the mean fluid velocity of 6.55 m/s and their fluctuating velocities were set to zero. When the particles were injected, each particle interaction time with eddy was randomly assigned within the eddy life time. Otherwise the predicted particle dispersion curve would be oscillatory with the period of eddy life time especially for light particle (hollow glass).

For the delta function SSF computations, 5,000 computational particles were sampled to calculate the resulting mean squared dispersion with respect to time. This computational particle number was chosen to get a smooth dispersion curve with minimum required number.

For the PDF computations, a single parcel in a deterministic trajectory along the centerline was sampled to evaluate the mean squared dispersion representing the variance of the parcel PDF by using the related parameters for each eddy interaction. The calculation of this single particle was started with $x/M = 68.4$, where particle pictures were taken. The mean particle injection velocity was same as the fluid velocity, but its root mean squared (rms) velocity was set to 60% of the gas rms velocity to partially take into account the turbulence effects from x/M=20 where it was injected.

Figure IV.1 shows the comparison of the predicted and measured particle dispersion with respect to time. The particle dispersion is defined as the mean squared displacement y related to the centerline,

$$\overline{Y^2} = \frac{1}{NP} \sum_{n=1}^{NP} y_n^2 \tag{IV.3}$$

The parcel PDF results show good agreement with the SSF results for light, medium, and heavy particles. Both models also show favorable agreement with the experimental data.

These numerical results indicate that the parcel PDF model can accurately and efficiently predict the particle dispersion this nearly-homogeneous turbulent flow.

IV.1.2 Inhomogeneous Turbulent Dispersion

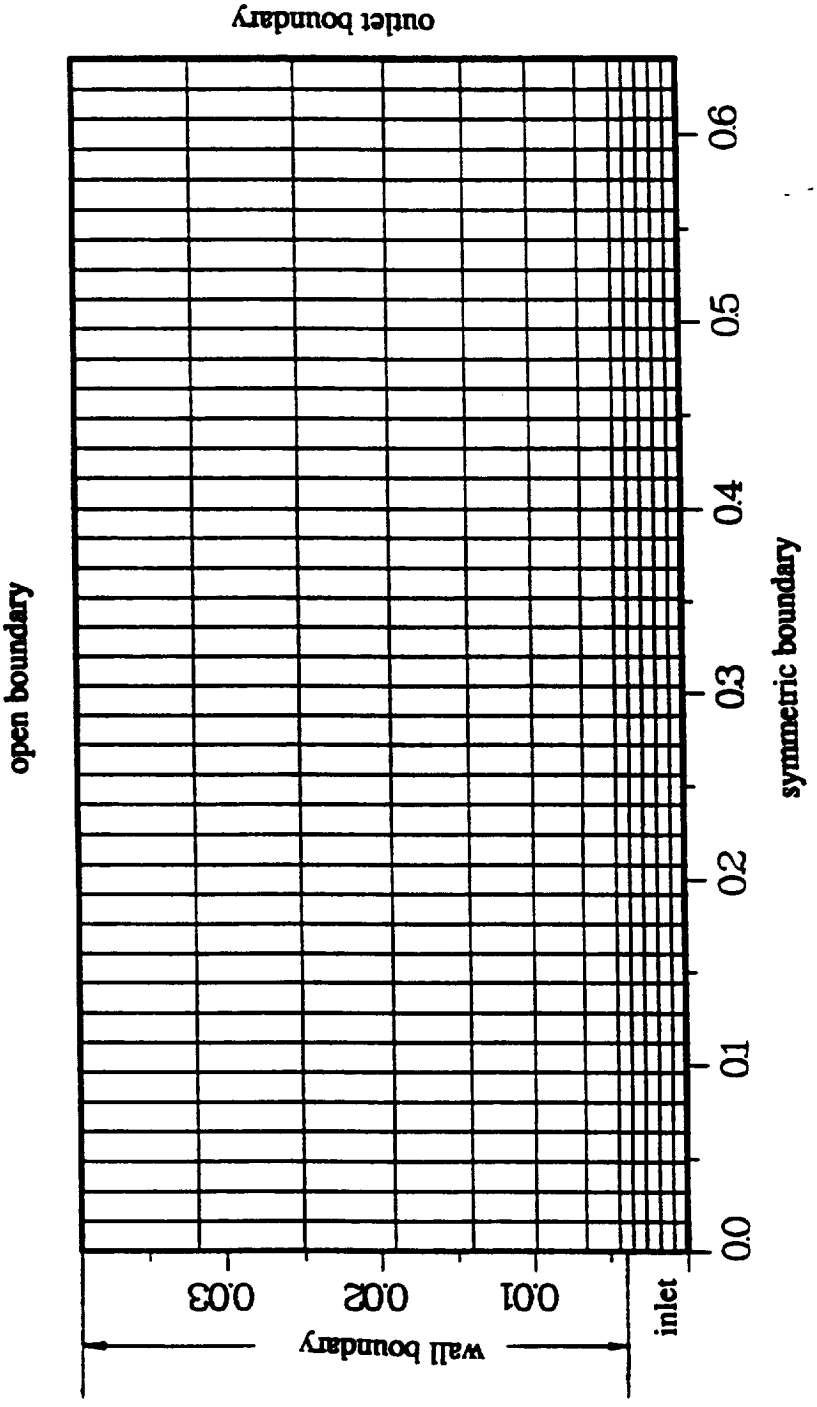

Figure IV.2: Grid system and boundary conditions for round turbulent jet.

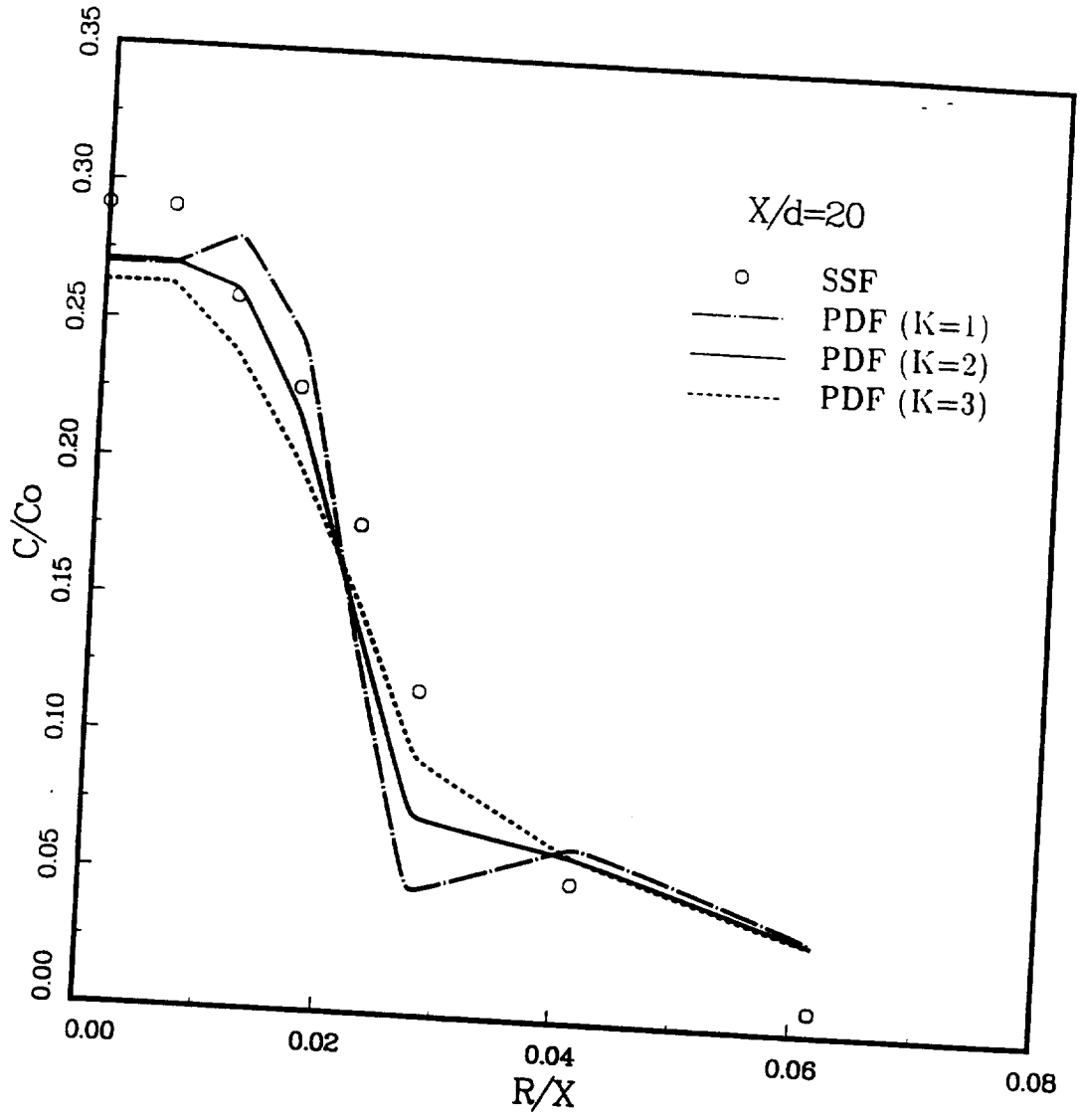

Figure IV.3: Normalized particle concentration distribution of particle laden round jet for SSF (10,000 parcels) and PDF (50 parcels) with various correction factors (x/d=20).

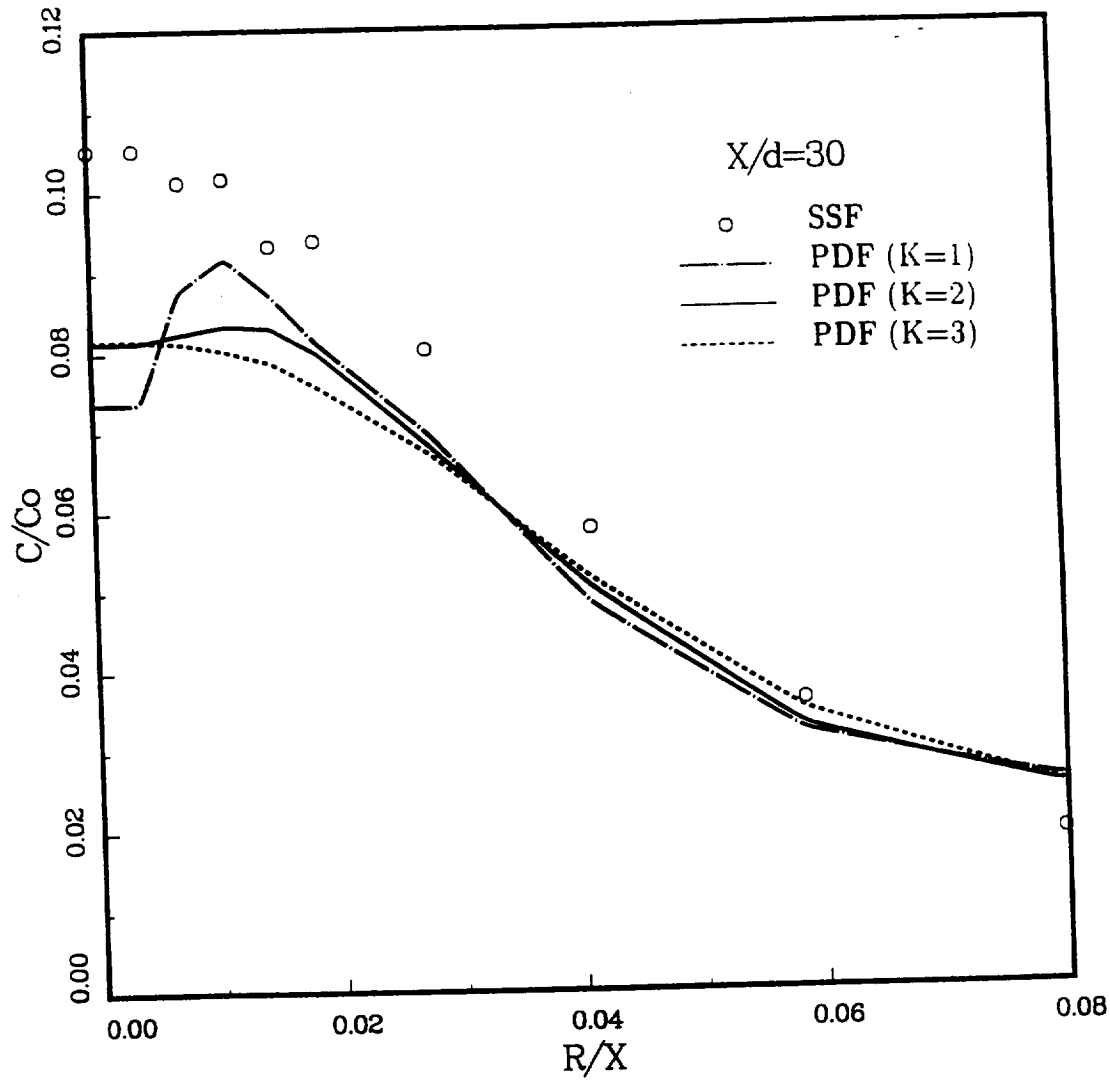

Figure IV.4: Normalized particle concentration distribution of particle laden round jet for SSF (10,000 parcels) and PDF (50 parcels) with various correction factors (x/d=30).

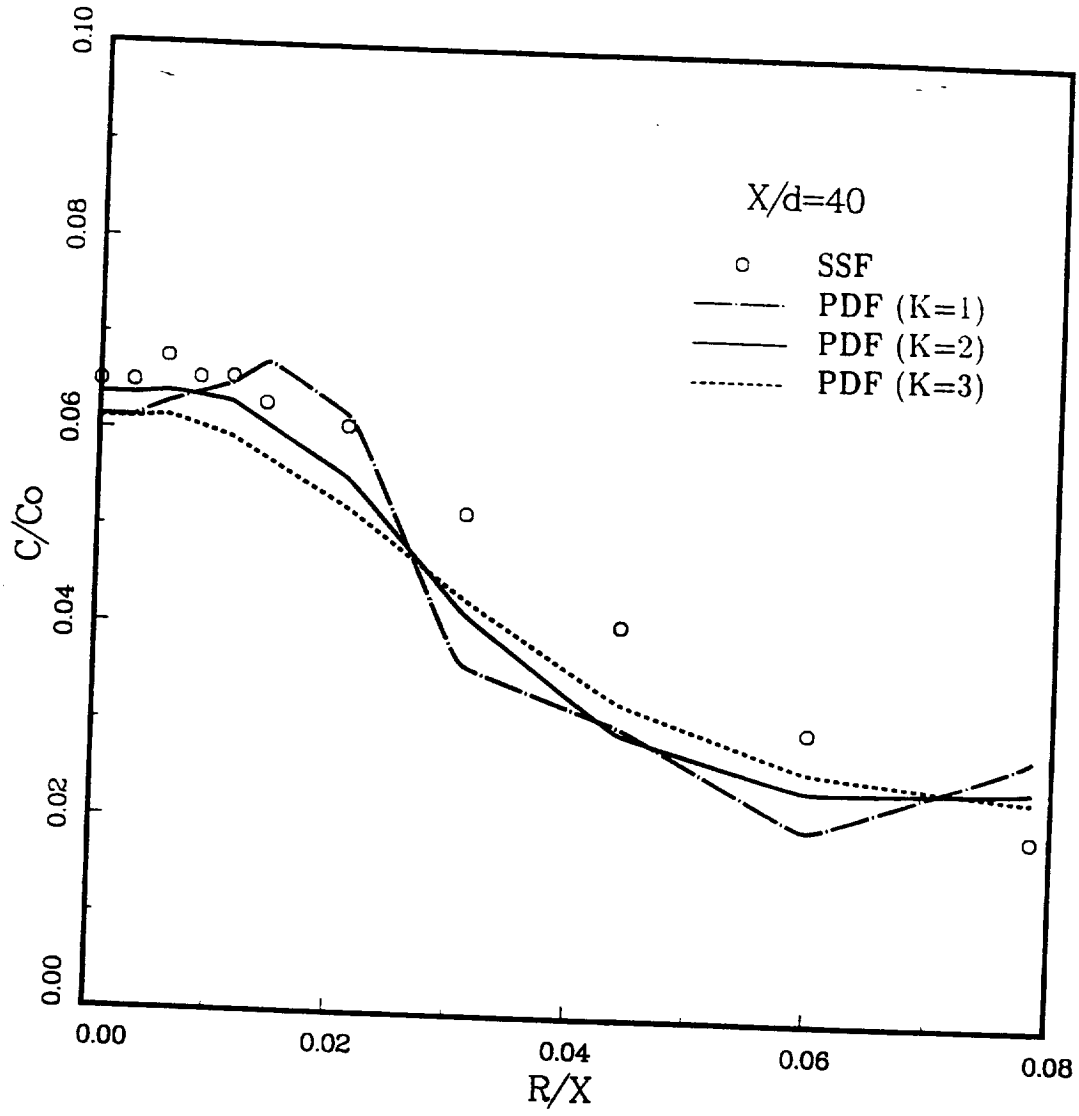

Figure IV.5: Normalized particle concentration distribution of particle laden round jet for SSF (10,000 parcels) and PDF (50 parcels) with various correction factors (x/d=40).

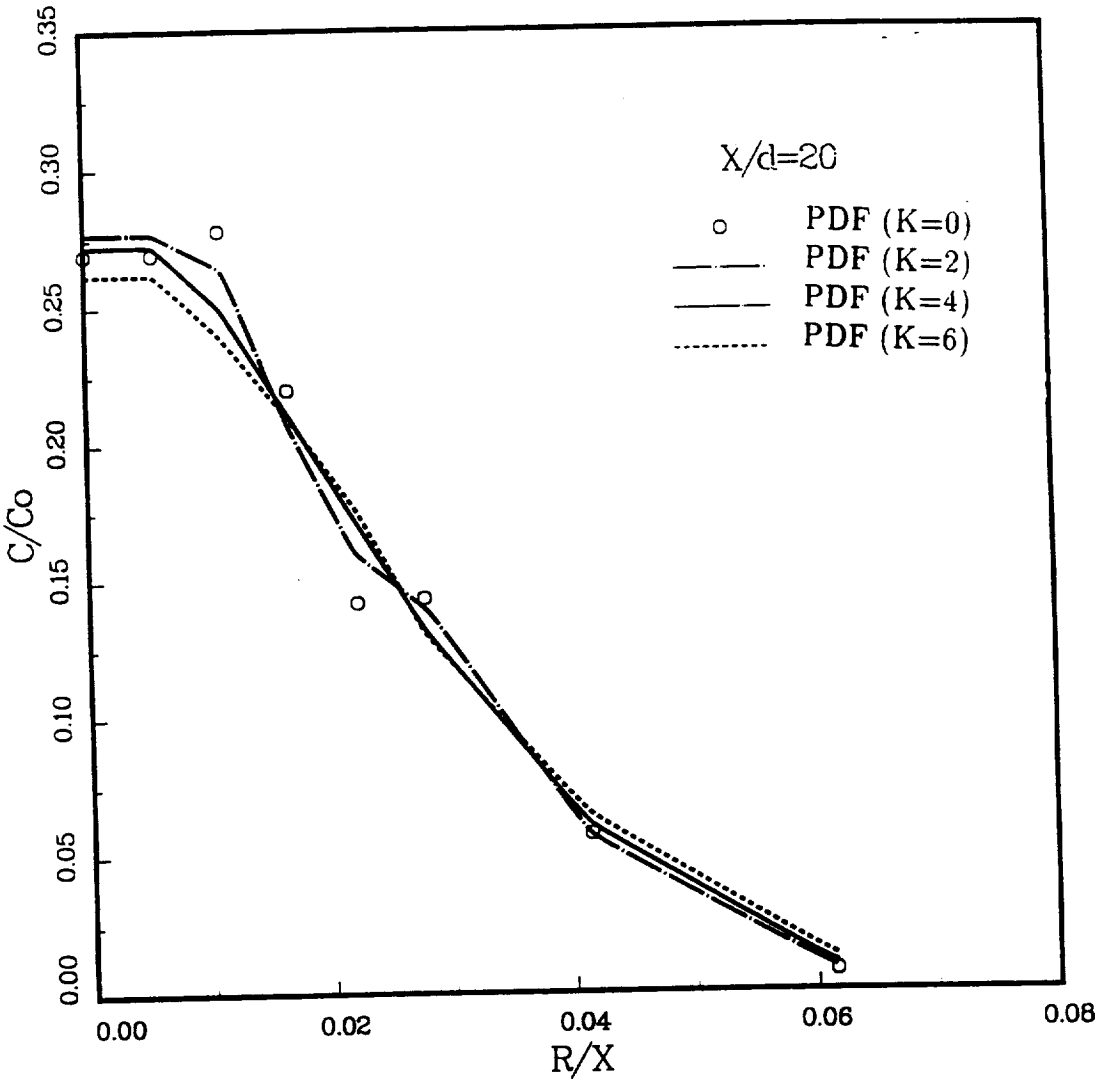

Figure IV.6: Normalized particle concentration distribution of particle laden round jet for PDF (200 parcels) with various correction factors (x/d=20).

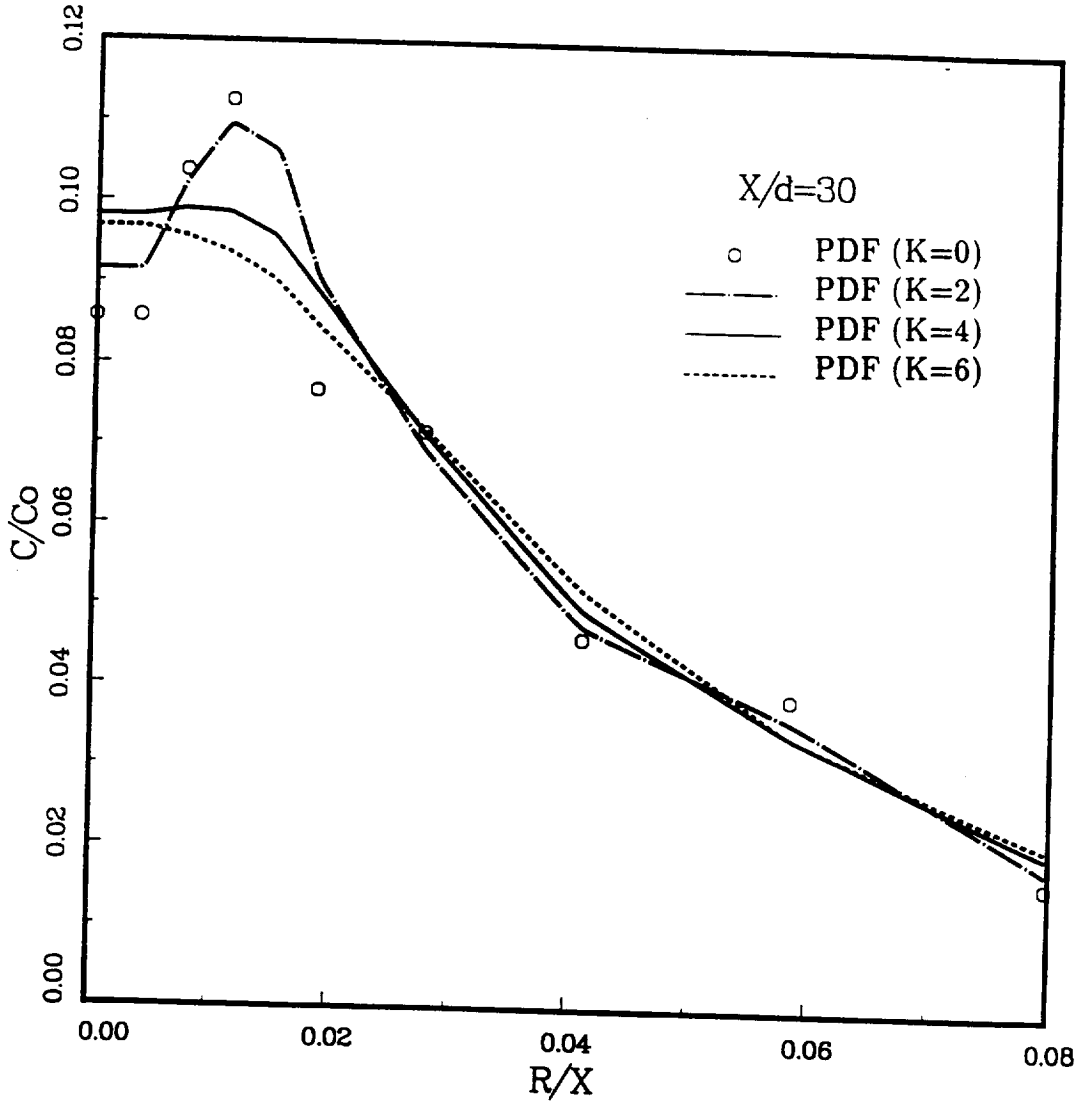

Figure IV.7: Normalized particle concentration distribution of particle laden round jet for PDF (200 parcels) with various correction factors (x/d=30).

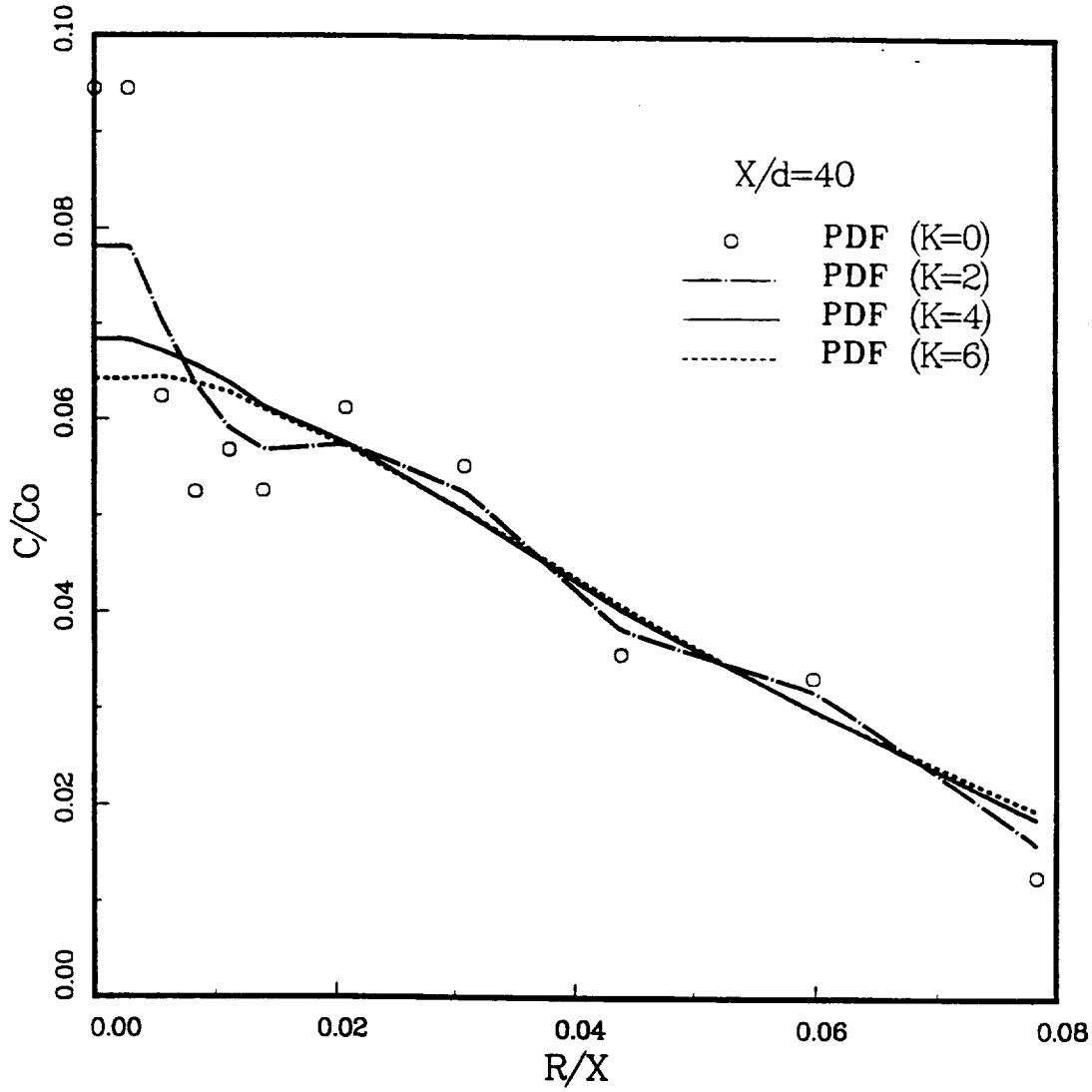

Figure IV.8: Normalized particle concentration distribution of particle laden round jet for PDF (200 parcels) with various correction factors (x/d=40).

The next example problem is the particle laden round jet of Yuu et al. [123] in which the turbulence is inherently inhomogeneous. The air jet is directed upward against the gravitational force. The nozzle diameter is 8 mm with a mean exit velocity of 20 m/s. Particles are injected with air velocity from the nozzle. The particle concentrations at the nozzle exit were measured at the centerline in the potential core and were between 0.8 and 4 g/m^3. The loading effects can be neglected, hence only one-way coupling needs to calculate. The turbulent gas-phase transport properties are provided by using the $k-\epsilon$ model. A 41×31 grid system with uniform grids in axial direction and clustered grids about the centerline is used in the calculation. Figure IV.2 shows the vicinity grid distribution in the centerline region and boundary conditions. The injected turbulent kinetic energy 1.2, which corresponding to 0.3% U^2, and its dissipation rate 20,000 are used to keep a very low eddy viscosity. Uniform profiles of velocity, turbulent kinetic energy and its dissipation rate are assumed for inlet boundary conditions. Numerical experimental results show that this choice gives a good prediction of the potential core length of the air jet when compared with the experimental data. For particle tracking calculation, a constant time-step $10\mu s$ is used.

The particle concentration profiles have been extensively examined by Shuen [107] using the SSF model. Also, Litchford and Jeng [75] have tested their DDWT and SDWT models with similar flow properties and different particle sizes, and the SDWT model is suggested to take into account the flow property variation in radial direction. The present study is to incorporated the parcel PDF (or SDWT) model and compare with the SSF model in terms of accuracy and efficiency in the statistical model, and no intention is made to compare with the experimental data. In the

following calculation, the particle size is 20 μm and density is 2.0 g/cm^3. Particle number concentration profiles are obtained with the particle number located in the cell divided by its volume and normalized by the total particle number in the cross section.

Figures IV.3, IV.4, IV.5, IV.6, IV.7 and IV.8 show the particle concentration profiles of the delta function SSF model and the SDWT model for 50 and 200 computational parcels, at various levels of the correction factor, and at several axial locations. 10,000 particles are sampled for the delta function SSF computations. Using the 10,000 particles in the SSF model, there is still evidence of slight undersampling. However the distribution is relatively smooth and is taken here as a good approximation to the theoretical profile. The results of the SDWT model with 50 parcels shown in Figures IV.3,IV.4 and IV.5 are very sensitive to the level of the correction factor, especially for upstream regions due to undersampling. By increasing the correction factor, K in equation (II.89), the uncertainty level in the mean increases the dispersion and smoothes the profile considerably. In Figures IV.6, IV.7 and IV.8 the zero correction factor case(K=0) corresponds to the delta function SSF case using 200 computational parcels. The computed profile of the SSF model using 200 parcel samples is very irregular and shows oscillatory distribution.

The 200 parcel case of parcel PDF model shown in Figures IV.9, IV.10 and IV.11 is less sensitive to the correction factor since there is less uncertainty in the mean because of increased sampling. In Figures IV.9, IV.10 and IV.11, the PDF results with 200 parcels and K=4 show favorable agreement with the delta function SSF with 10,000 computational particles. In terms of the CRAY X/MP-24 CPU time, the parcel PDF (SDWT) solutions with 200 parcels requires about 36 seconds while

the SSF solutions with 10,000 parcels needs about 1,375 seconds. These numerical results clearly indicate that the parcel PDF model has the capability of accurately representing dispersion in inhomogeneous turbulent flows with improved efficiency over the delta function SSF model.

In the calculation of Litchford and Jeng [75], with only 50 parcels the PDF model produces smooth and accurate distributions comparing 200 parcels required in the present calculation. This discrepancy should be attributed to the different methods for calculating the particle concentration and different grid size used for accounting the particle number in the cell. In Litchford and Jeng's calculation, they used PSIC and particle concentration was obtained by calculating the particle transition time crossing the cell boundaries, which usually gives more accurate results but needs more computation time and is not convenient for arbitrary grid system. In the present method, only the particles which located in the cell are taken into the concentration calculation.

IV.2 Non-Evaporating Solid-Cone Spray

IV.2.1 Measurements of Hiroyasu and Kadota

The solid-cone spray measurements of Hiroyasu and Kadota [43] were used to validate the present numerical dense spray model which includes collision, coalescence, and breakup models described in Chapter II. Liquid fuel is injected through a single hole nozzle into constant pressure, room-temperature nitrogen. Spray tip penetration and drop sizes were measured from photographs of the backlighted spray. The test conditions are given in Table IV.2, and the SMD is measured for the spray cross-section 65 mm downstream of the nozzle. The nozzle diameter was 0.3 mm

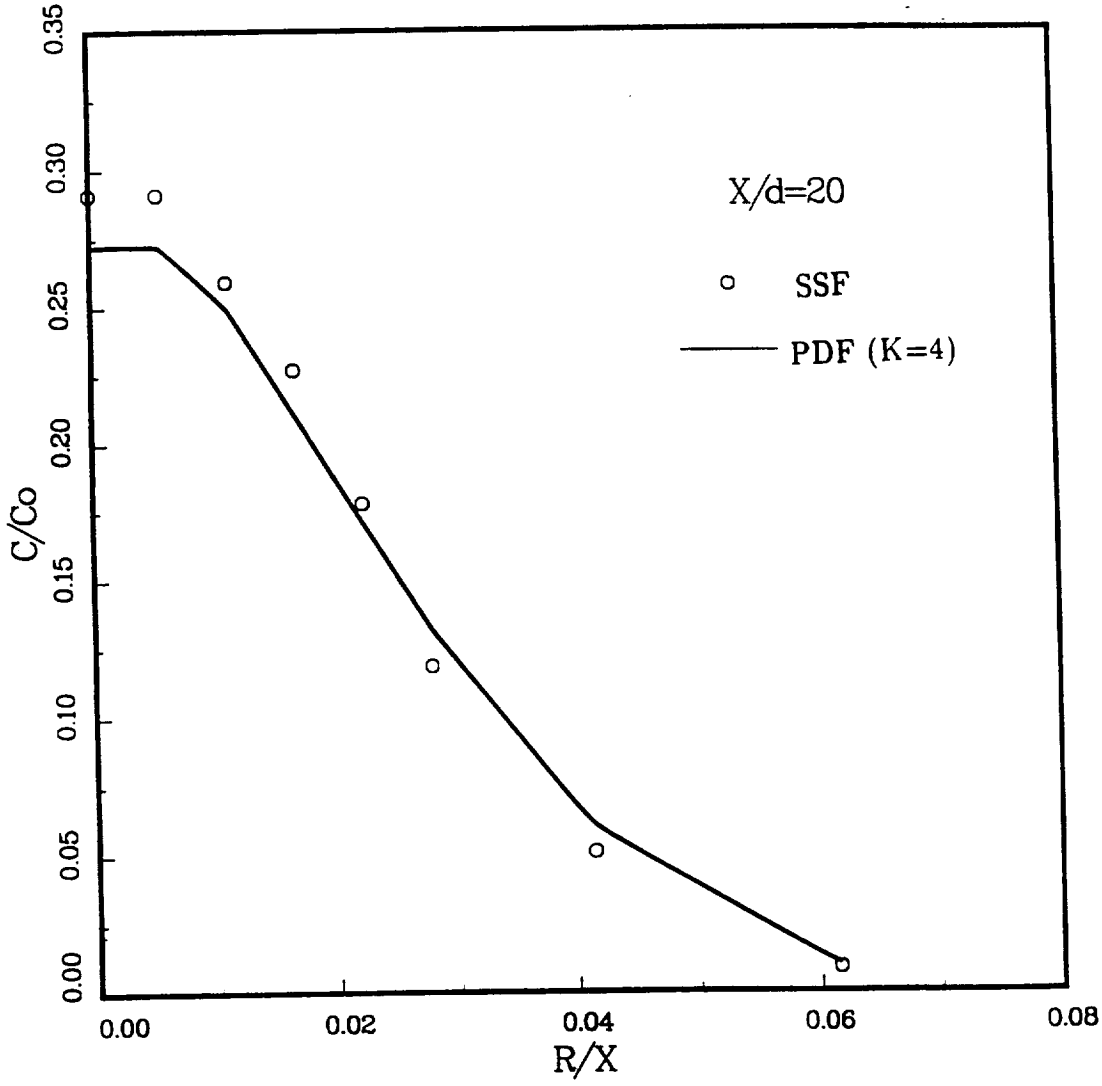

Figure IV.9: Normalized particle concentration distribution of particle laden round jet for SSF (10,000 parcels) and PDF (200 parcels) (x/d=20).

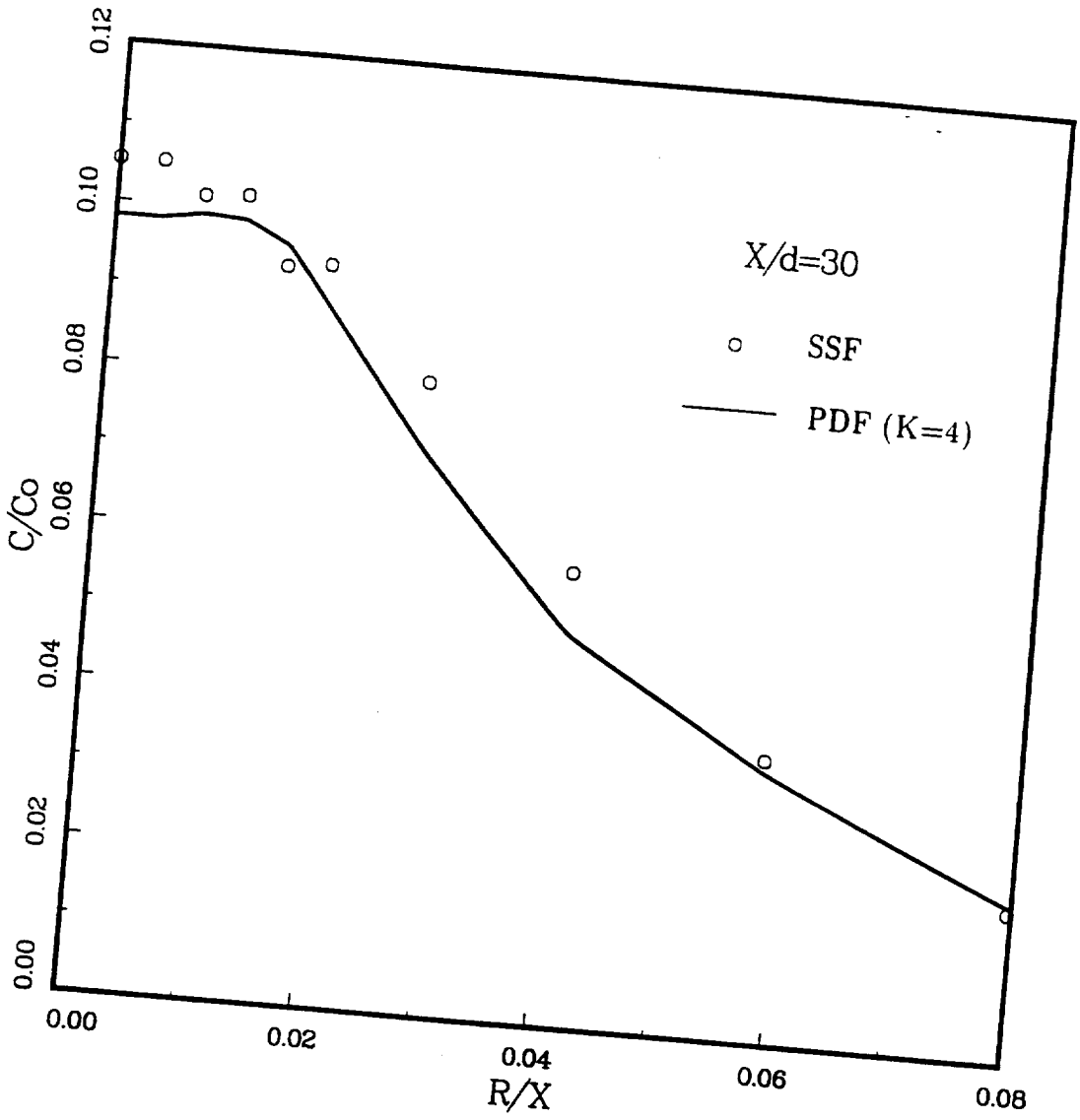

Figure IV.10: Normalized particle concentration distribution of particle laden round jet for SSF (10,000 parcels) and PDF (200 parcels) (x/d=30).

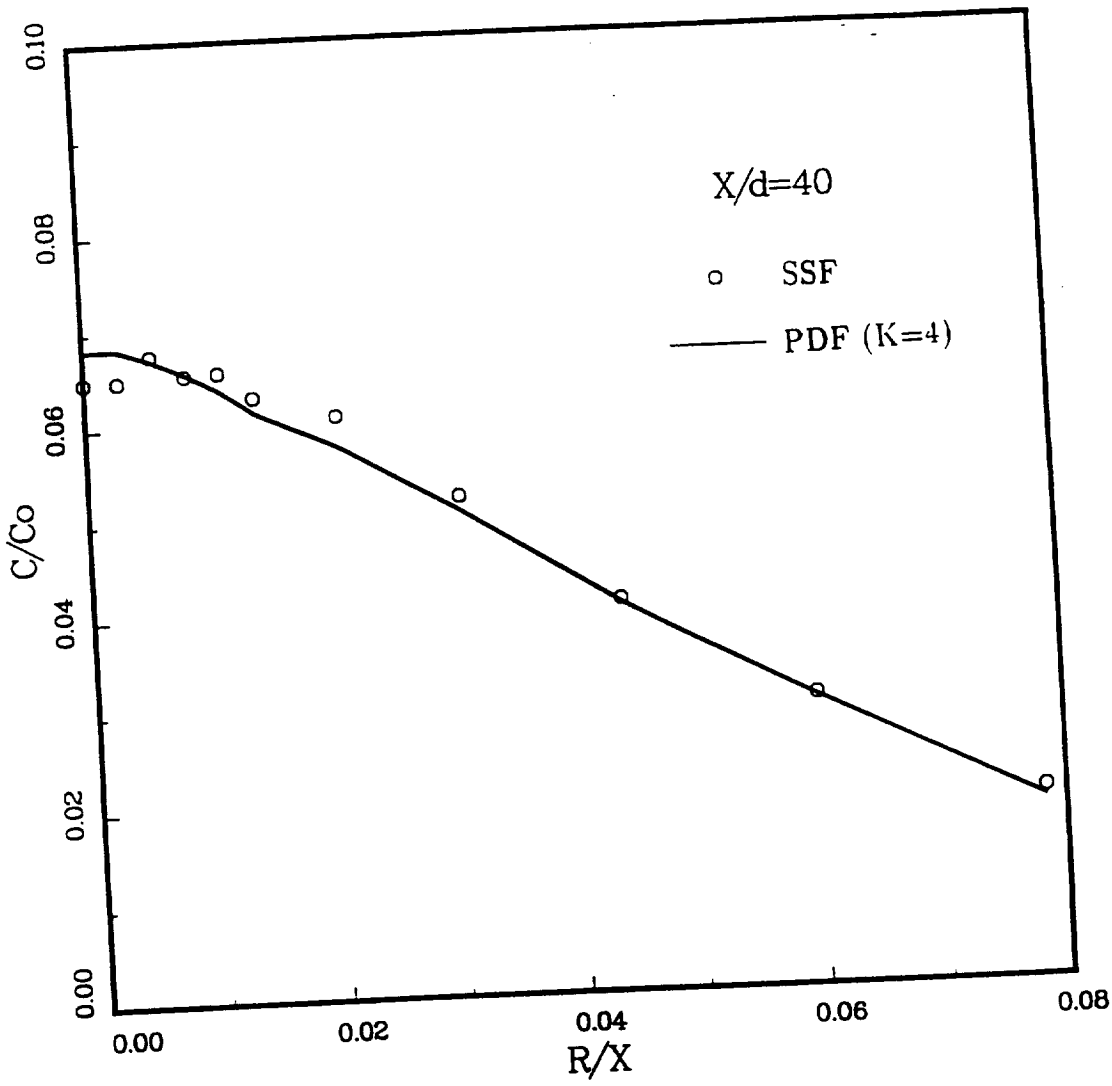

Figure IV.11: Normalized particle concentration distribution of particle laden round jet for SSF (10,000 parcels) and PDF (200 parcels) (x/d=40).

Table IV.2: Test Conditions for the Measurement of Hiroyasu and Kadota

Nozzle diameter: 300 μm Injection pressure: 9.9 MPa

Liquid: diesel fuel Density: 840 kg/m^3

Viscosity: $3.8 \times 10^{-4} N \cdot s/m^2$ Surface tension: 0.0232N/m

Ambient gas: nitrogen Temperature: $25°C$

Case	Pgas (MPa)	ρ_{gas} (kg/m^3)	Vinj (m/s)	Minj (kg/s)	SMD (μm)
1	1.1	12.36	115.80	0.00688	42.4
2	3.0	33.70	102.54	0.00609	49.0
3	5.0	56.17	86.41	0.00513	58.8

and the present computations used tetradecane for the liquid fuel (the experiments used a diesel fuel with physical properties close to tetradecane).

A computational domain of 20 mm in radius and 120 mm in length was discretized by a 25 radial and 45 axial grids. The mesh spacing was nonuniform with refinement on the centerline and close to the injector. The smallest cell is 0.5 mm radially and 1.5 mm axially. The grid system and boundary conditions are shown on Figure IV.12. The time-step sizes used for three test cases are 10, 18 and 18 μs respectively

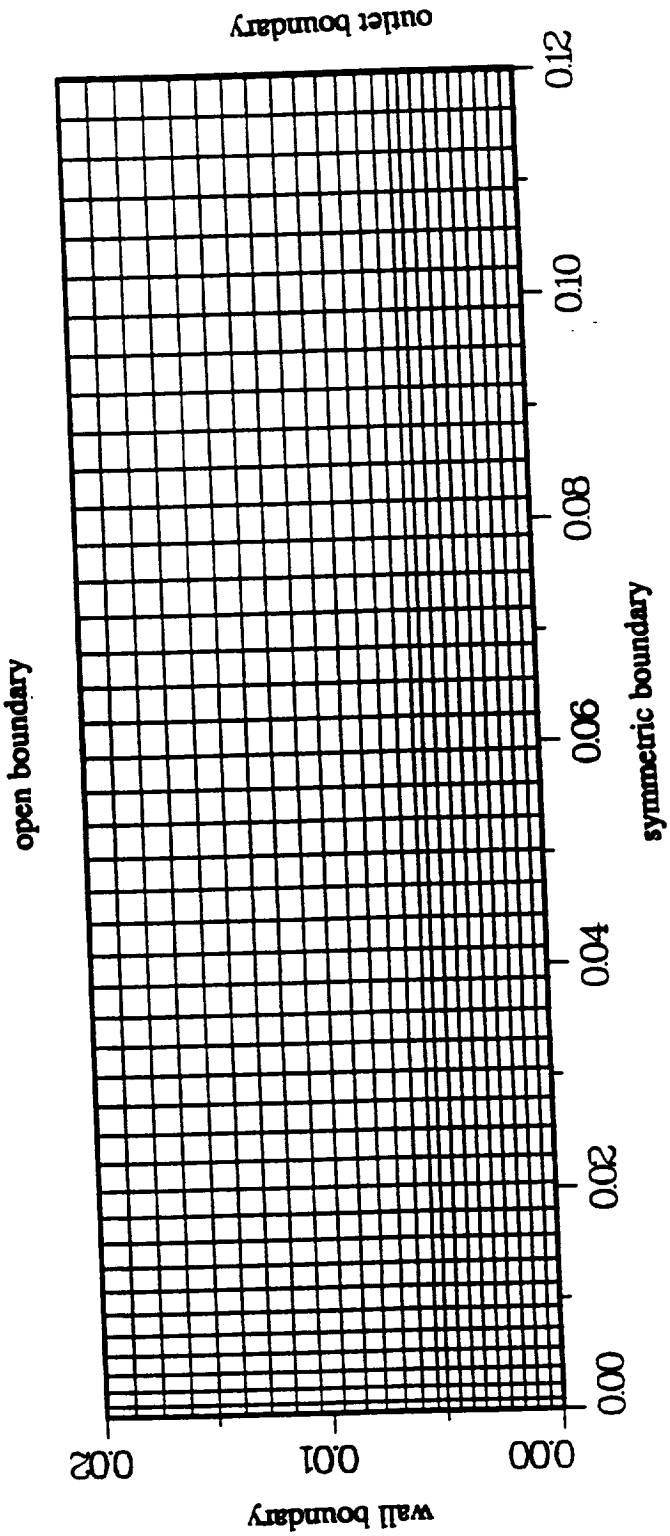

Figure IV.12: Grid system and boundary conditions for solid-cone spray.

and 250 time steps are used for all of the three cases. The number of computational parcels at the end of calculations was between 1000 and 3000, which were varied with the back pressure. The present numerical results did not change appreciably when this parcel number was varied. The initial turbulent quantities were assumed as the small values ($k = 1 \times 10^{-3} m^2/s^2, \epsilon = 4 \times 10^{-4} m^2/s^3$). The numerical results were insensitive to these initial values. The typical CPU time required on CRAY X-MP/24 using both breakup models is listed on Table IV.3.

Table IV.3: CPU Time Requirement for the Hiroyasu's Case

	TAB Model		Reitz's Model	
Case	Parcel	CPU Time (s)	Parcel	CPU Time (s)
1	1130	114.6	1854	207.0
2	1181	120.4	1038	150.4
3	1248	123.4	1676	229.0

Figures IV.13, IV.14 and IV.15 show the spray parcel distributions for three cases with the TAB breakup model [89] and Figures IV.16, IV.17 and IV.18 with Reitz's model [95]. These plots indicate that the spray tip penetration and the core length decrease with the increase of the gas density. The predicted core lengths ($20mm$ for P=1.1 MPa, $12mm$ for P=3.0 MPa, $10mm$ for P=5.0 MPa) based on Reitz's model

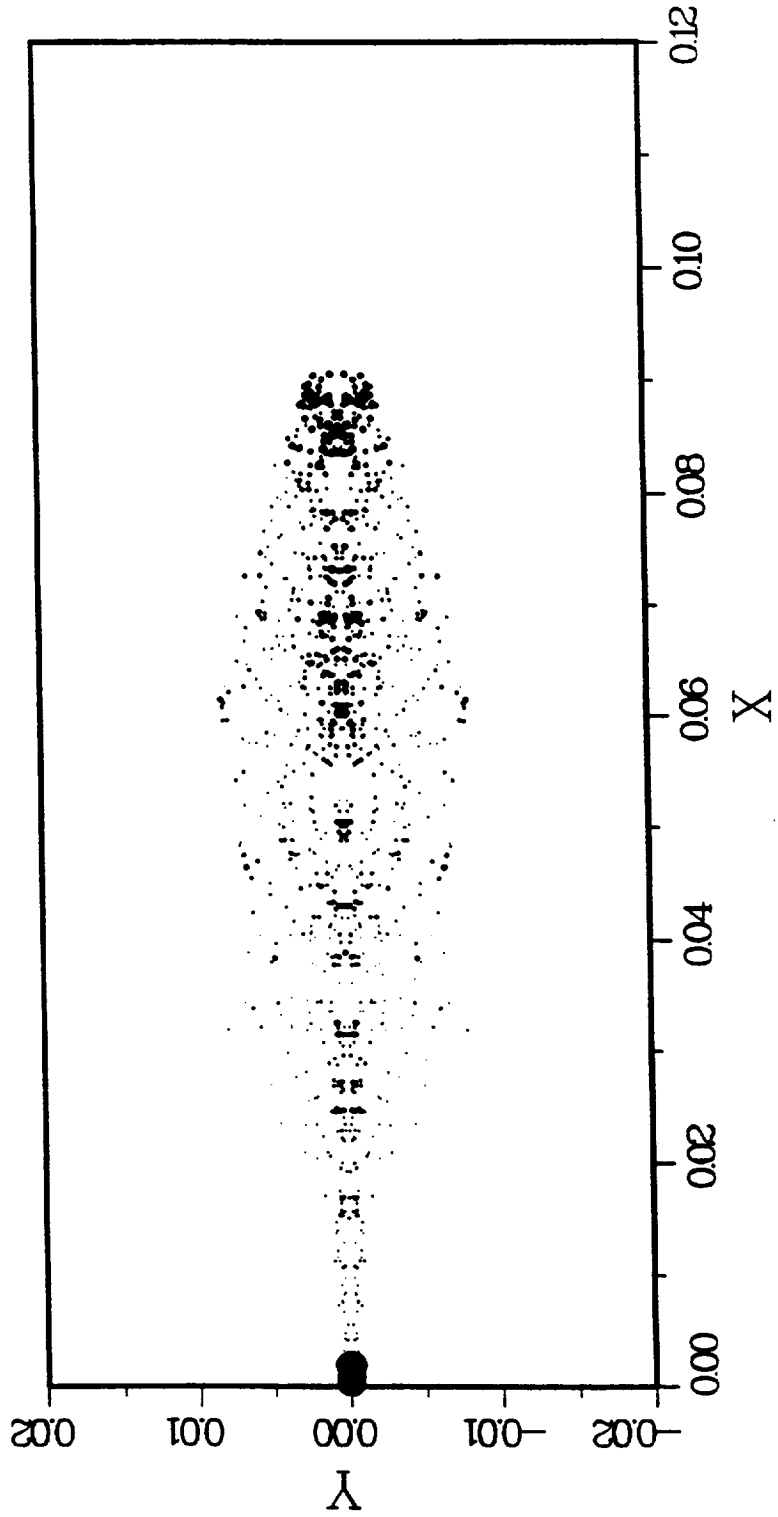

Figure IV.13: Spray parcel distribution in a solid-cone spray (Case 1, Time=2.5ms, TAB model).

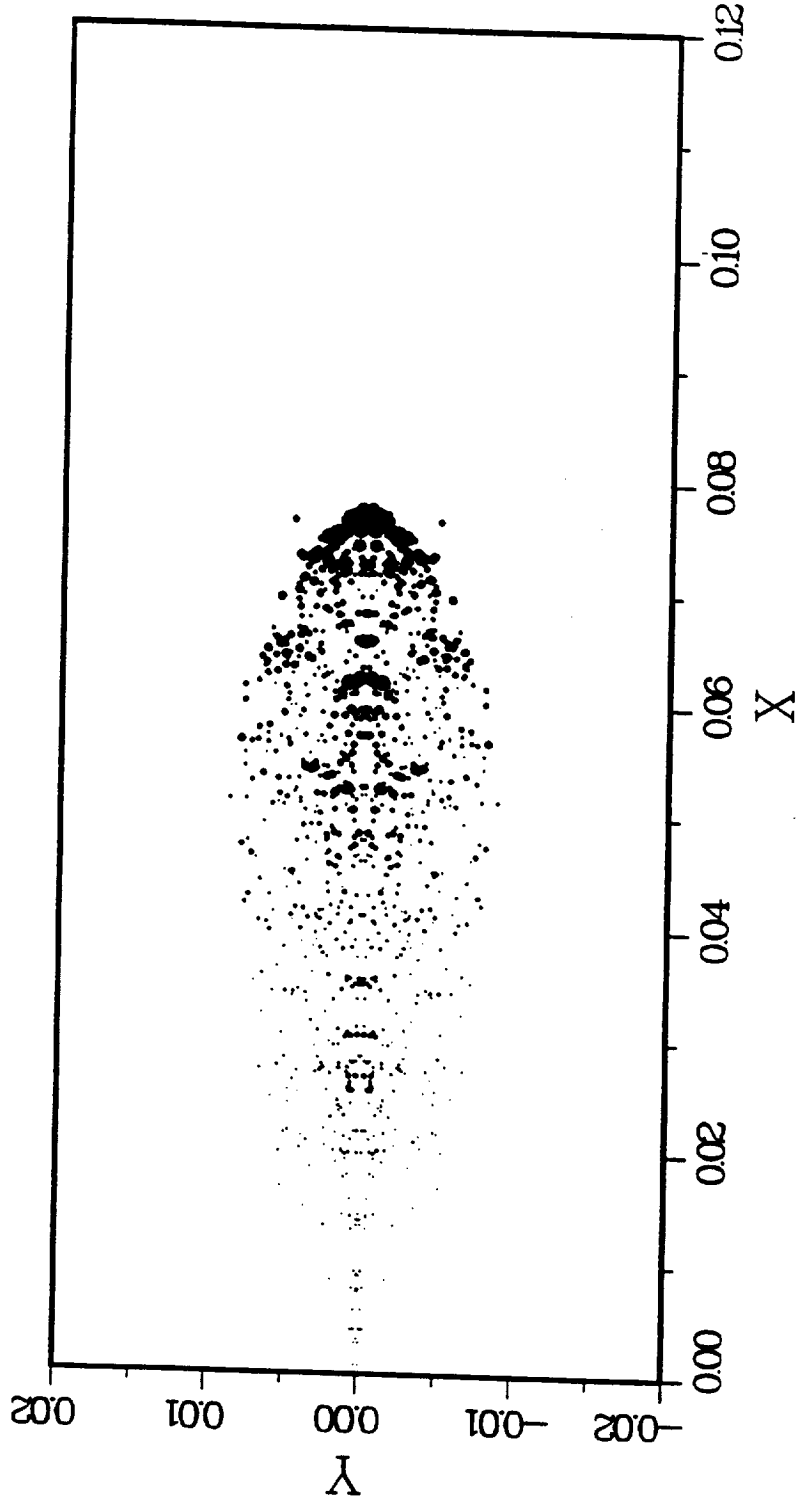

Figure IV.14: Spray parcel distribution in a solid-cone spray (Case 2, Time=4.5ms, TAB model).

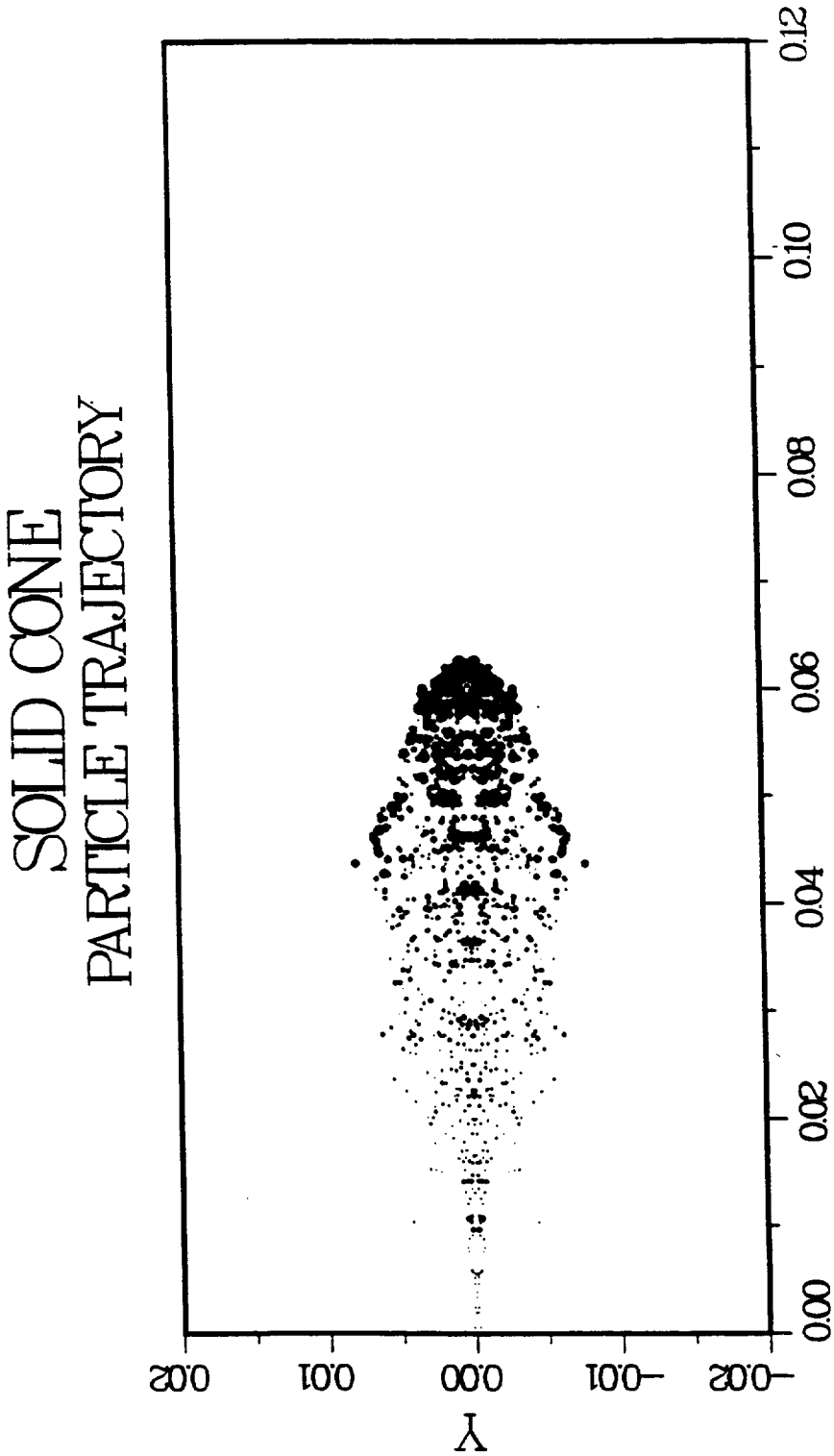

Figure IV.15: Spray parcel distribution in a solid-cone spray (Case 3, Time=4.5ms, TAB model).

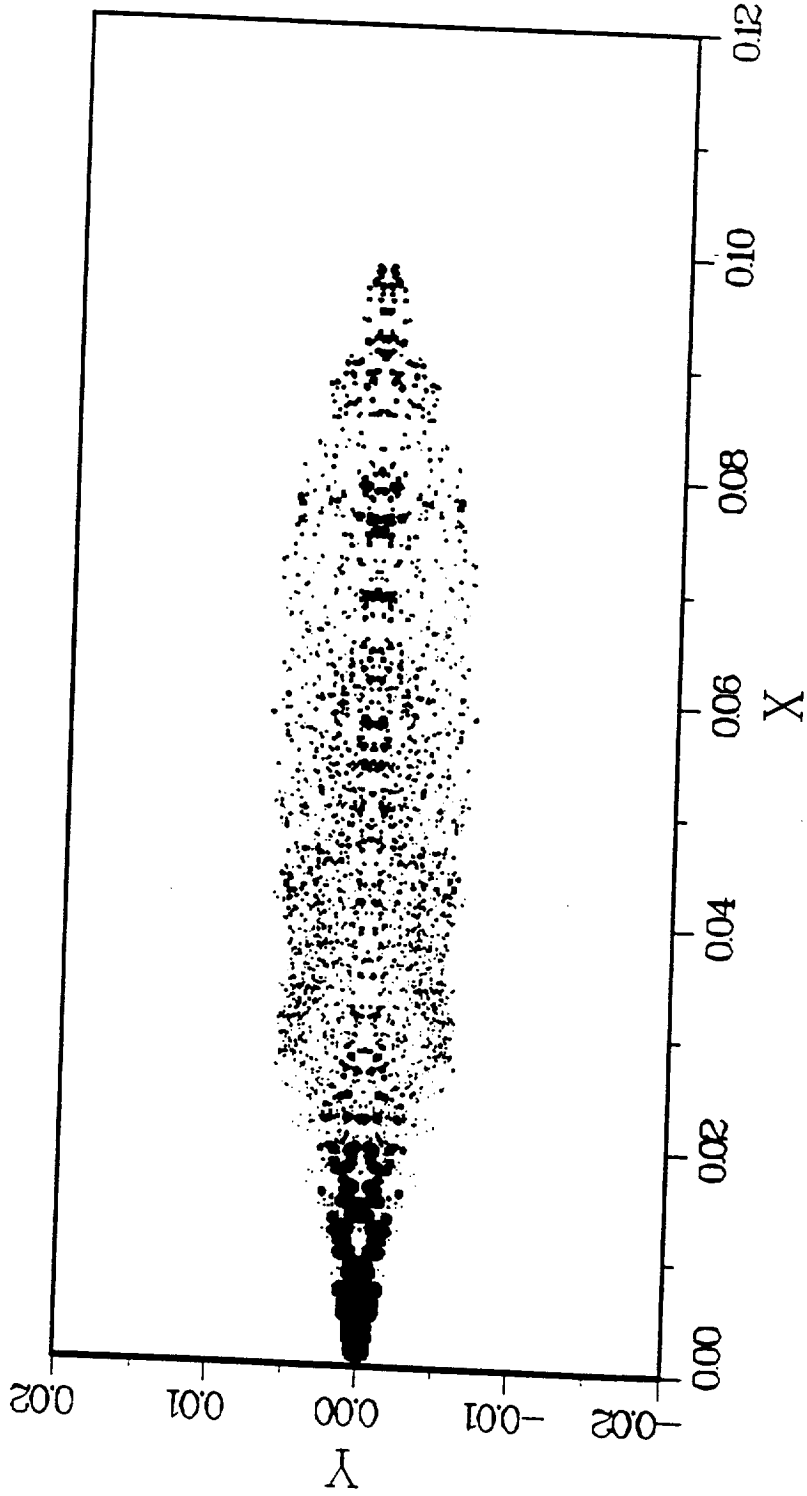

Figure IV.16: Spray parcel distribution in a solid-cone spray (Case 1, Time=2.5ms, Reitz's model).

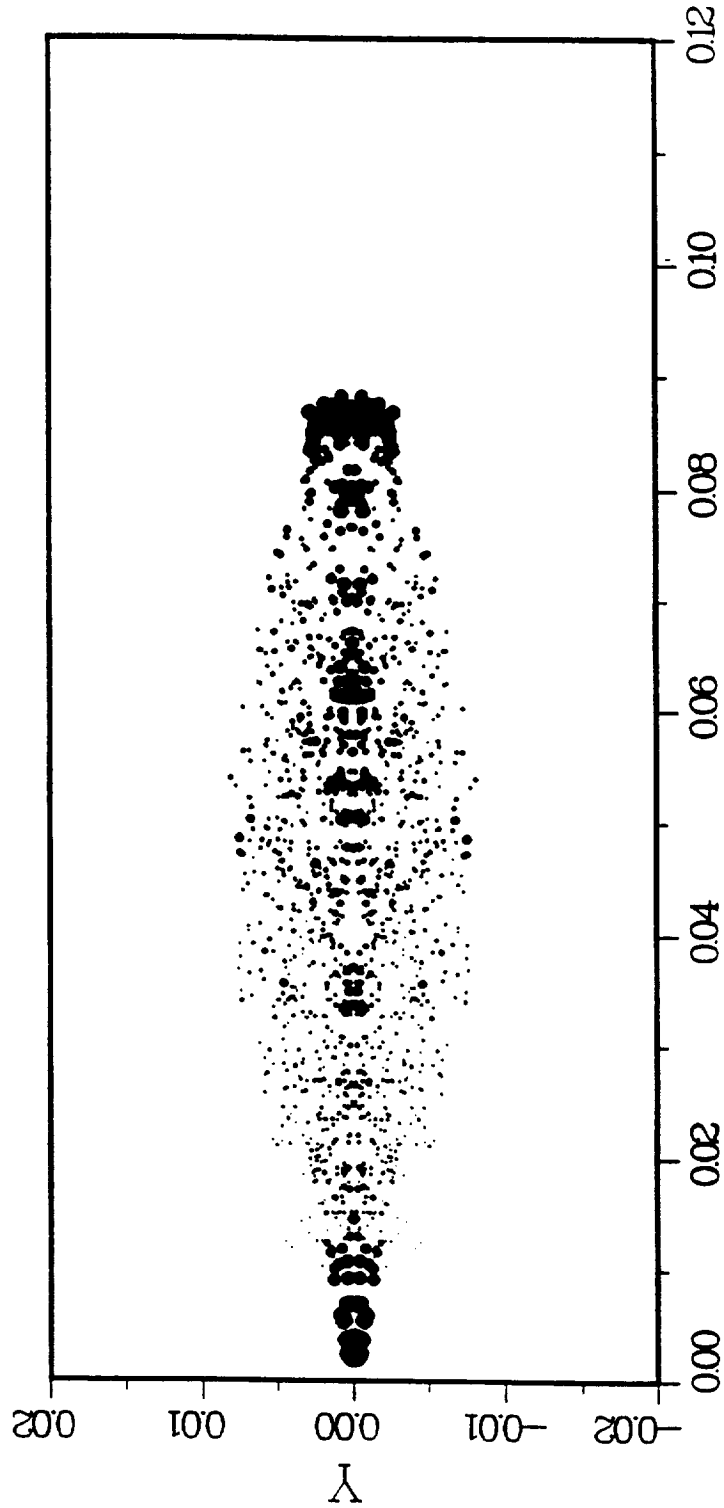

Figure IV.17: Spray parcel distribution in a solid-cone spray (Case 2, Time=4.5ms, Reitz's model).

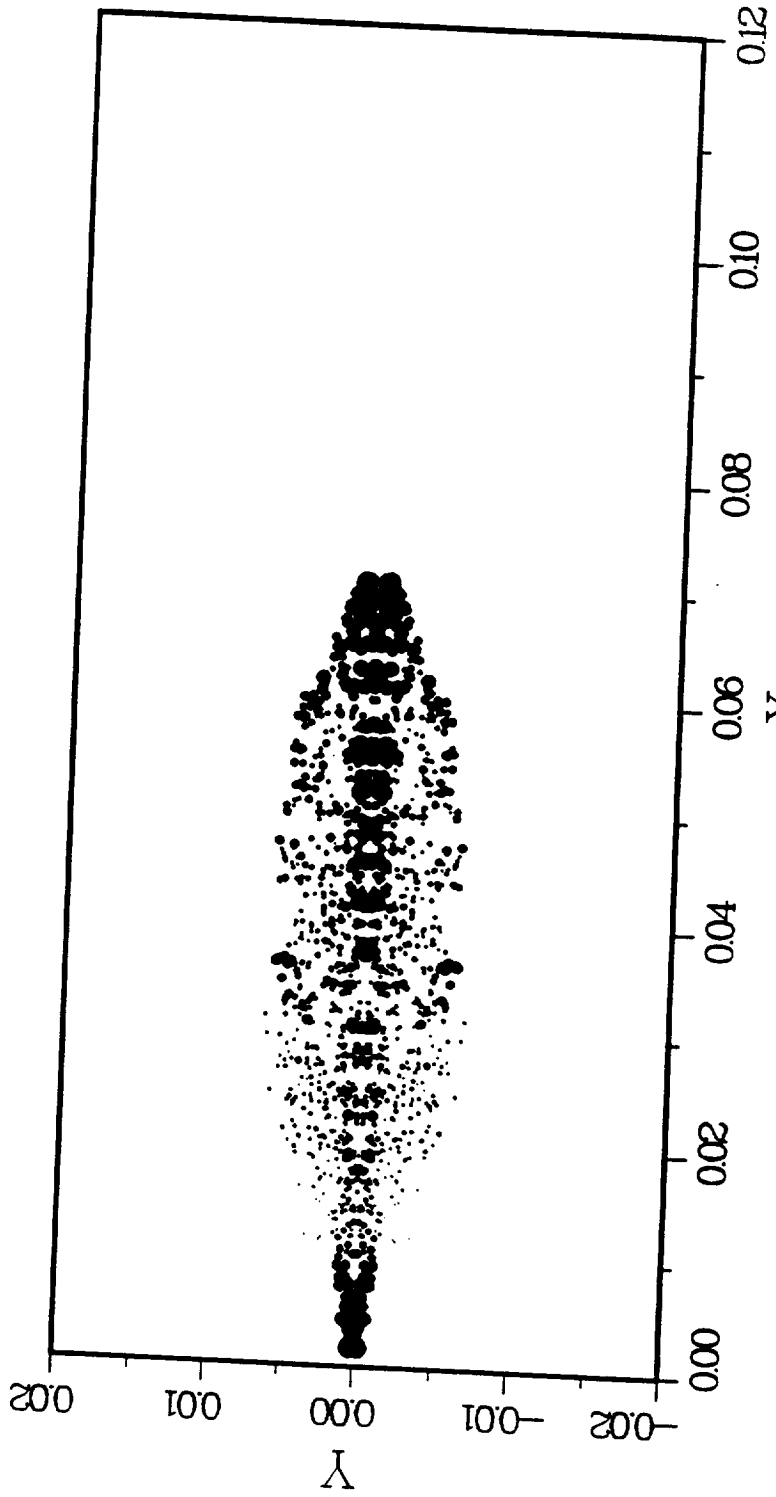

Figure IV.18: Spray parcel distribution in a solid-cone spray (Case 3, Time=4.5ms, Reitz's model).

have a reasonable agreement with the jet length correlation suggested by Arai et al.[6], but the TAB model predicts much shorter intact core lengths. These results indicate that the Reitz's wave instability model is capable of predicting the intact core length with reasonable accuracy.

Figures IV.19 and IV.20 show the predicted and measured spray tip penetration for two breakup models. The calculated penetrations for two breakup models show reasonably good agreement with the measurement. Compared to the TAB model, the Reitz's model slightly overpredicts the penetration length for three cases. However, the discrepancies in the penetration length could be partially attributed to the imprecise definition of the spray tip. In the present computations, the spray tip was defined to be the location of the leading spray drop parcel. It is necessary to note that a far-field spray penetration is not a sensitive indicator of model performance. Previous studies [31, 21] indicated that a far-field spray penetration is mostly influenced by the turbulence diffusivity. However, a near-field spray penetration could be more sensitive to the physical submodels such as breakup and collision.

Figures IV.21 and IV.22 show the variation of SMD for two breakup models. The three data at 65 mm correspond to the measurements. The computed drop sizes are time-averaged over the spray cross-section at each axial location. At the nozzle exit, the drop diameter is equal to the nozzle diameter, 0.3 mm. The overall trend of the SMD distribution is similarly predicted by the two models. Generally, these curves can be broken into two sections. Close to the injector, the drop size decreases rapidly due to drop breakup. Further downstream, the drop size increases gradually due to drop coalescence. In the lower pressure case(1.1 MPa), the drop size remains relatively uniform after initial breakup region and then increases slightly in

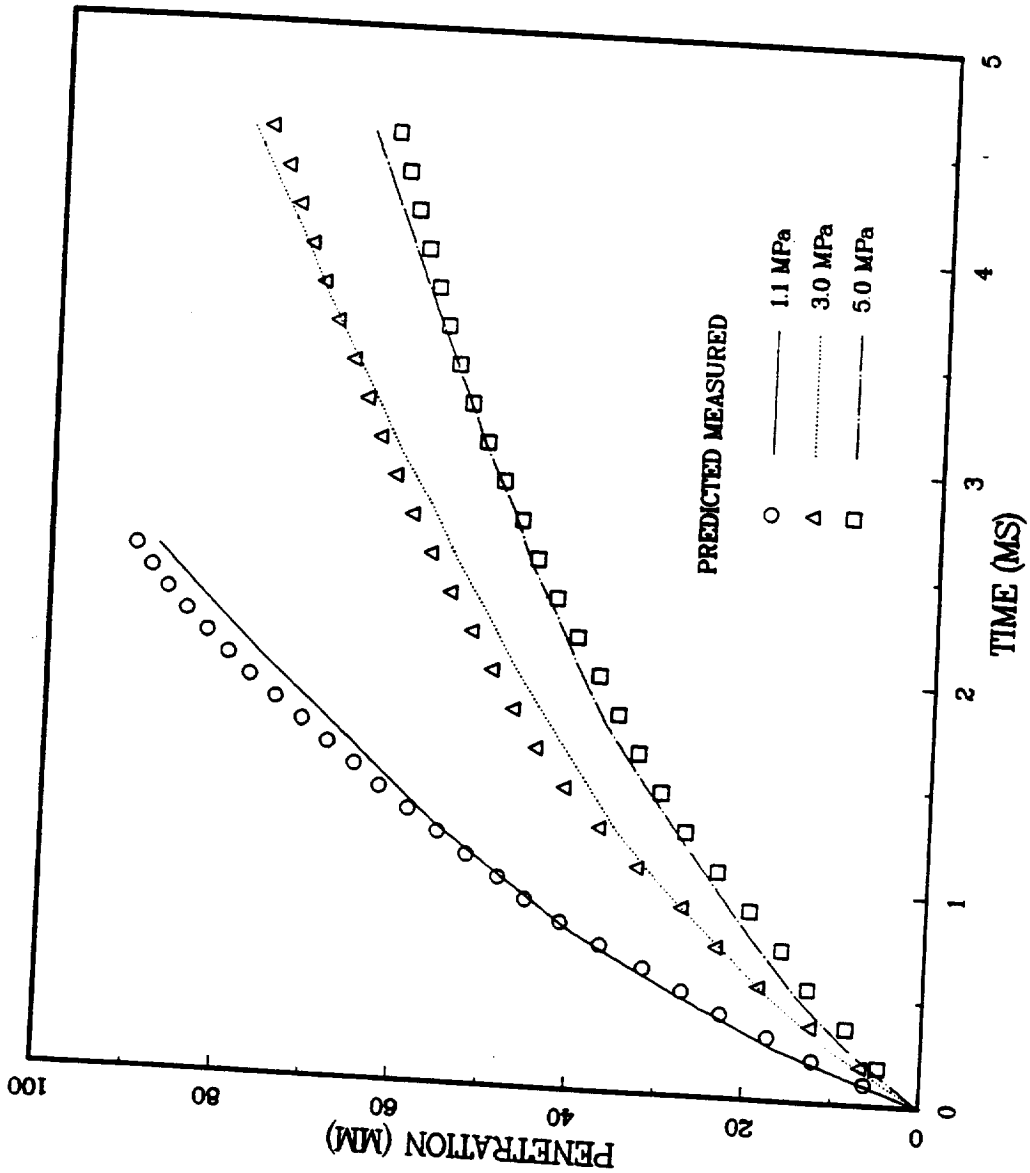

Figure IV.19: Spray tip penetration versus time in a solid-cone spray (TAB model).

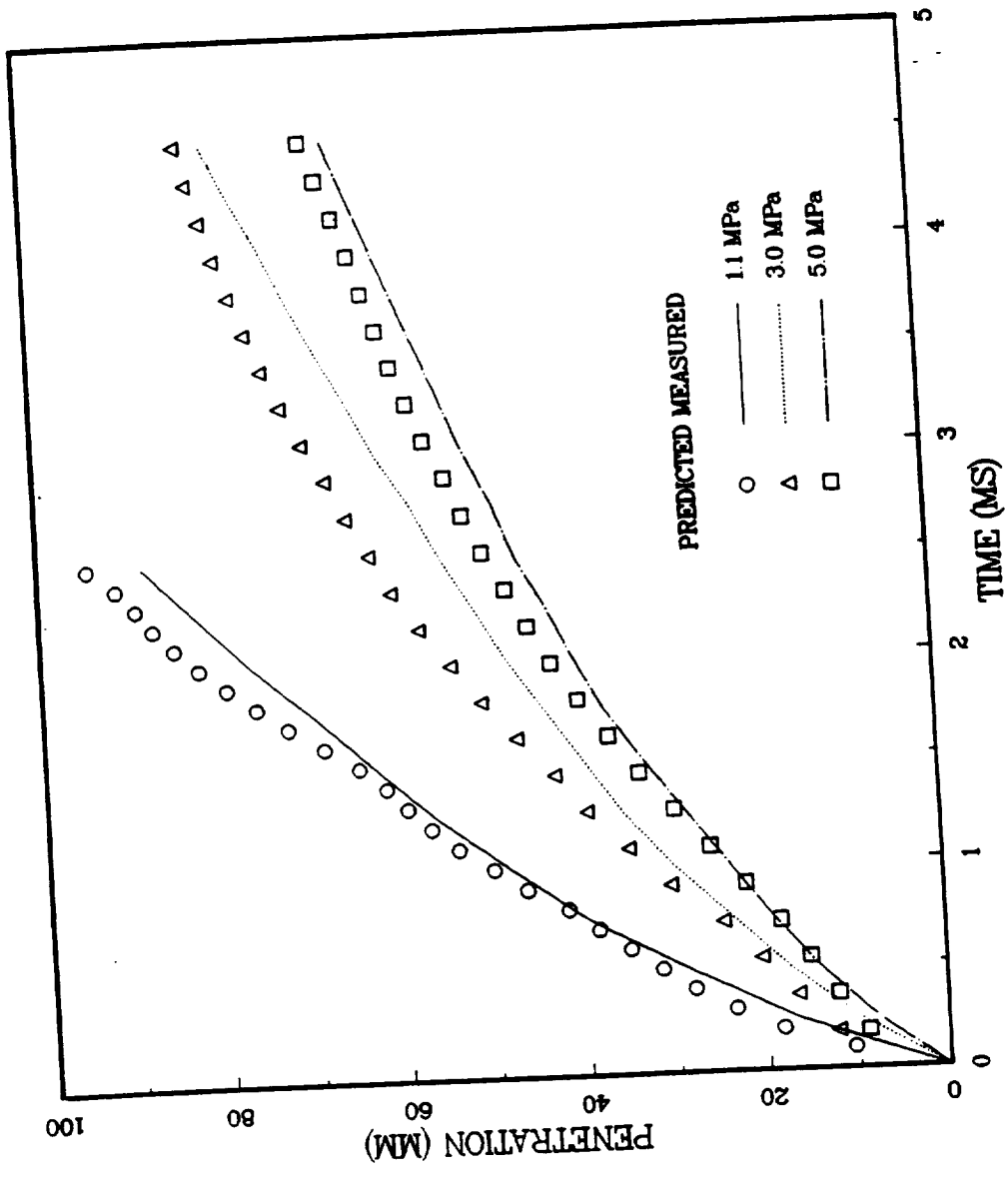

Figure IV.20: Spray tip penetration versus time in a solid-cone spray (Reitz's model).

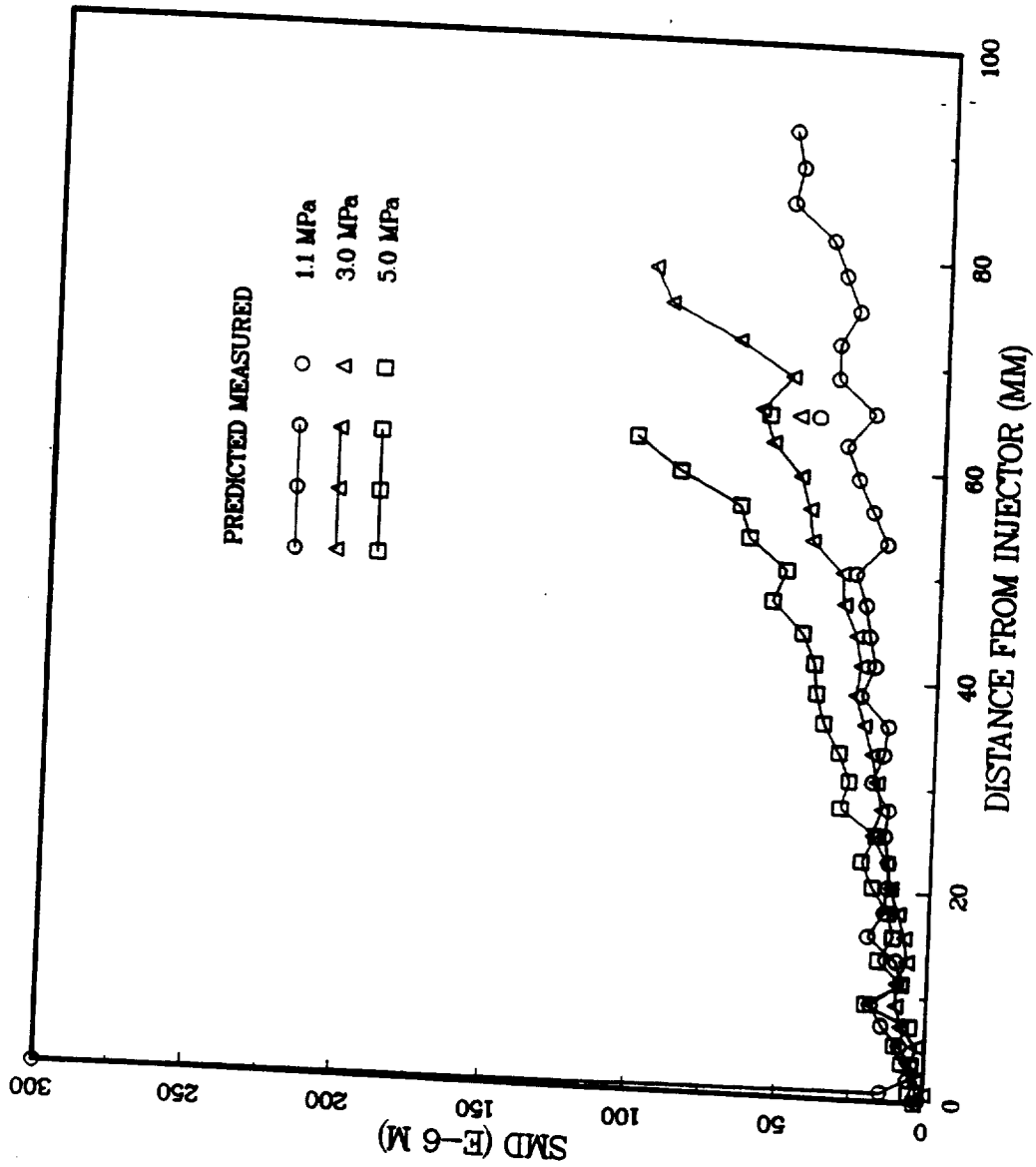

Figure IV.21: Sauter mean diameter versus distance from the injector (TAB model).

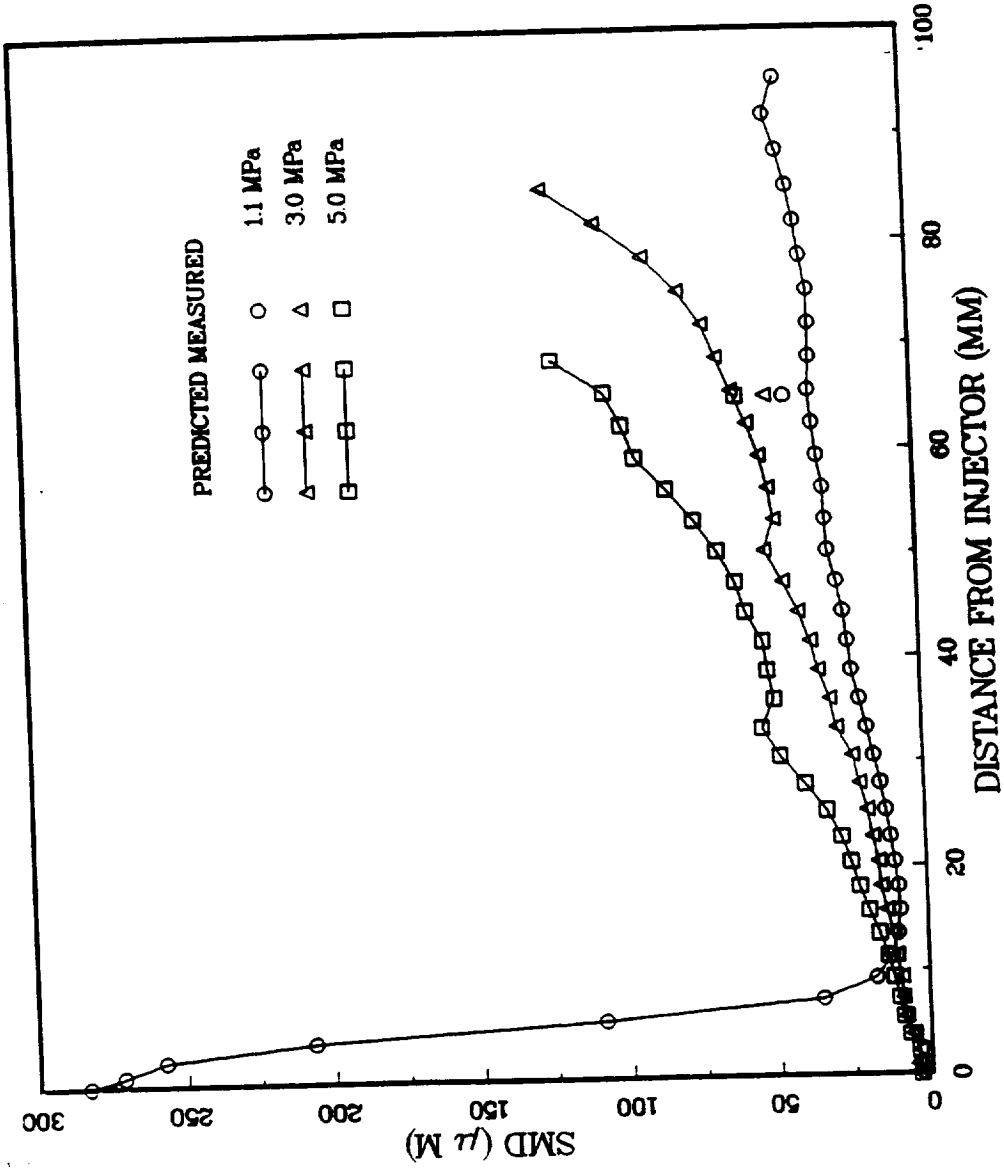

Figure IV.22: Sauter mean diameter versus distance from the injector (Reitz's model).

the far-downstream region. For the high pressure cases(3.0 and 5.0 MPa), the drop size increases largely in far-downstream region, because higher gas densities promote collisions and coalescence. This trend is also observed in the measurements. The predicted drop sizes at 65 mm qualitatively agreed with the experimental data for all three cases. The discrepancy could be associated with the fact that the experimental sprays were pulsed while the computations assumed a constant pressure injection for the entire computational time period. In comparison with the Reitz's model, the TAB model provides the relatively rapid breakup rate near the injector and the relatively low SMD distribution for three cases. Especially close to the injector for the low gas pressure case(1.1 MPa), the TAB model predicts the much faster breakup than the Reitz's model. Due to this faster breakup rate near the injector, the TAB model underpredicts the intact core length for three cases. The larger SMD distribution predicted by the Reitz's model could be tied with to the overprediction of the spray penetration length.

IV.2.2 Measurements of Wu et al.

To compare with the local flow properties in terms of the velocities and the turbulent intensities for gas and droplet, the measurements of Wu et al. [120] were selected. In this experiment, axial and radial components of the droplet velocity were measured by laser Doppler velocimetery (LDV) within liquid n-hexane sprays injecting into high-pressure nitrogen from single-hole cylindrical nozzles at room temperature. It was found that beyond 300 nozzle diameters from the nozzle that the fully developed incompressible jet structure and droplet-gas equilibrium were being approached.

Because this is a steady state case, no initial conditions are required. The grid

Table IV.4: Test Conditions for the Measurement of Wu et al.

Nozzle diameter: 127 μm Injection pressure: 9.9 MPa

Liquid: n-hexane Density: 665 kg/m^3

Viscosity: $3.2 \times 10^{-4} N \cdot s/m^2$ Surface tension: 0.0184 N/m

Ambient gas: nitrogen Temperature: $25°C$

Case	Pinj (MPa)	Pgas (MPa)	ρ_{gas} (kg/m^3)	Vinj (m/s)	x/d_0
A	12.5	1.48	17.02	127.0	400
B	15.2	4.24	48.68	127.0	500
C	30.4	4.24	48.68	194.0	500

system and boundary conditions are the same as the previous case, shown on Figure IV.12. The time-step sizes used for three test cases are 20, 20 and 10 μs respectively. At the beginning of the calculation, larger time-step sizes are used to establish the gas flow field, and then the above small time-steps are used for two-phase calculations. 300 time steps are used to obtain statistically steady results. The droplet properties and three injection conditions are listed on Table IV.4.

In this experimental setup, the gas turbulent round jet was developed by the injection of liquid fuel and its atomization. Two-phase flow was fully coupled by

gas-droplet momentum exchange especially in the immediate vicinity of the nozzle exit. For the present dense spray, it is of interest to establish the importance of droplet modulation to gas turbulence and compare with the available experimental measurements. Before getting into the detailed comparison with the experimental data, the effect of drops on the turbulence is studied with several modulation models. In the following figures, *Model* 1 corresponds to the model suggested by Mostafa and Mongia [83]; *Model* 2 by Amsden et al. [4] and *Model* 3 by Chen and Wood [78].

Figure IV.23 shows the predicted gas-phase centerline velocity with and without modulation terms in standard $k-\epsilon$ equation. Close to the nozzle, all models predict the peak velocity at the nearly same axial location. However, there exists differences of the centerline velocity distribution near the nozzle exit. At downstream of the peak point, the standard $k-\epsilon$ model without modulation effect predicts the fastest decay of the centerline velocity followed by *Model* 2, *Model* 1 and *Model* 3. In the far downstream, all models predict similar slopes due to the relatively small effects of the turbulence modulation. Therefore, the turbulence modulation is important in the jet developing region. *Model* 1 and *Model* 3 show the favorable agreement with the far-field measured velocities(Case C). Figure IV.24 shows the centerline turbulent kinetic energy with four models. Around the peak point, *Model* 1 predicts the lowest turbulence level followed by *Model* 3, *Model* 2, and no-modulation case. In the far field, *Model* 1 and *Model* 3 have the almost same turbulence level.

Figure IV.25 shows the comparison of predicted and measured centerline velocity for the three test conditions. Predictions based on *Model* 1 have a good agreement with measurements for three test cases. Figure IV.26 shows the radial profiles of gas

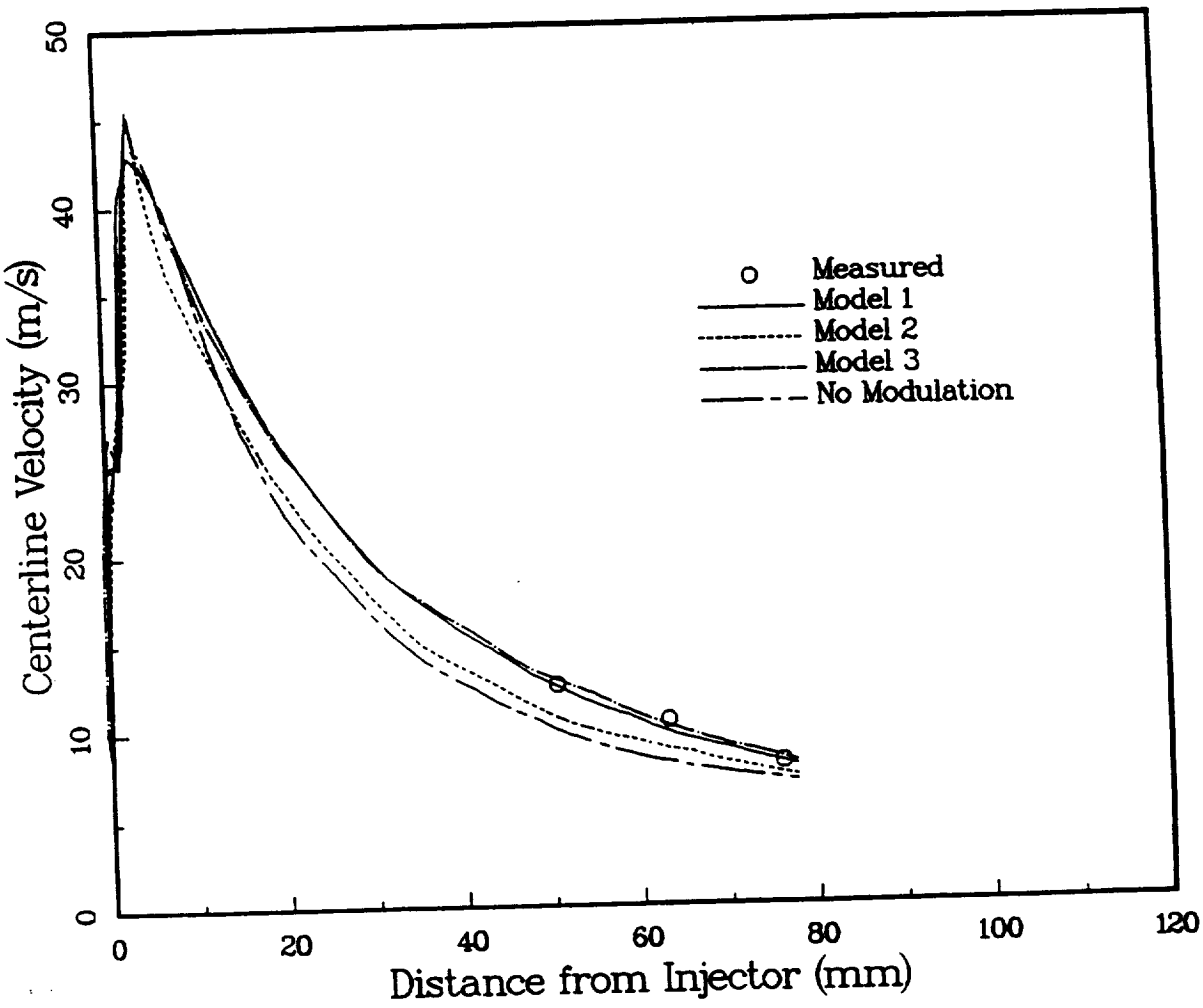

Figure IV.23: Gas-phase axial centerline velocity (Case C)

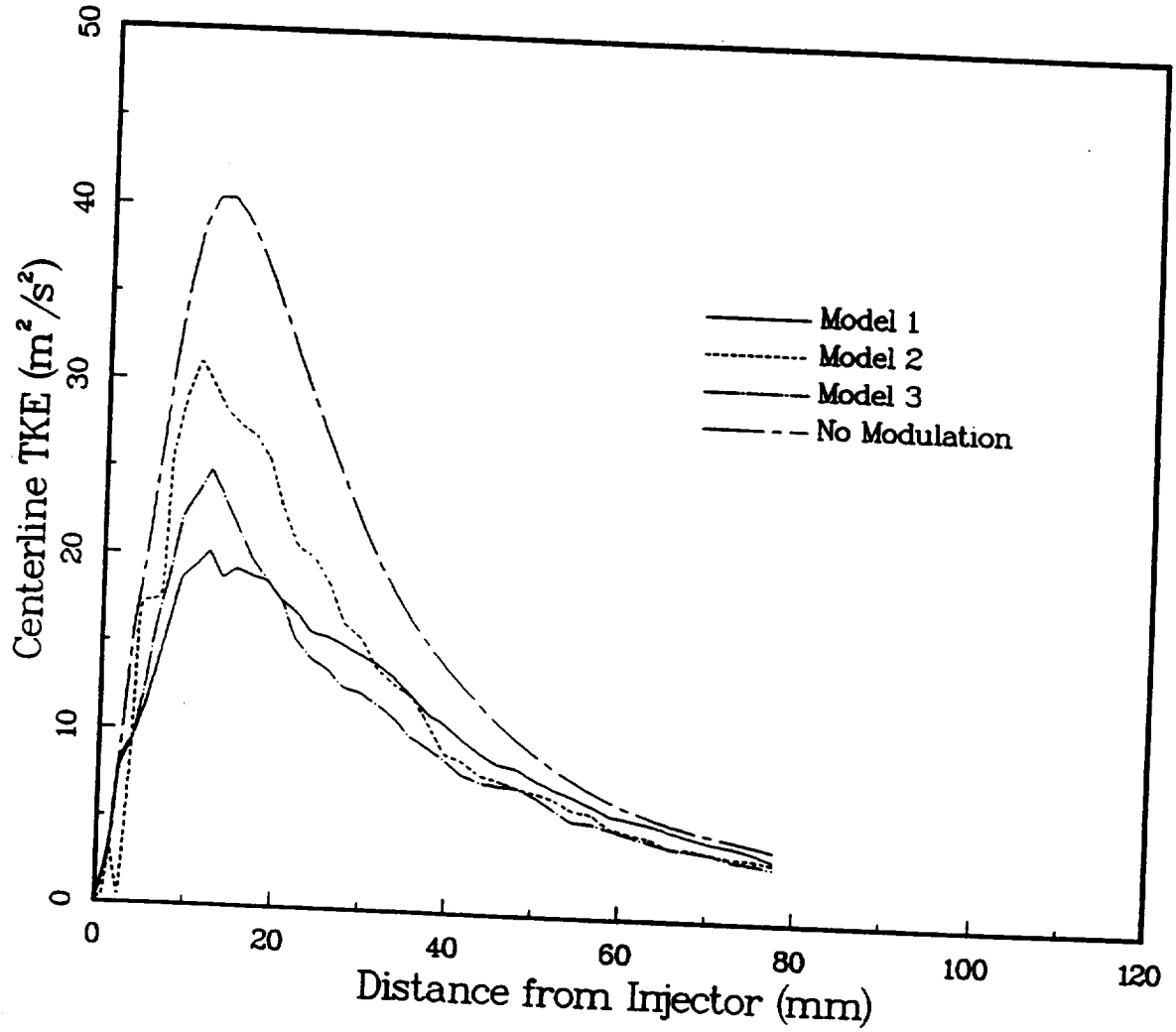

Figure IV.24: Gas-phase axial centerline turbulent kinetic energy (Case C)

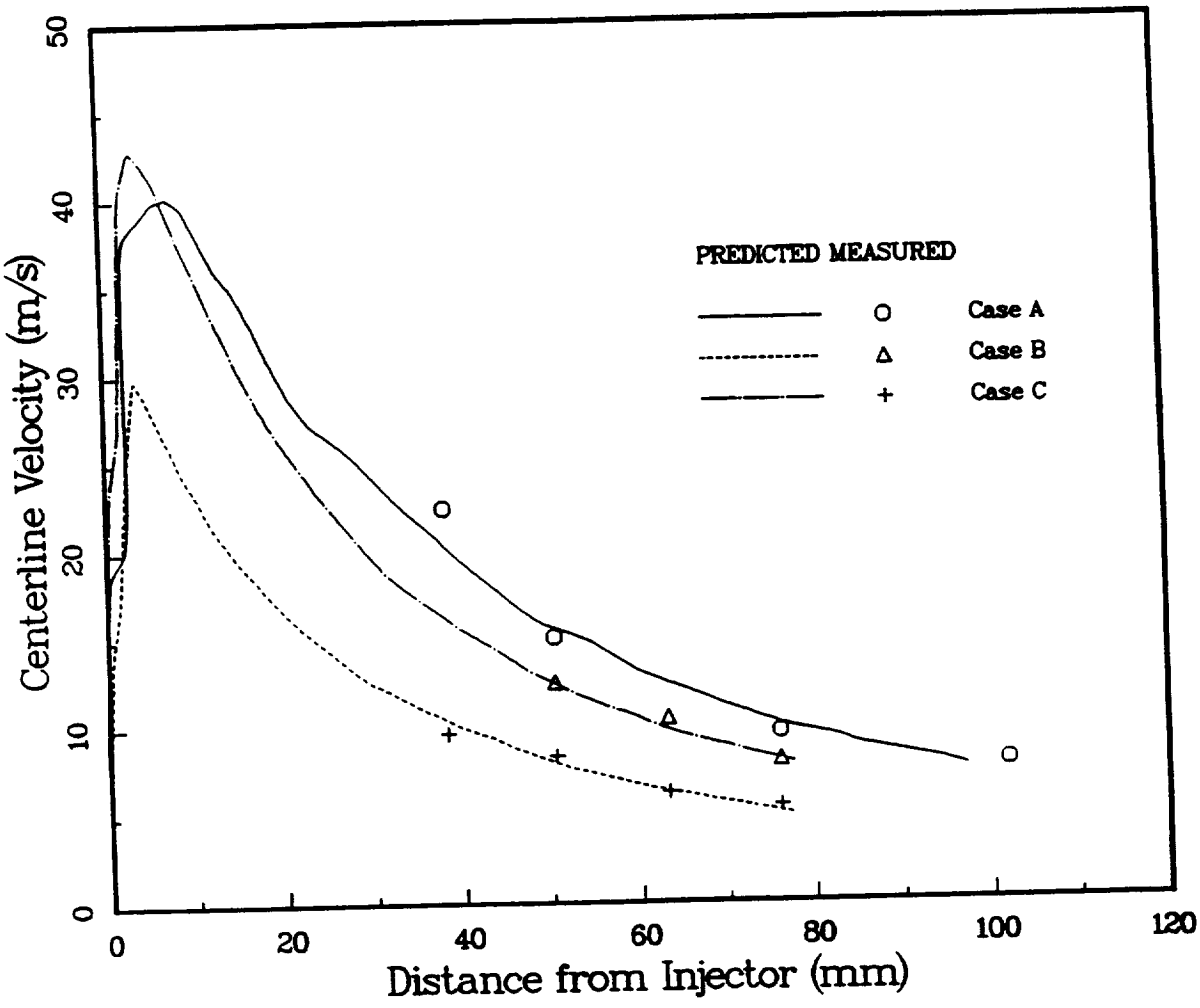

Figure IV.25: Gas-phase axial centerline velocity for three test conditions

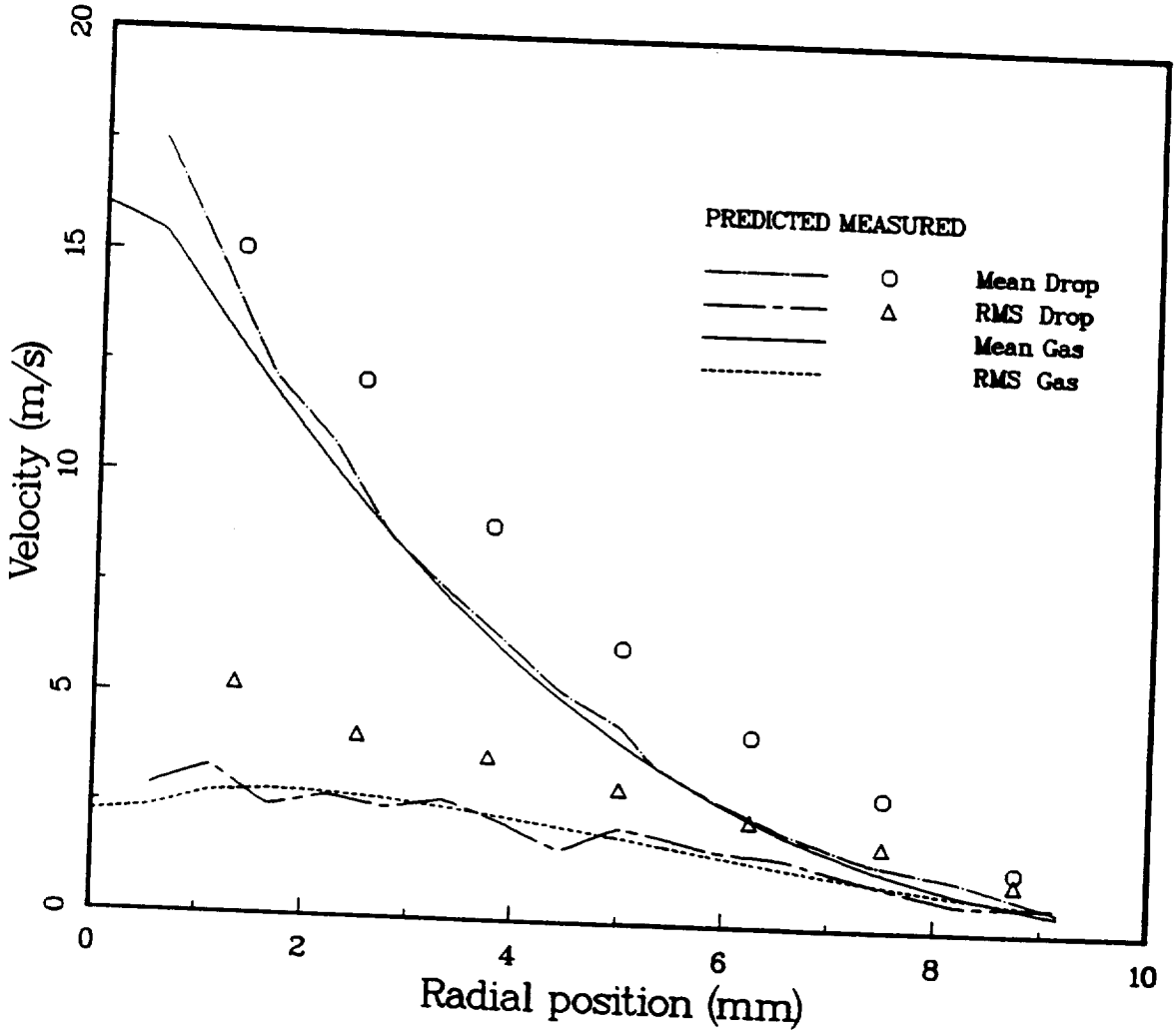

Figure IV.26: Radial profiles of gas/drop axial mean and RMS velocity (x=50.8mm, Case A)

and drop axial mean velocity and RMS velocity at axial location of 50.8 mm (400 nozzle diameters, Case A) from the injector. The predicted mean drop velocities weighted by the drop number are obtained by averaging the instantaneous values over $6ms$ period. The predicted mean and RMS velocities are somewhat lower than measured data(Case A). As would be expected, the predictions for gas and drop velocities are in almost equilibrium at this downstream location.

The predicted and measured results for Case B are shown in Figure IV.27. The corresponding axial location in Case B is 63.5 mm (500 nozzle diameters) from the injector. The computed mean and RMS velocities are favorably agreed with the experimental data. The slight oscillations in the predicted drop velocity profile are due to undersampling of computational parcels. Figure IV.28 summarizes the results for Case C at axial location of 63.5 mm from the injector. In this case, the overall agreement is good in the mean and RMS velocities. However, around radial location of 4.5 mm, the predicted mean drop velocities are somewhat lower than the measurements. The previous numerical study of Reitz and Diwakar[97] showed the similar trend with the present study.

Figures IV.29, IV.30 and IV.31 show the radial profiles of the mean gas and drop velocities, and the instantaneous drop velocities using the SSF model and the parcel PDF model for three cases. The number of computational parcels for the SSF model and the parcel PDF model is about 3600 in the whole flow field. Compared to the parcel PDF results, the computed profiles of the SSF model for three cases are very irregular and oscillatory. The parcel PDF model provides the realistic and similar distributions with the mean drop profiles. Due to slight undersampling, certain level of irregularities exist in the distributions of mean drop velocities and instantaneous

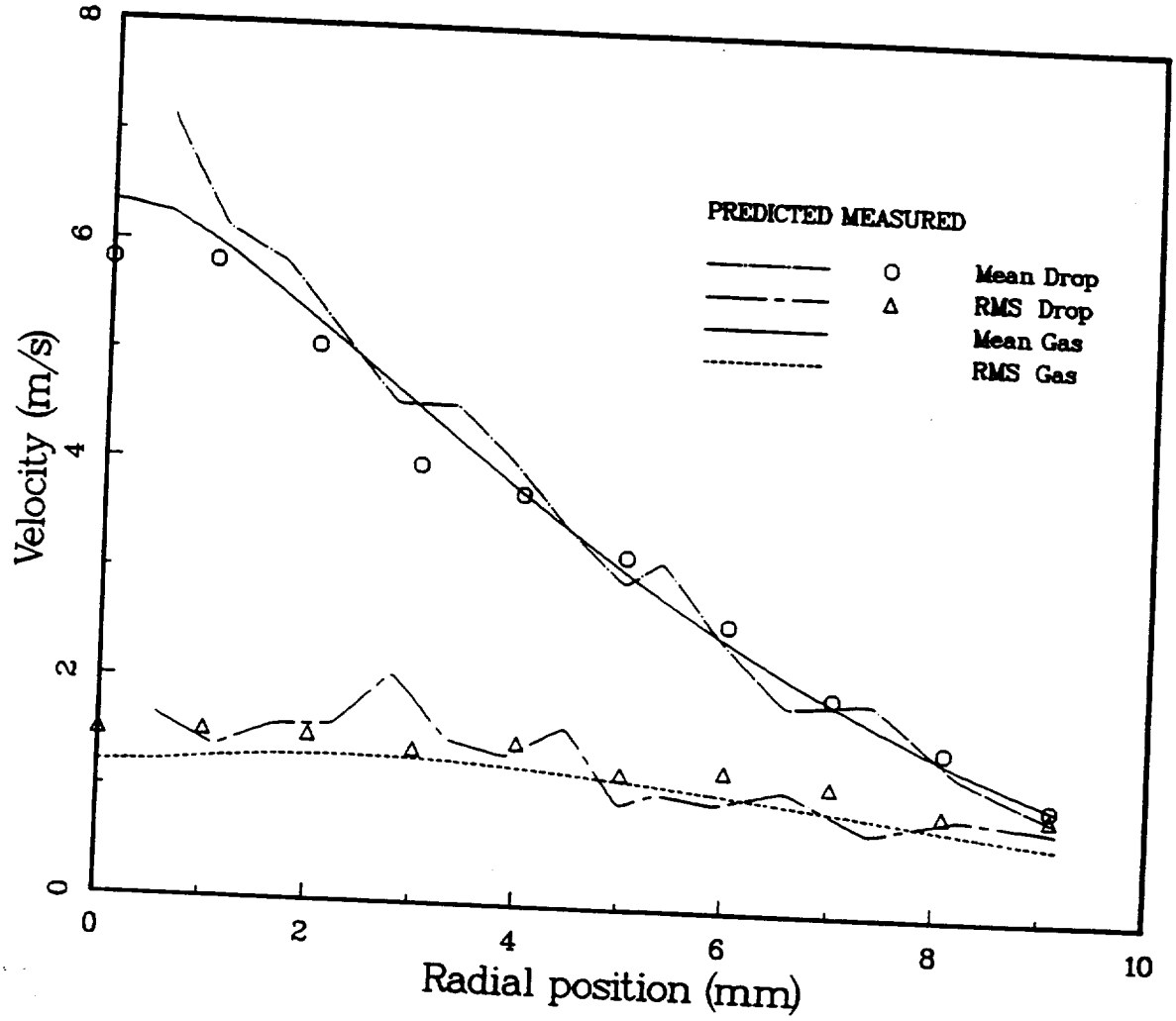

Figure IV.27: Radial profiles of gas/drop axial mean and RMS velocity (x=50.8mm, Case B)

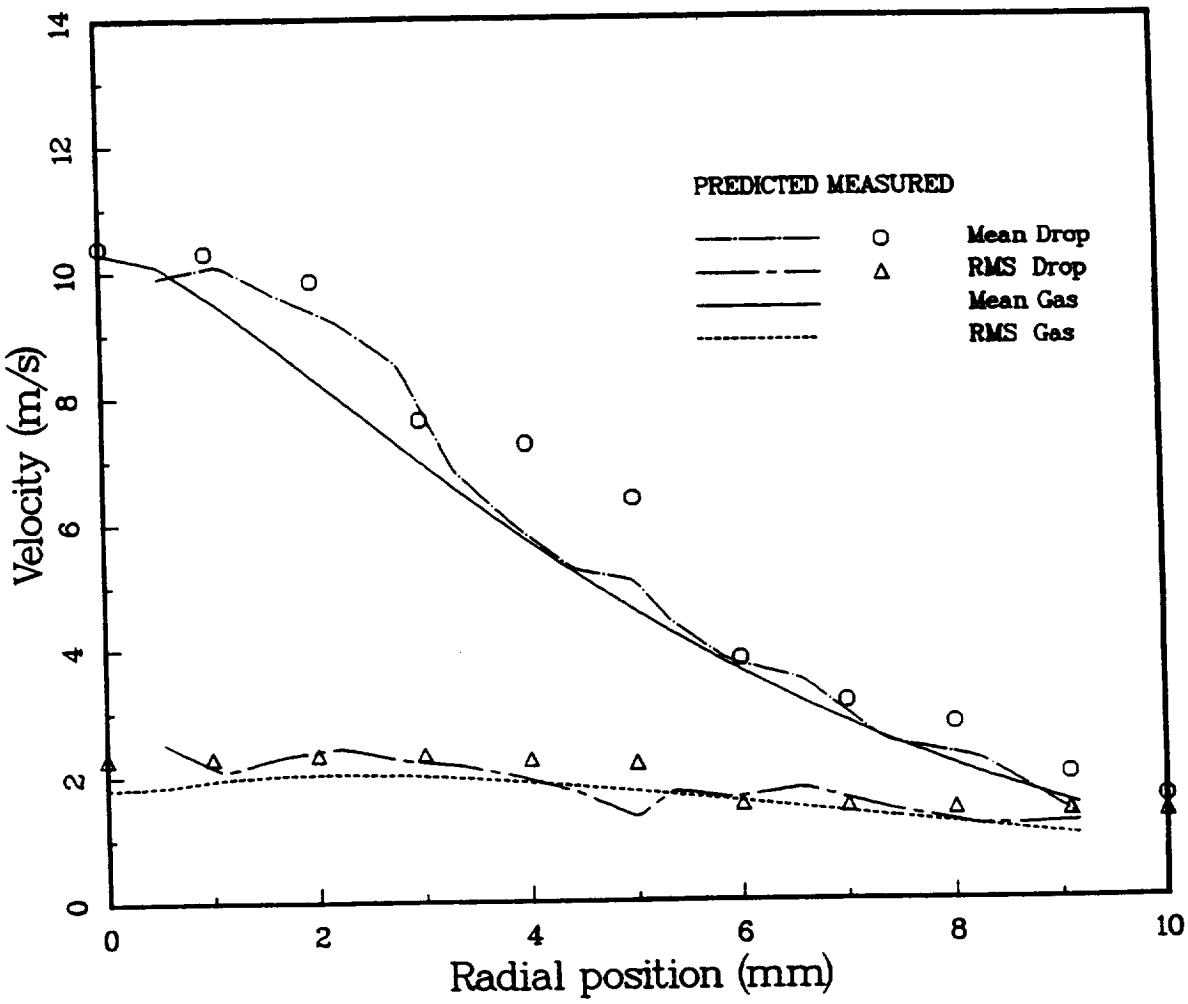

Figure IV.28: Radial profiles of gas/drop axial mean and RMS velocity (x=50.8mm, Case C)

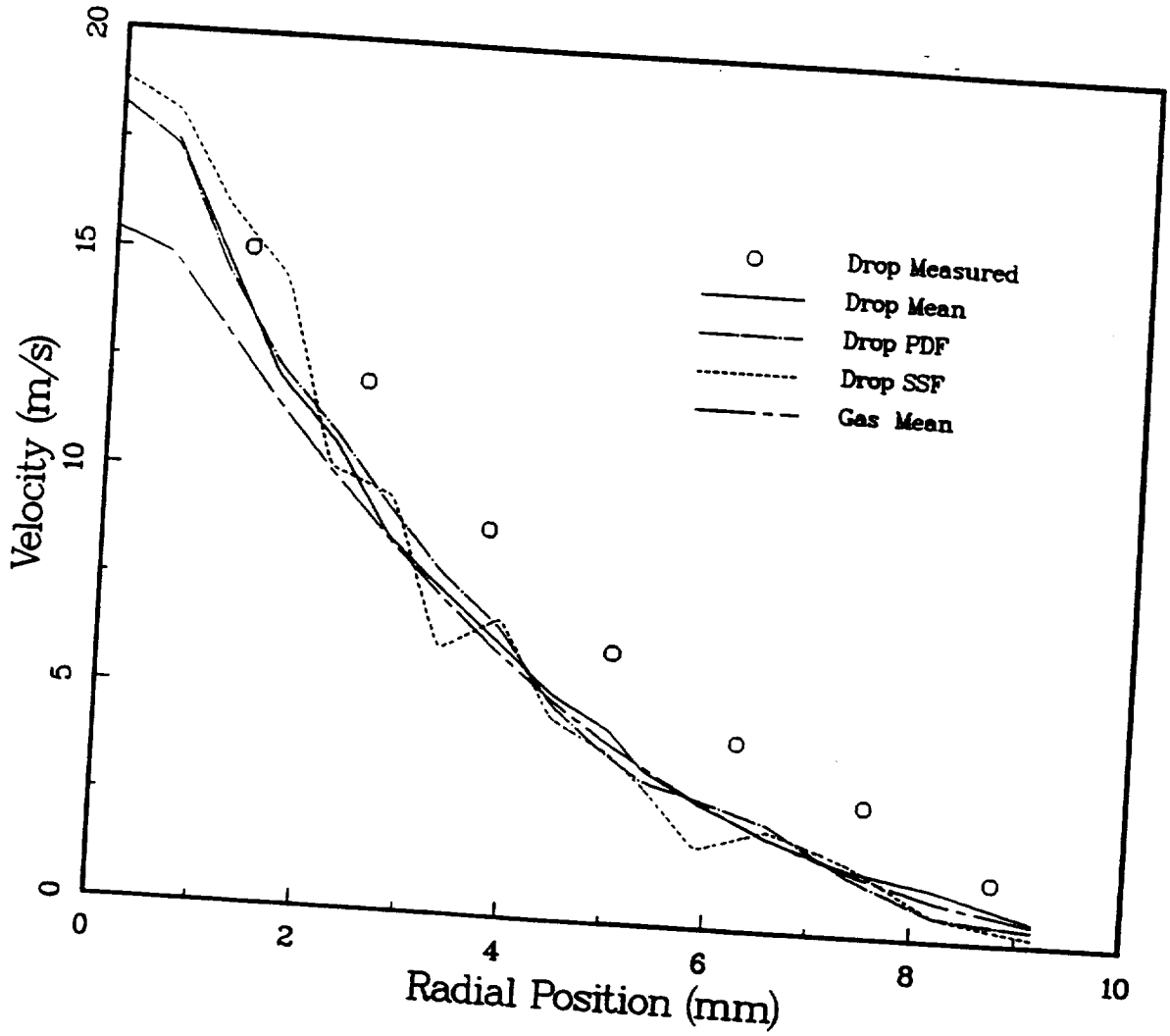

Figure IV.29: Radial profiles of gas/drop mean and instantaneous axial velocity comparisons with PDF (Case A)

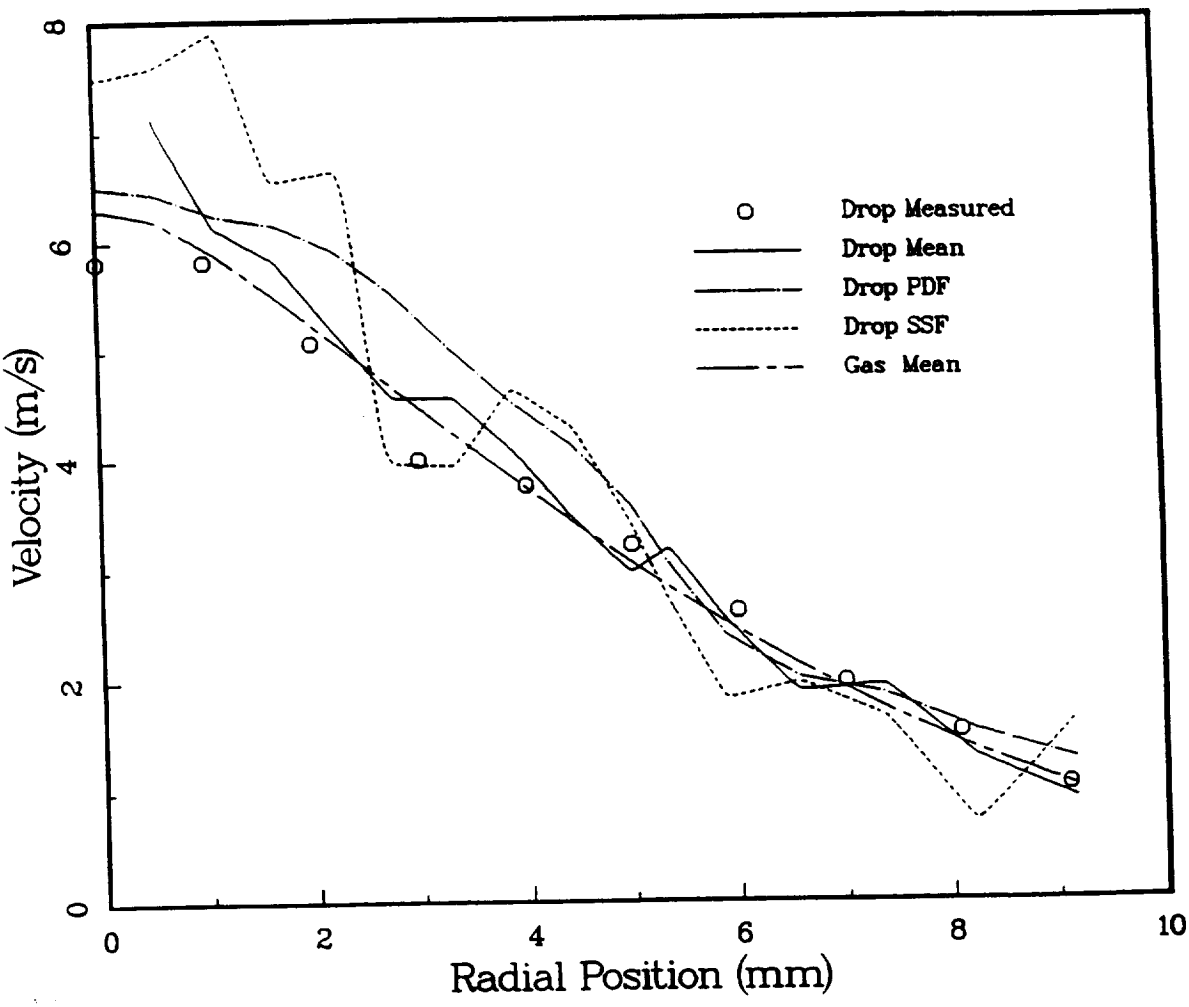

Figure IV.30: Radial profiles of gas/drop mean and instantaneous axial velocity comparisons with PDF (Case B)

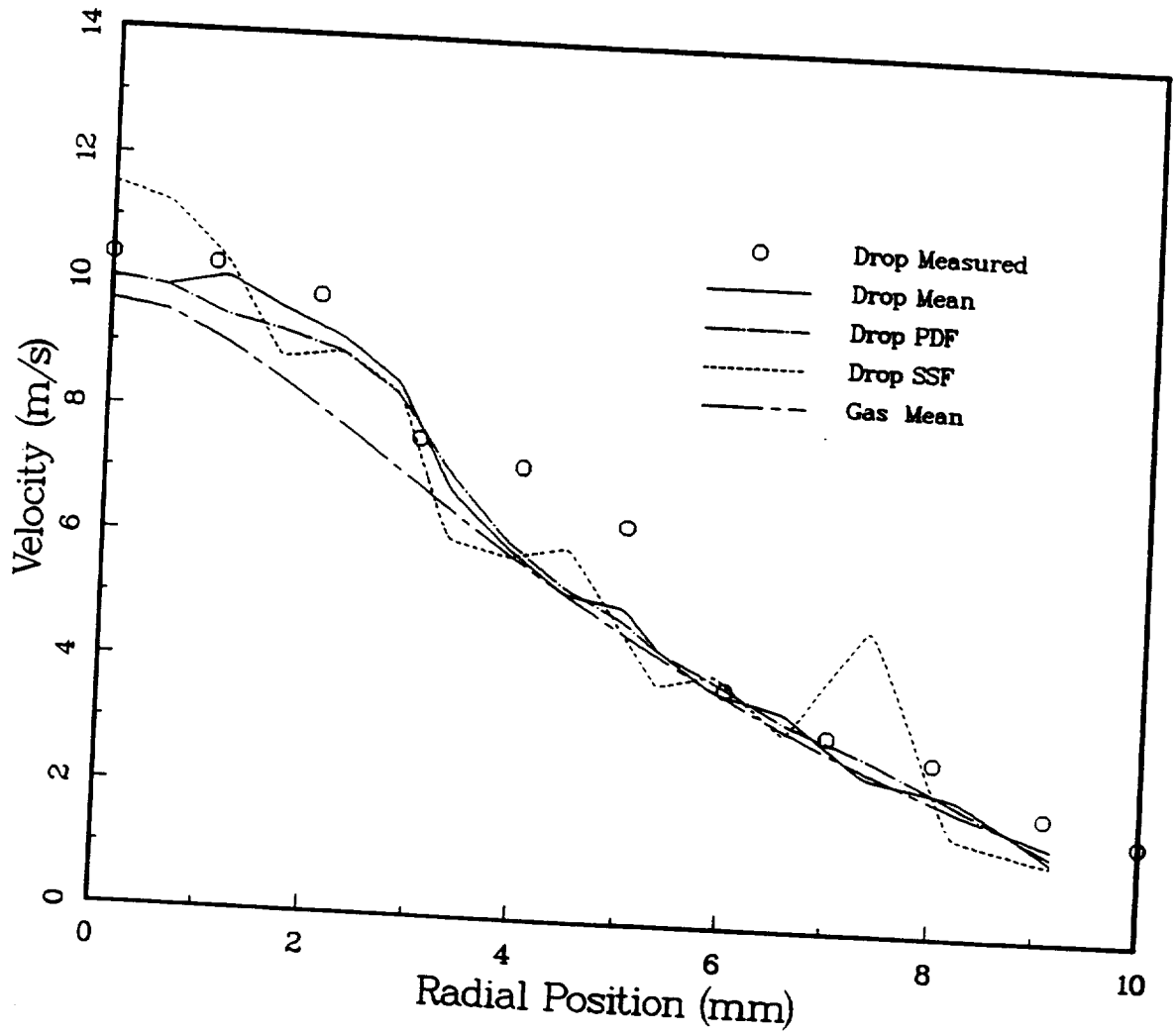

Figure IV.31: Radial profiles of gas/drop mean and instantaneous axial velocity comparisons with PDF (Case C)

droplet velocities using the parcel PDF model. Compared to the SSF calculations with the same number of computational parcels, the CPU time with the parcel PDF model is increased about 10%. However, to reach the same level of the realistic distributions of the parcel PDF model, the SSF model needs to increase the number of the computational parcels at least several times which results in the drastic increase in CPU time and the memory storage requirement. Furthermore, the irregular drop/gas distributions due to the undersampling of the computational parcels in the SSF model can create numerically oriented high-frequency noises which possibly contaminate the high-frequency combustion instability solutions. The present parcel PDF method has potential advantage to eliminate numerically oriented noises associated with the droplet injection as well as to reduce the number of computational parcels with accurate representation of spray dynamics. The results indicated that the present parcel PDF model has the capability of accurately representing drop dispersion in dense sprays with manageable number of computational parcels.

IV.3 Non-Evaporating Hollow-Cone Spray

The hollow-cone spray tip penetration data of Shearer and Groff [105] have been used for the model validation. In the experiment, the liquid fuel (indolene-clear gasoline) is injected into quiescent room-temperature nitrogen at $P = 550kPa$. A computational domain of 20 mm in radius and 40 mm in axis was uniformly discretized by 41 and 81 grids respectively as shown on Figure IV.32 with boundary conditions. The experimental spray cone angle is 60 degrees, and the flow rate 0.0165 ml/injection with four pulses, each of duration about 0.58 ms. The droplet injection velocity could be approximated as a constant through the injection [96] and is set

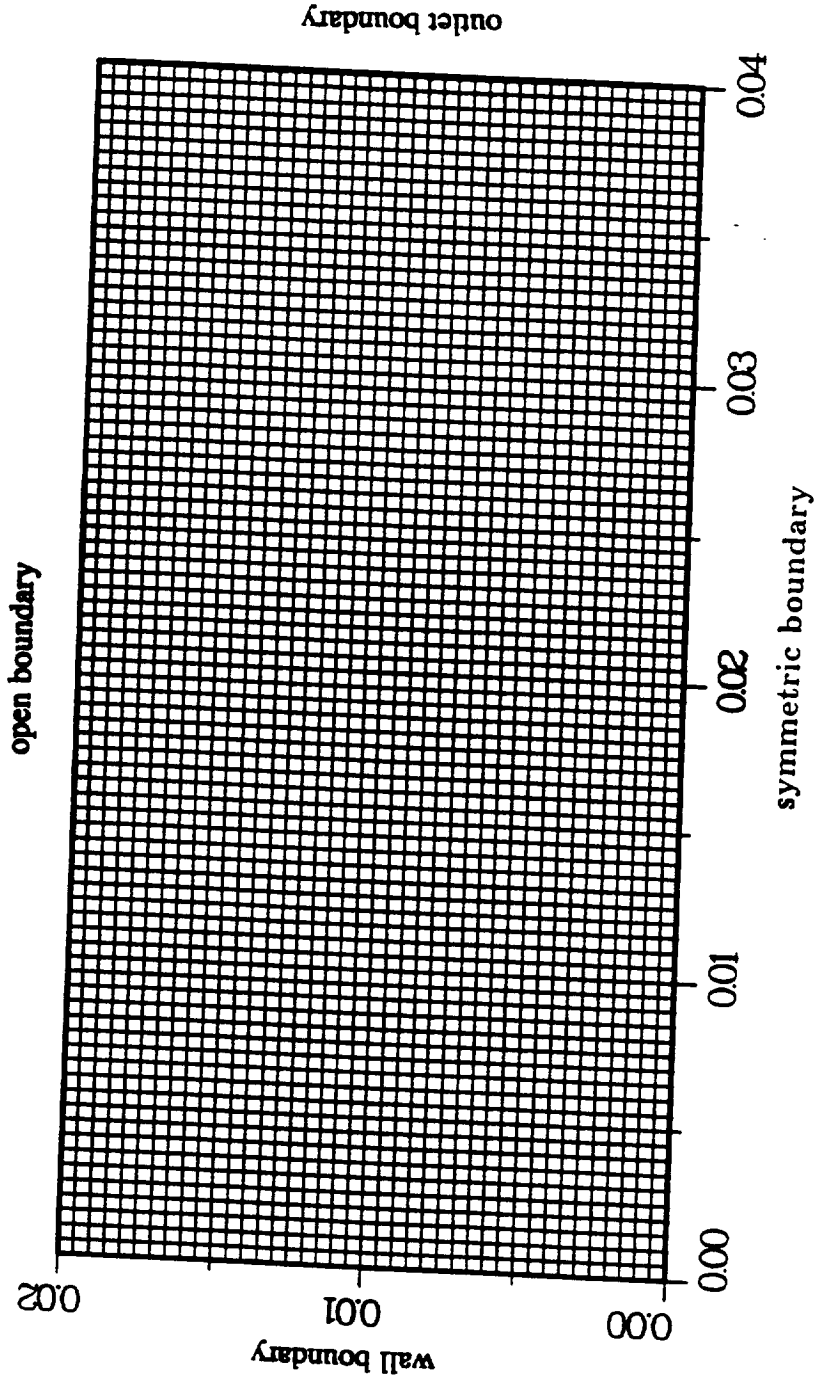

Figure IV.32: Grid system and boundary conditions of hollow-cone spray.

Table IV.5: Test Conditions for the Measurement of Shearer and Groff

Pgas (kPa)	ρ_{gas} (kg/m^3)	Vinj (m/s)	VOLinj (ml/inj)	Cone Angle (deg)
550	6.36	60	0.0165	60

to the experimental spray tip velocity ($60m/s$) measured from the movie pictures in the early stage of the injection. Turbulence modulation model and PDF model are not activated in this calculation. The TAB breakup model and collision model are used to account for the effect of droplet breakup and collision/coalescence. 10 droplets are injected each time step with the same size as the nozzle diameter 60 μm. The numerical timestep size is $10\mu s$ and about 1200 spray parcels are present at time 1.32 ms (132 time steps) in the computation with 141 second CPU time on CRAY X-MP/24.

Figures IV.33,IV.34,IV.35,IV.36, IV.37 and IV.38 show the spray parcel distributions and the velocity vectors with time advancing. The numerical results indicate that turbulence has a relatively small effect on penetration in a hollow-cone spray because the radial spreading due to inertia is the dominant factor. The gas velocity vectors indicate the presence of a vortex near the head of the spray, which curls the spray tip toward the outside of spray. A substantial region of strong inward flow in the center of the cone near the injector was also observed. These flow patterns

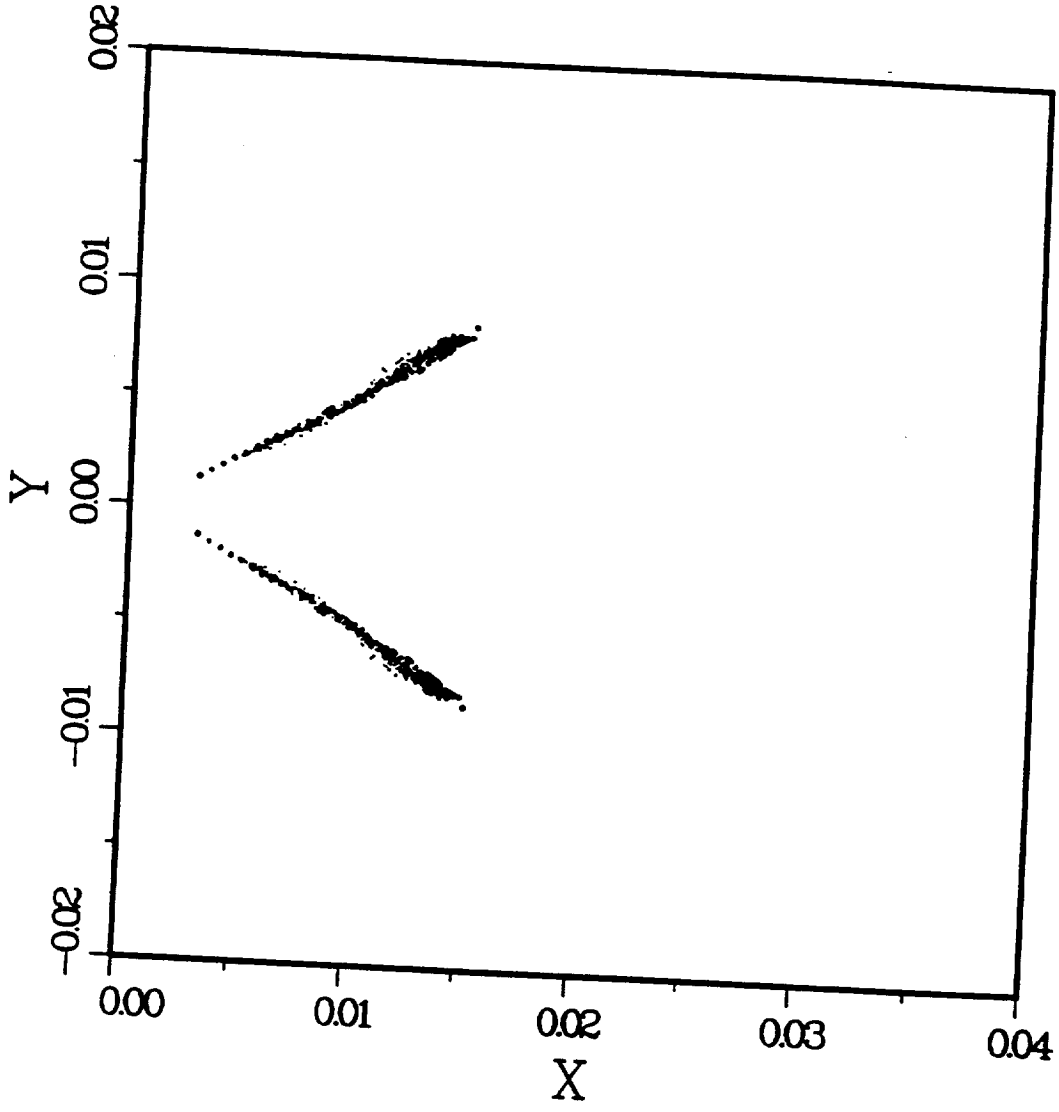

Figure IV.33: Spray parcel distribution in hollow-cone spray (Time=0.44ms)

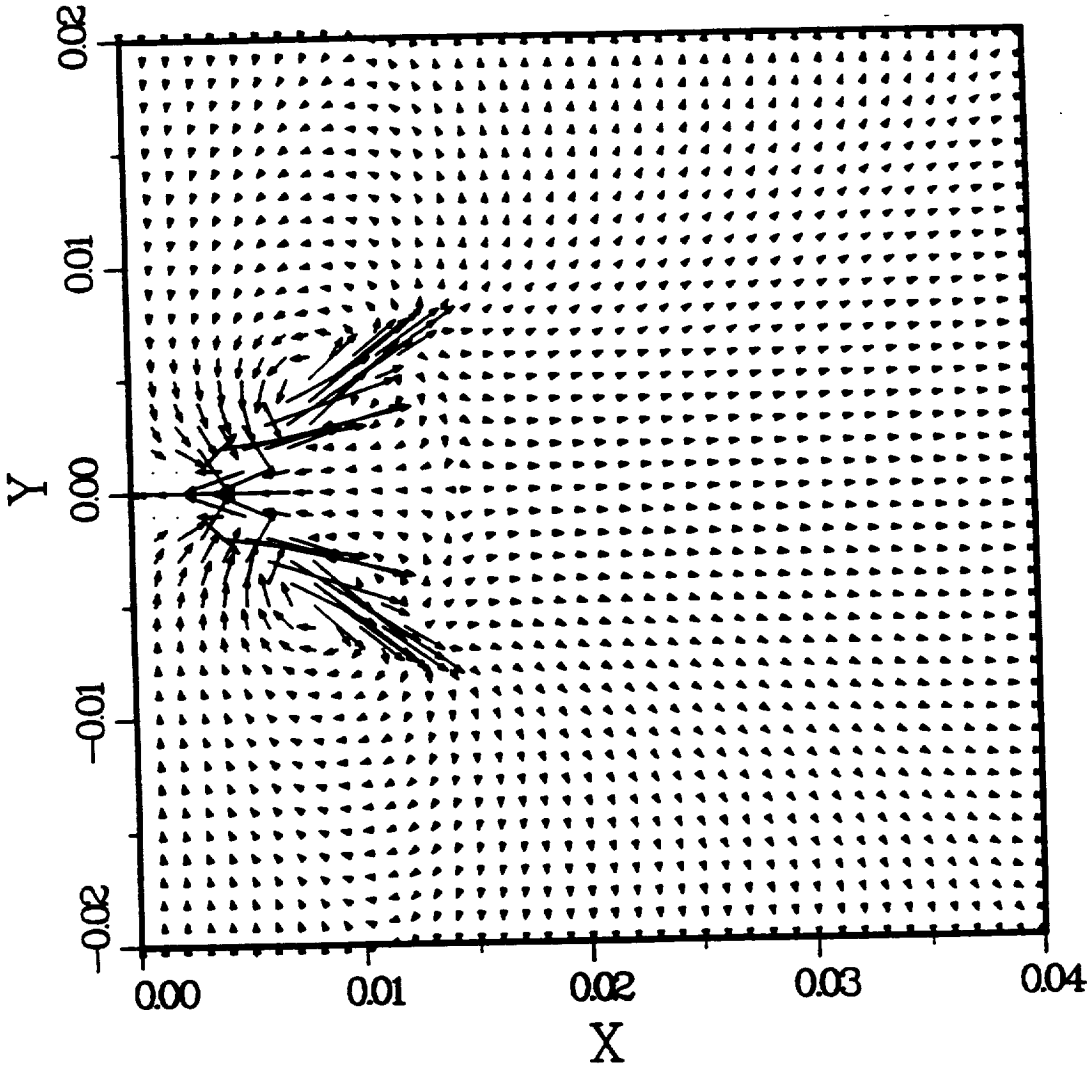

Figure IV.34: Velocity vectors in hollow-cone spray (Time=0.44ms)

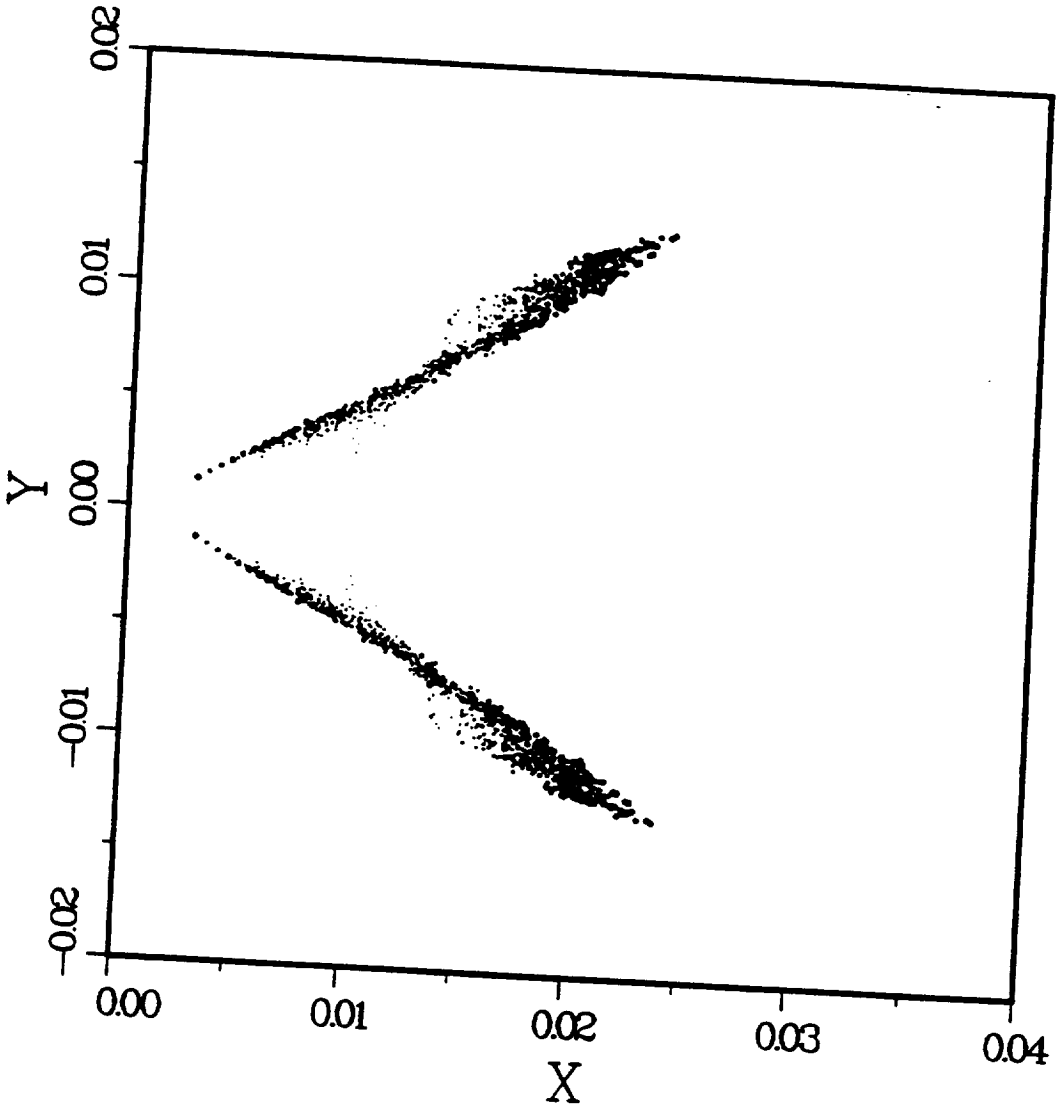

Figure IV.35: Spray parcel distribution in hollow-cone spray (Time=0.88ms)

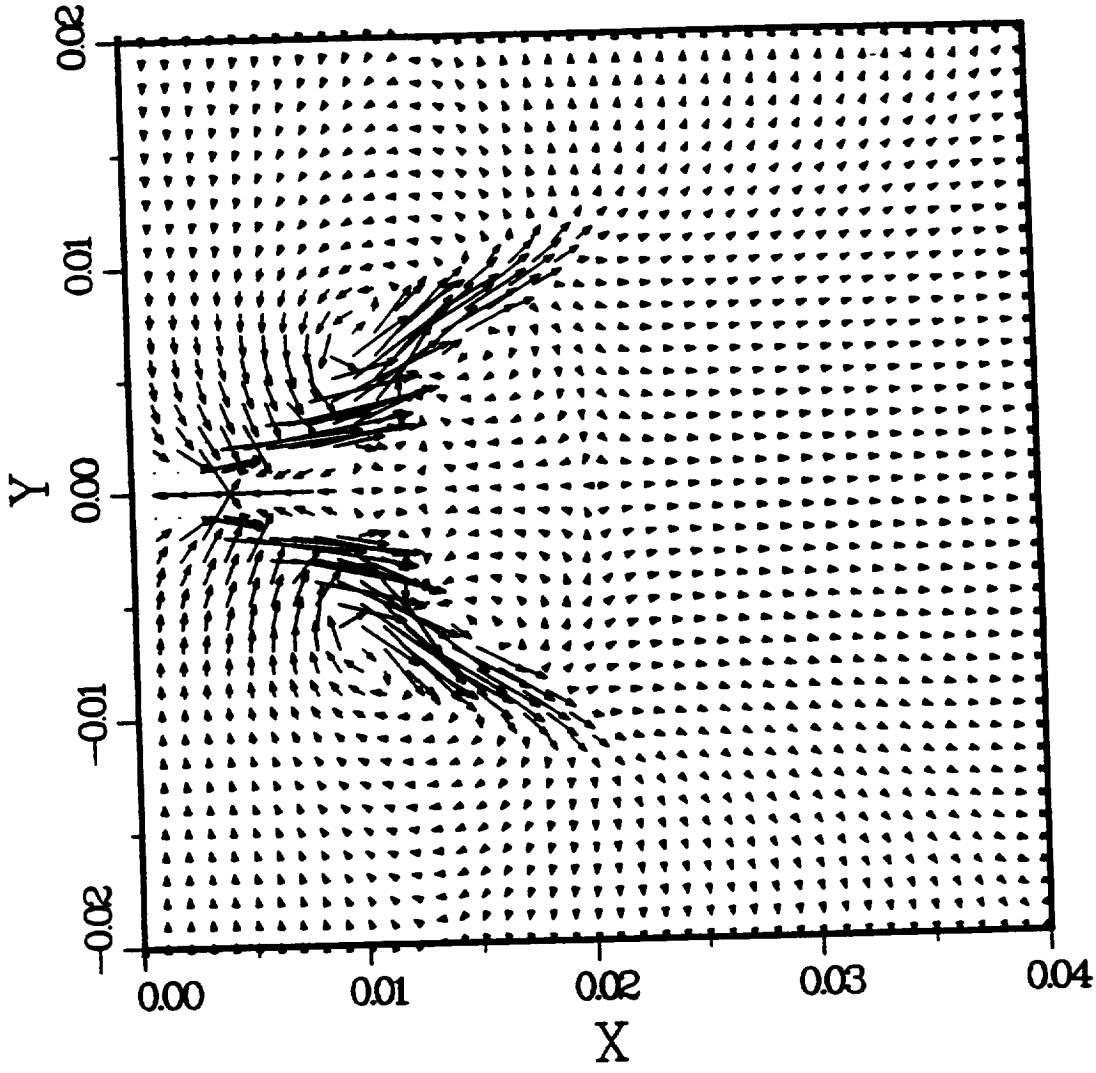

Figure IV.36: Velocity vectors in hollow-cone spray (Time=0.88ms)

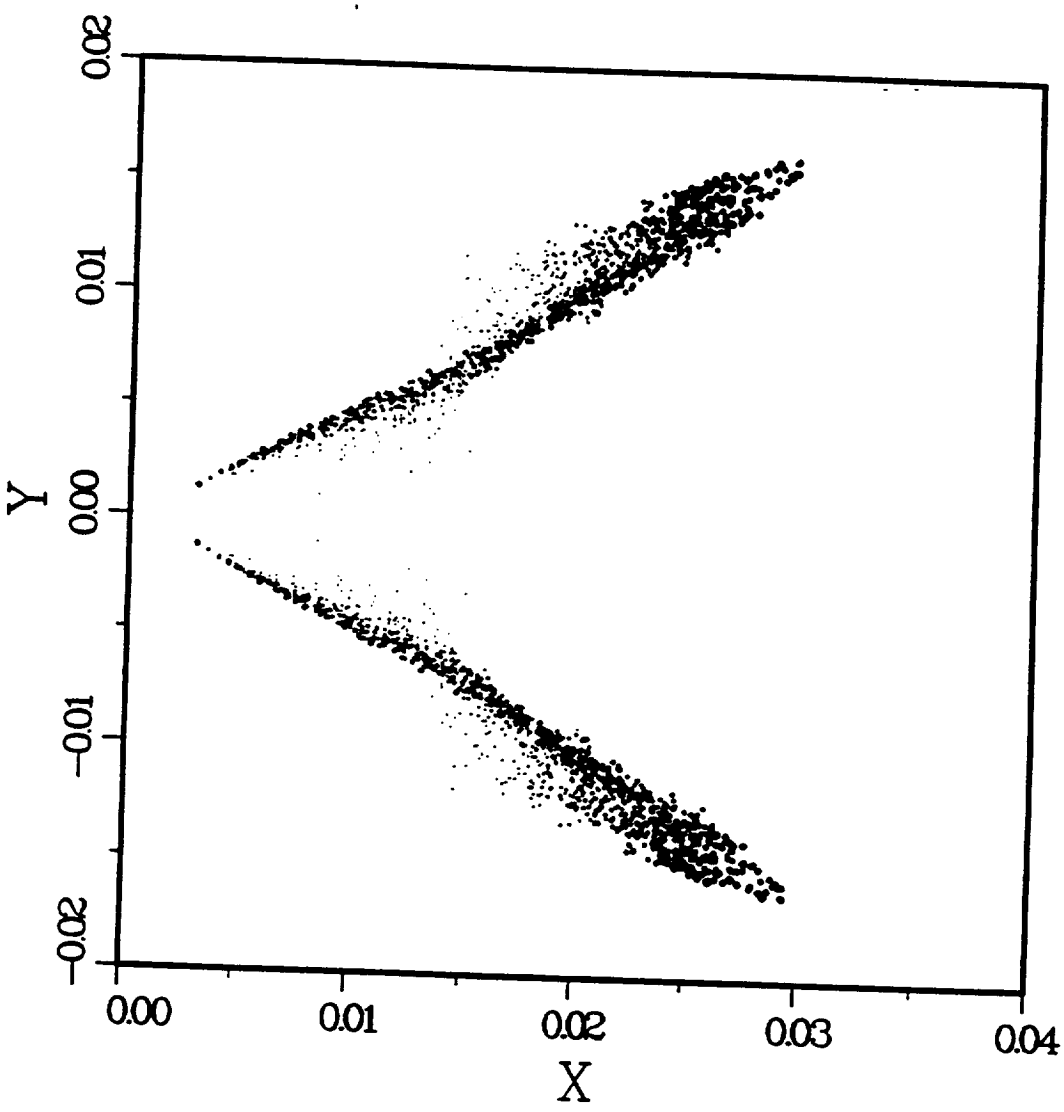

Figure IV.37: Spray parcel distribution in hollow-cone spray (Time=1.32ms)

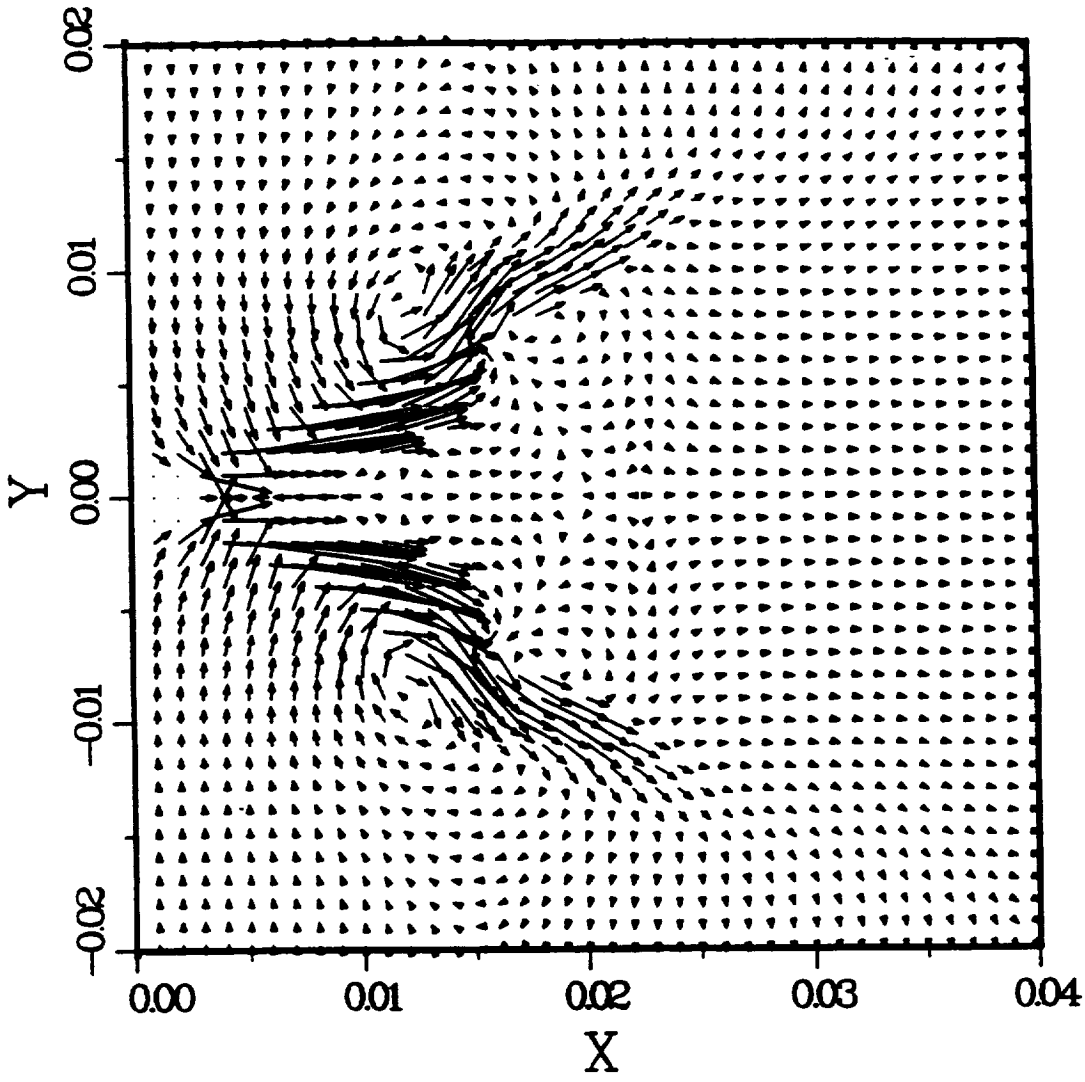

Figure IV.38: Velocity vectors in hollow-cone spray (Time=1.32ms)

and spray shapes clearly show a very complex structure of a hollow-cone spray and two-phase interactions. These results are compared favorable agreement with the experimental observations [105]. The predicted and measured spray tip penetration versus time are shown in Figure IV.39, and the present predictions show reasonable agreement with the experimental tip penetration.

IV.4 Evaporating and Burning Solid-Cone Spray

Table IV.6: Test Conditions for the Measurement of Yokota et al.

Case	Pinj (MPa)	Pgas (MPa)	Tamb (K)	Minj (kg/s)	Atmosphere
Evaporating Spray	30	3.0	900	0.00326	N_2
Burning Spray	30	3.0	900	0.00326	*Air*

The evaporating and burning solid-cone spray measurements of Yokota et al. [122] have been used to validate the present numerical dense spray model with droplet evaporation. Liquid fuel (tridecane $C_{13}H_{28}$) is injected through a single hole nozzle into high-pressure, high-temperature nitrogen or air. The test conditions for evaporating and burning sprays are given in Table IV.6. The nozzle diameter was 0.16 mm. A computational domain of 20 mm in radius and 100 mm in length was

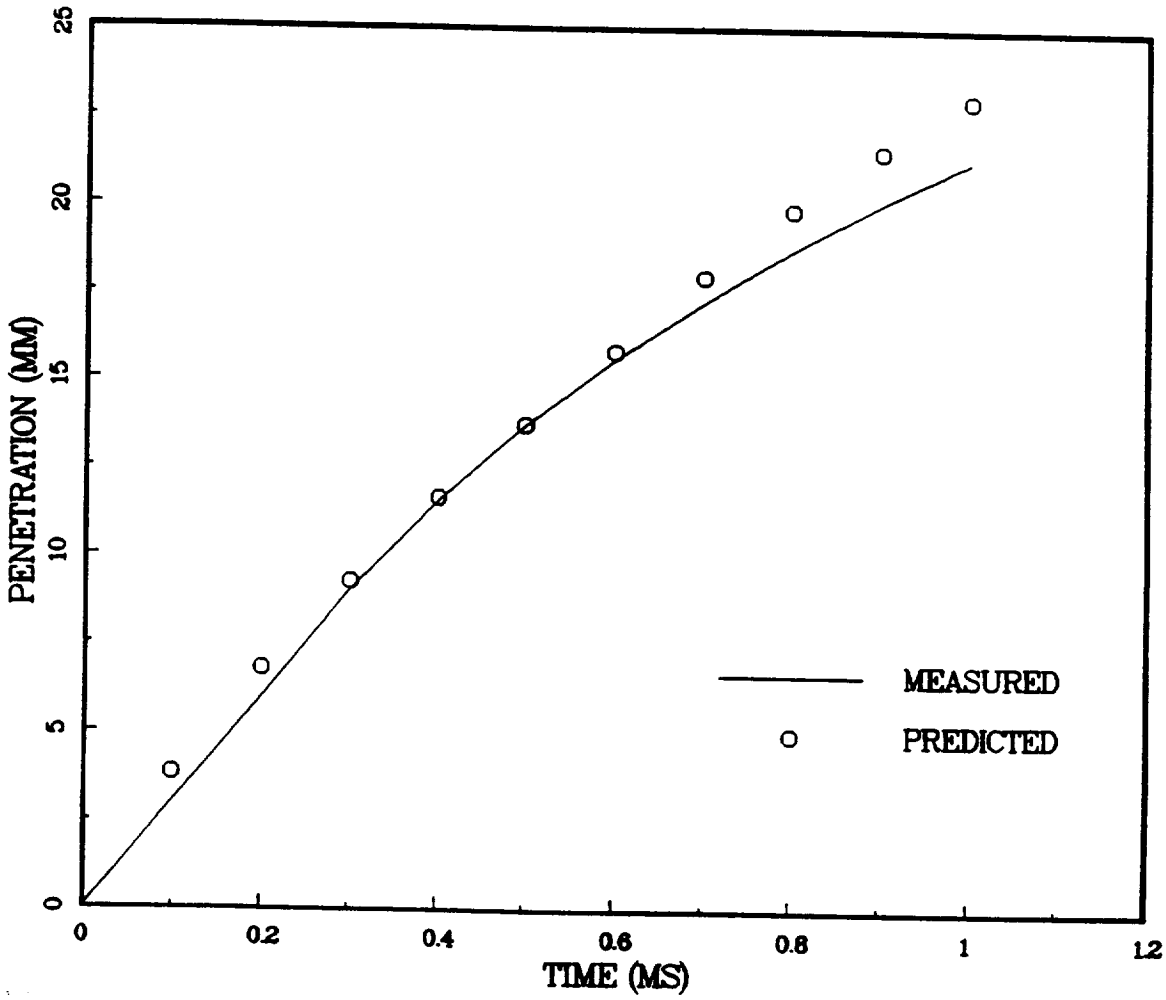

Figure IV.39: Spray tip penetration versus time in a hollow-cone spray

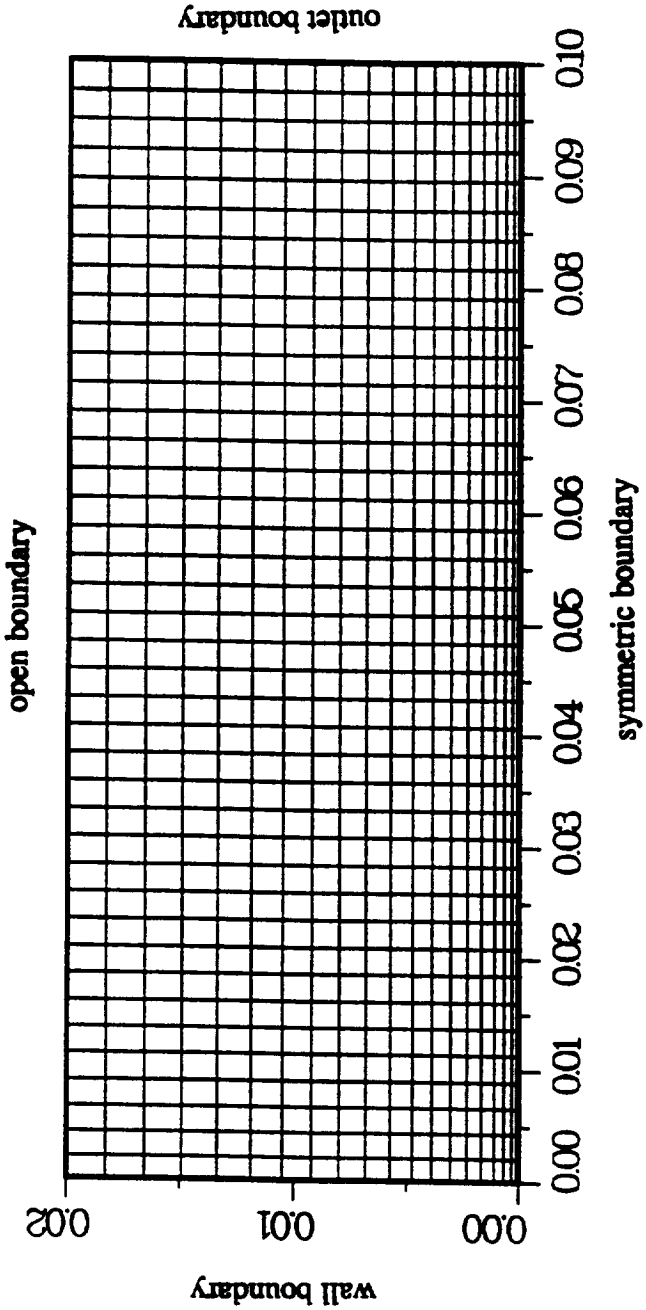

Figure IV.40: Grid system and boundary conditions of evaporating and burning cases.

Table IV.7: Properties of tridecane

ρ_d	840 kg/m^3	H_{com}	4.45 $\times 10^7$ J/kg
MW	184 kg/kmole	T_{cr}	677 K
T_d	300 K	V_{inj}	185 m/s
α_{350}	0.02126 N/m		

Table IV.8: Constants for gas property

AIRLA1	$2.52 \times 10^{-3} W/(m \cdot K)$	AIRLA2	200
AIRMU1	$1.46 \times 10^{-6} kg/(m \cdot s)$	AIRMU2	110

discretized by a 21 radial and 44 axial grids. The mesh spacing was nonuniform with refinement on the centerline and close to the injector. The grid system and boundary condition are shown on Figure IV.40. The number of computational parcels at the end of the calculations was about 400 and 900. More parcels have been tried with no significant effect on the calculation results. Due to the numerical reasons, the initial turbulent quantities were assumed to be small values ($k = 0.2m^2/s^2$ and $\epsilon = 1.0m^2/s^3$). The upstream boundary is treated as a solid wall, and other boundaries are treated as open boundaries. Collision model, turbulence modulation

model and PDF model are not activated in these calculations. A constant time-step size 10 μs was used and 6 droplets were injected per time-step for both evaporating and burning cases. After 4 ms of droplet injection with 400 time steps, the droplet numbers in the flow field were about 930 and 410, and the CPU time on CRAY X-MP/24 were 212 and 188 seconds for evaporating and burning sprays respectively.

The properties of liquid fuel (tridecane $C_{13}H_{28}$) are listed on Table IV.7. Where α_{350} is the droplet surface tension at 350 K. The physical properties of surface tension α, fuel vapor diffusivity multiplying by density ρD, gas-phase thermal conductivity K, and gas-phase viscosity μ are calculated using the following empirical relation as functions of temperature,

$$\alpha = \frac{T_{cr} - T_d}{T_{cr} - 350}\alpha_{350} \tag{IV.4}$$

$$\rho D = AIRDIF \cdot T_g^{EXPDIF} \tag{IV.5}$$

$$K = AIRLA1 \cdot T_g^{1.5}/(T_g + AIRLA2) \tag{IV.6}$$

$$\mu = AIRMU1 \cdot T_g^{1.5}/(T_g + AIRMU2) \tag{IV.7}$$

where T_d and T_g are droplet and gas-phase temperature respectively. The constants are listed on Table IV.7 and IV.8. The enthalpy of gas and fuel, latent heat of droplet and fuel vapor pressure as functions of temperature are taken in table from $JANAF$ data bank [116].

IV.4.1 Evaporating Solid-Cone Spray

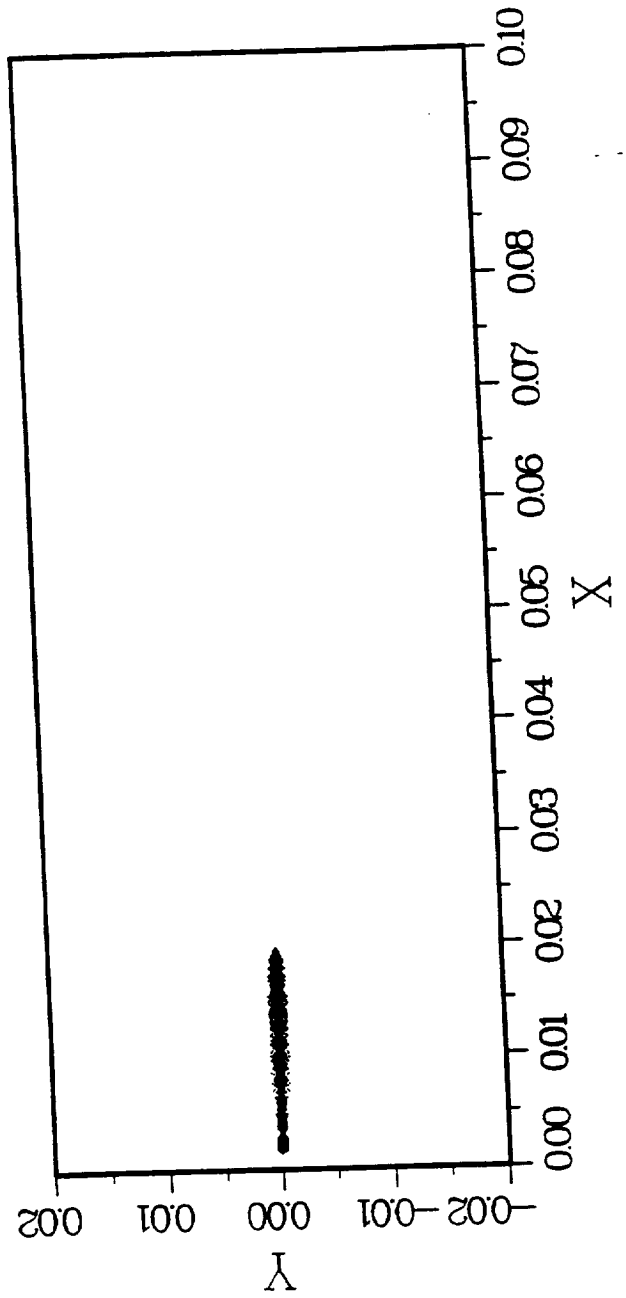

Figure IV.41: Spray parcel distribution in an evaporating spray (Time=0.2ms)

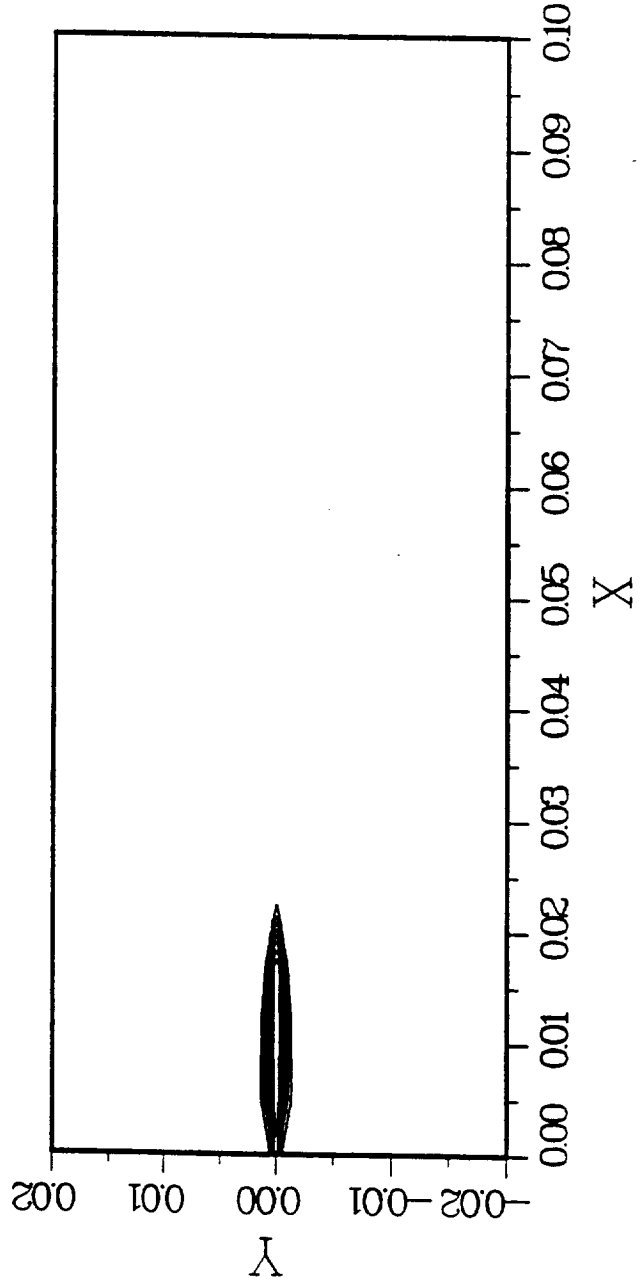

Figure IV.42: Contour of temperature in an evaporating spray (Time=0.2ms)

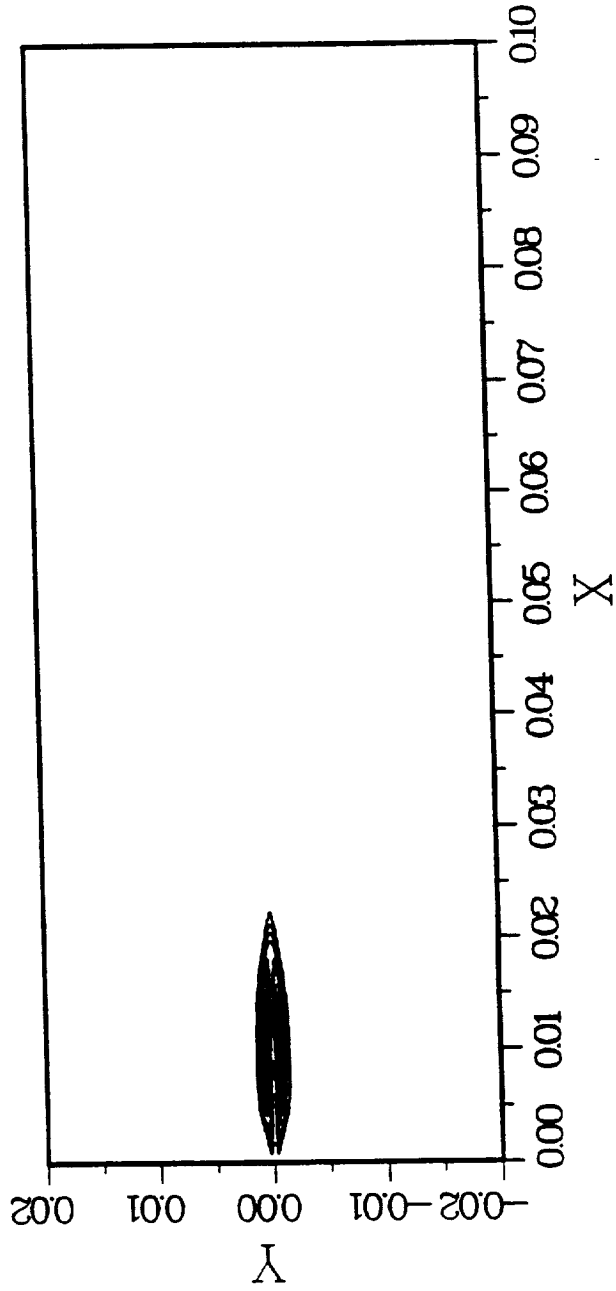

Figure IV.43: Contour of fuel mass fraction in an evaporating spray (Time=0.2ms)

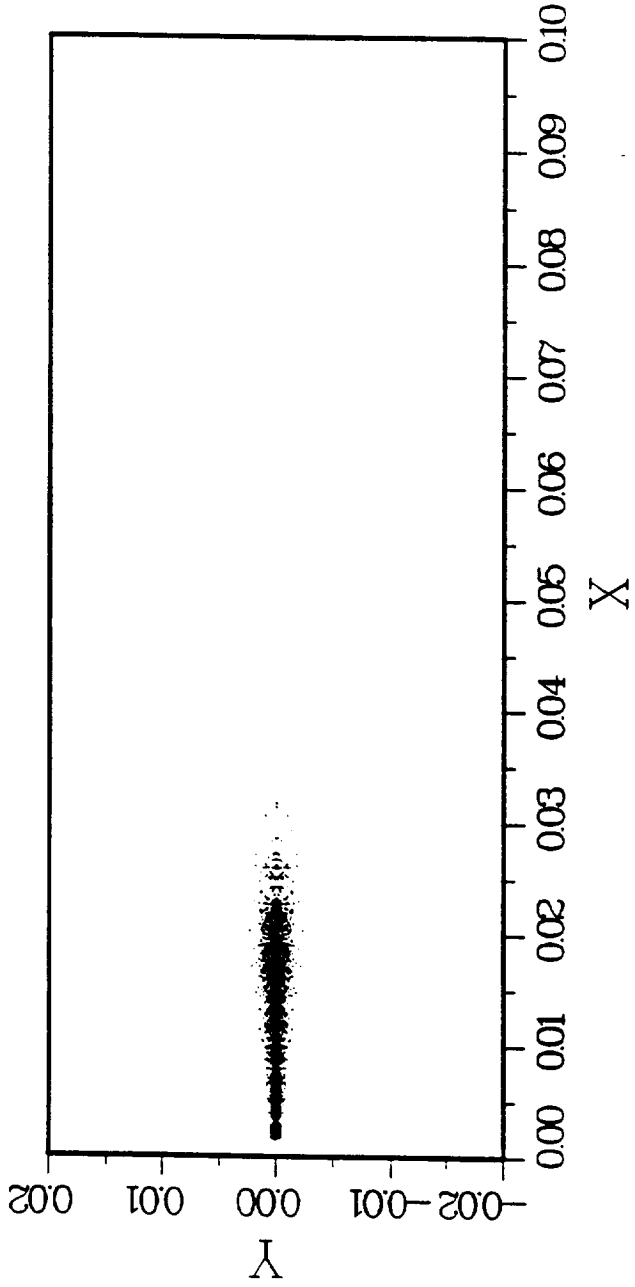

Figure IV.44: Spray parcel distribution in an evaporating spray (Time=1.0ms)

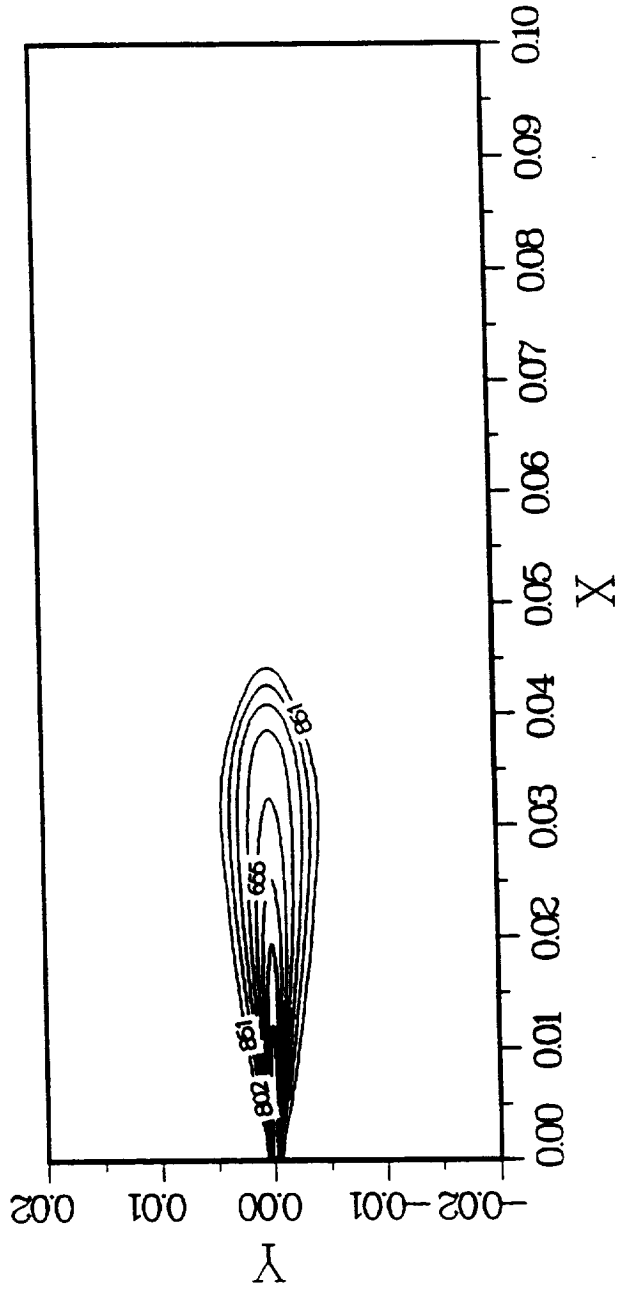

Figure IV.45: Contour of temperature in an evaporating spray (Time=1.0ms)

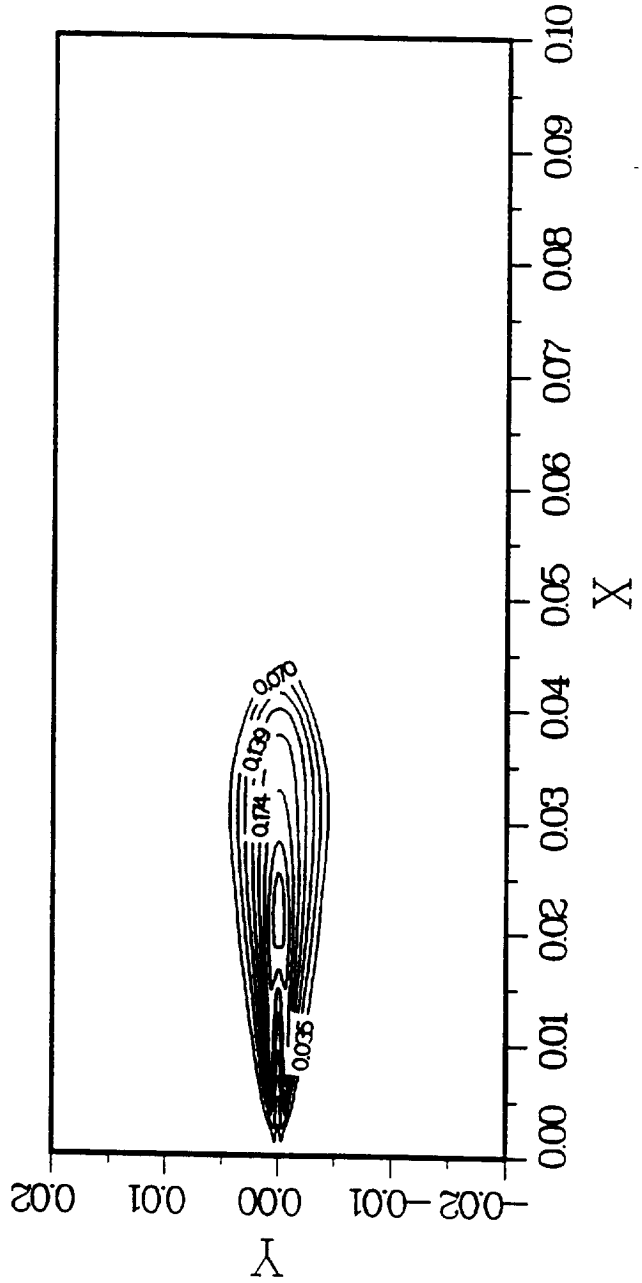

Figure IV.46: Contour of fuel mass fraction in an evaporating spray (Time=1.0ms)

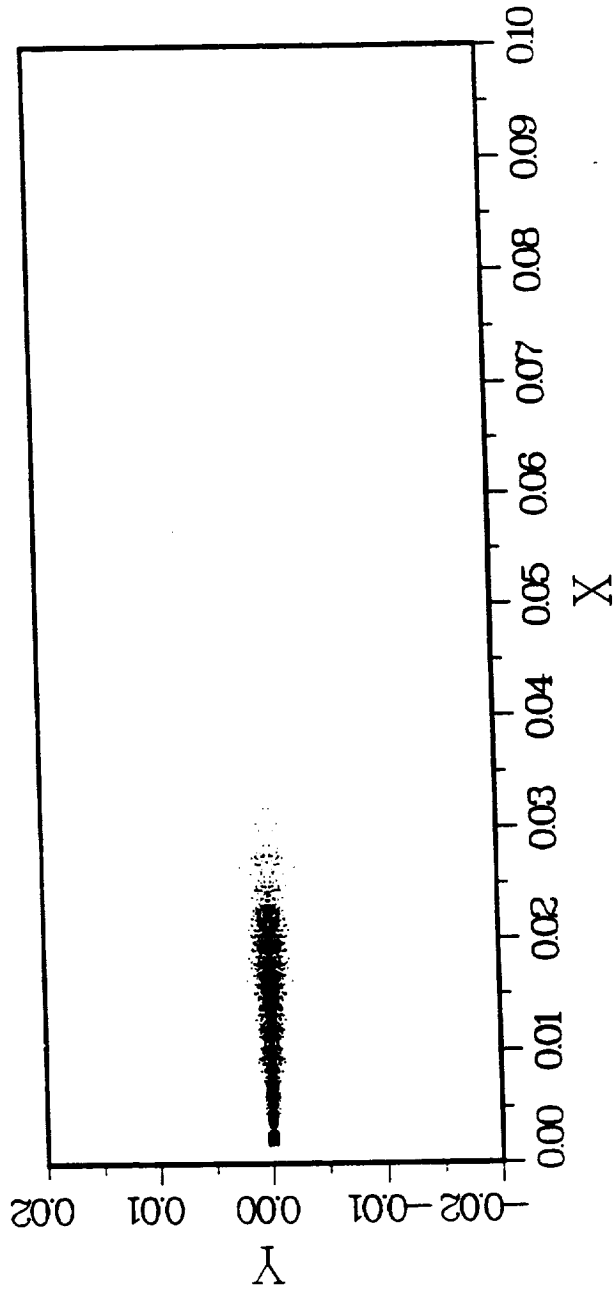

Figure IV.47: Spray parcel distribution in an evaporating spray (Time=4.0ms)

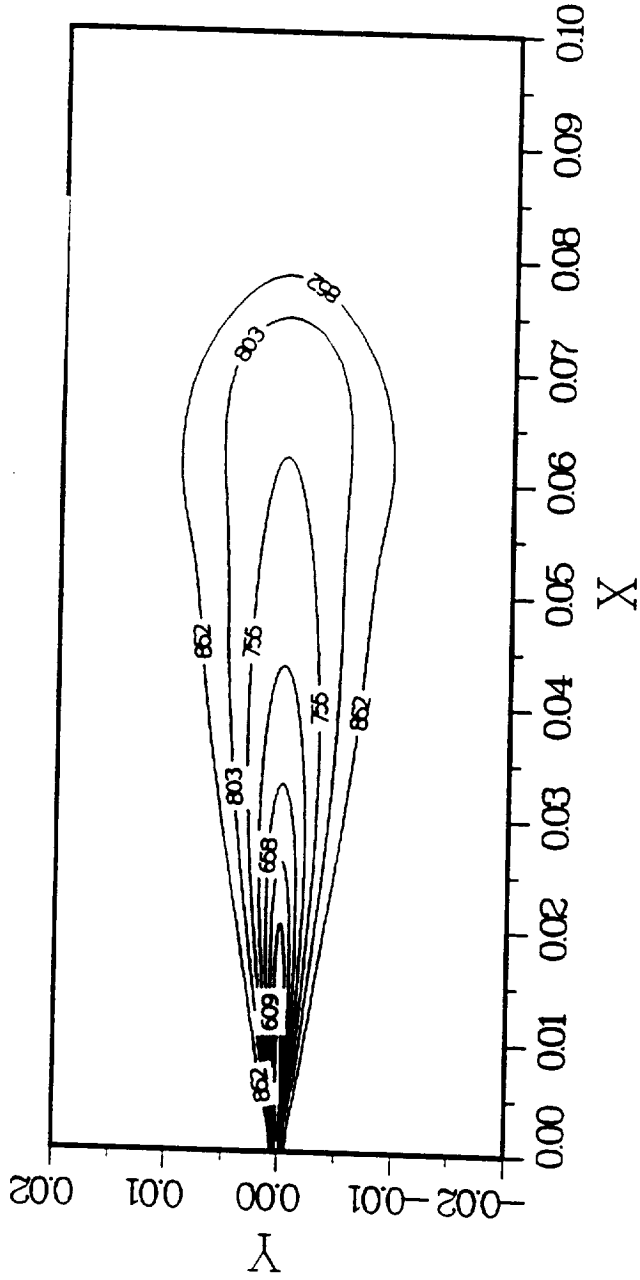

Figure IV.48: Contour of temperature in an evaporating spray (Time=4.0ms)

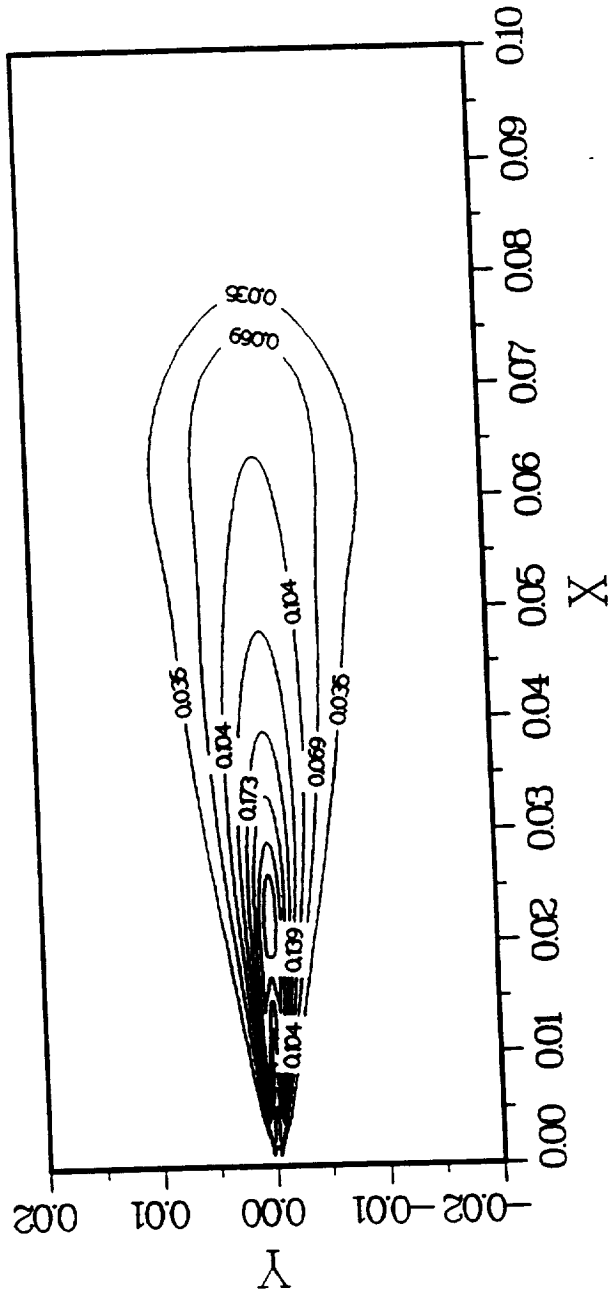

Figure IV.49: Contour of fuel mass fraction in an evaporating spray (Time=4.0ms)

Using the numerical results of the Reitz's breakup model [95], the spray parcel distribution, the contours of the fuel mass fraction, and the temperature contours for the evaporating spray are plotted in Figures IV.41, IV.42, IV.43, IV.44, IV.45, IV.46, IV.47, IV.48 and IV.48 at different times of spray development. These results show that the spray penetrations increase with respect to time at early period of injection, however the penetration become nearly constant after $t = 0.2ms$ due to evaporation. Even though the liquid drop does not penetrate more, the evaporated fuel vapor continuously penetrate with respect to time. At later period of injection, the low-temperature zone near the injector is created due to the cooling effects of evaporation. In this evaporating case, we did not turn on the collision routine because the collision process causes a significant increase of the drop size and the corresponding penetration length is unrealistically long. The discrepancy could be attributed to the inconsistency between the collision model and the vaporization model as well as the neglect of the supercritical vaporization effects. A similar spray characterization was obtained using the TAB breakup model.

Comparisons of the computed and experimental spray penetration versus time are shown in Figure IV.50. Due to the neglect of the collision process, two breakup models underpredict the penetration length. At the initial stage of the injection, the TAB model noticeably underpredicts the penetration length. The underpredicted penetration length with the TAB model results from the rapid breakup rate near the injector.

IV.4.2 Burning Solid-Cone Spray

When the experimental atmosphere changed from nitrogen to air, ignition and combustion occurred at this high temperature environment. A single-step fast chemical

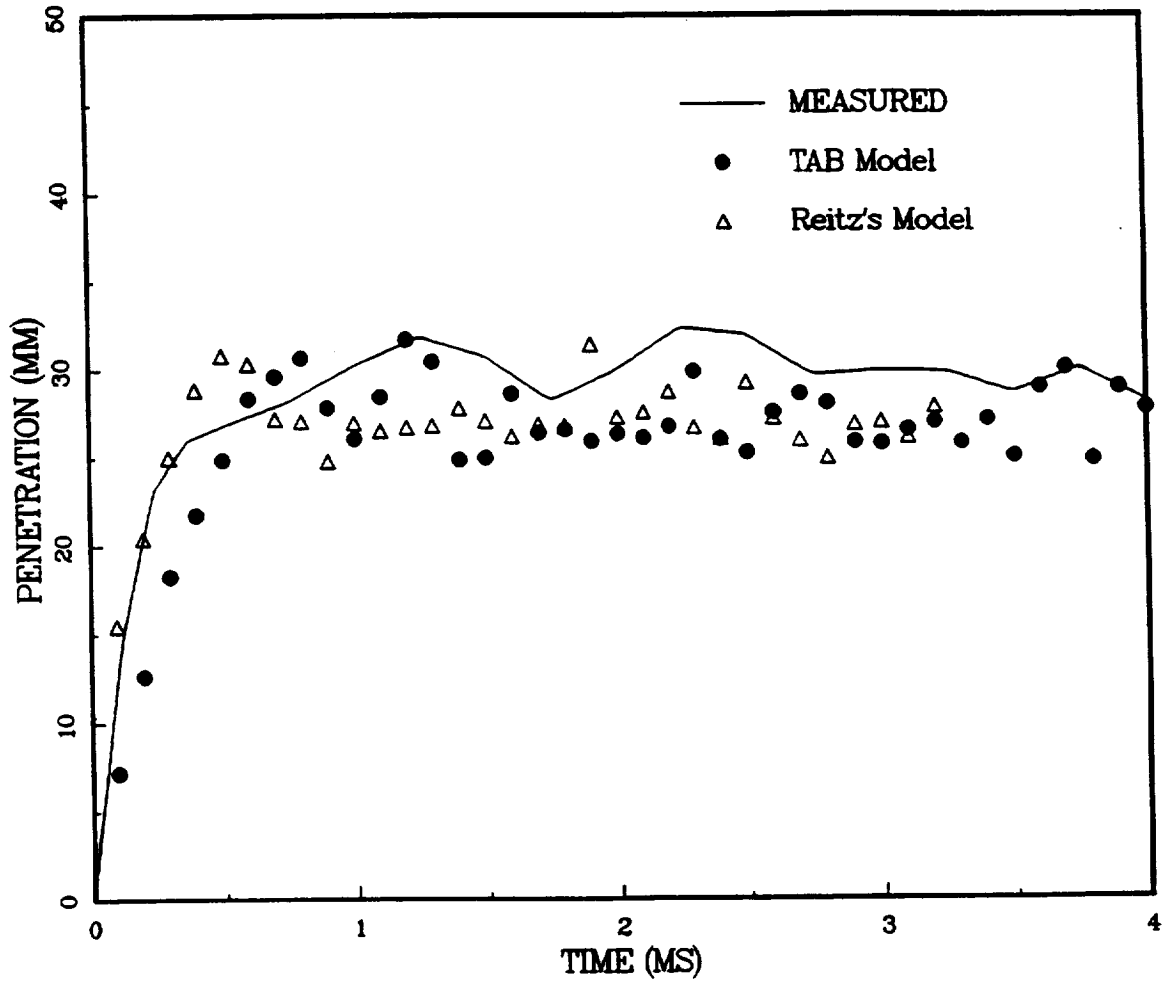

Figure IV.49: Spray tip penetration versus time in an evaporating spray.

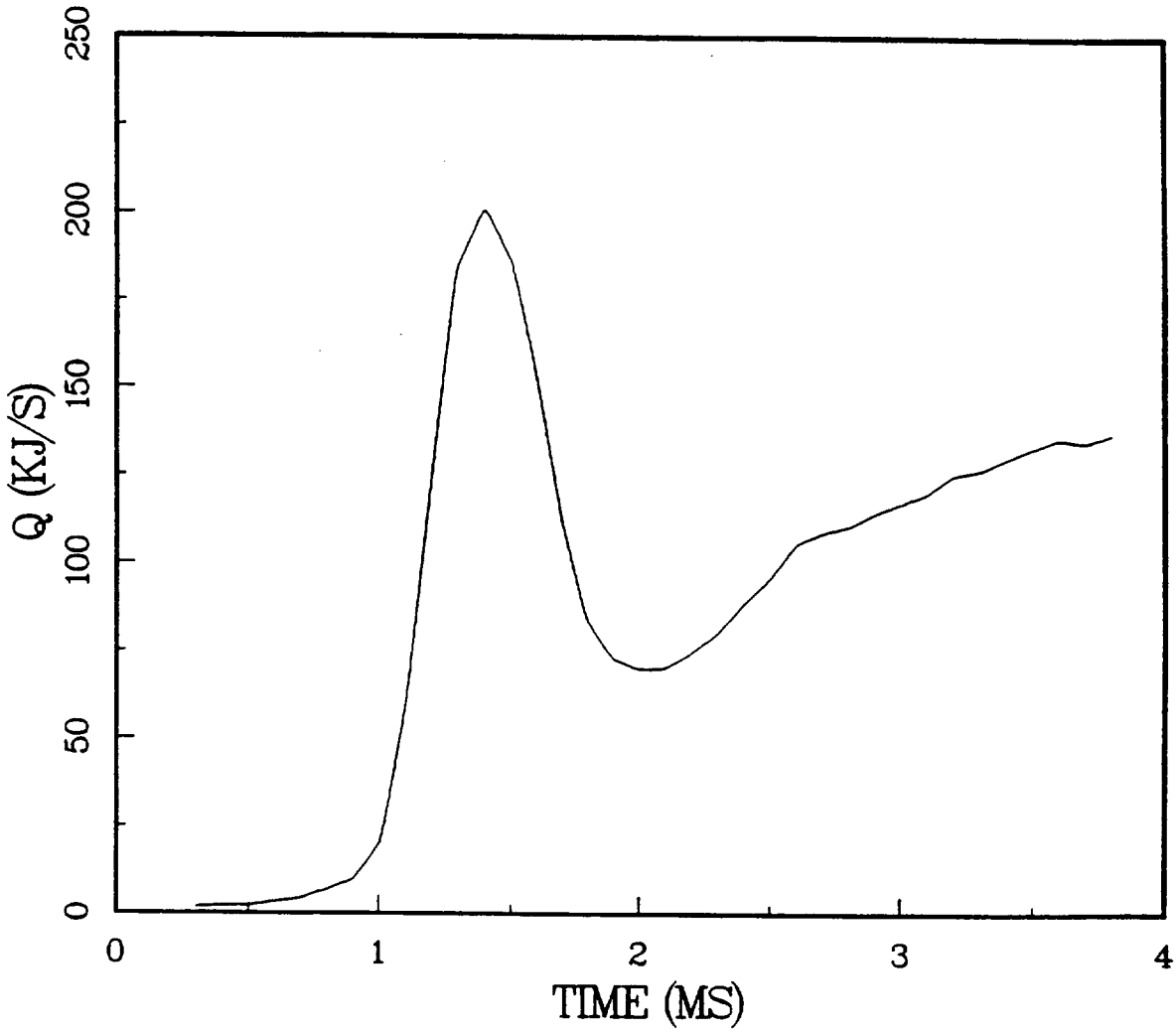

Figure IV.51: Whole net heat release rate of fuel vapor versus time.

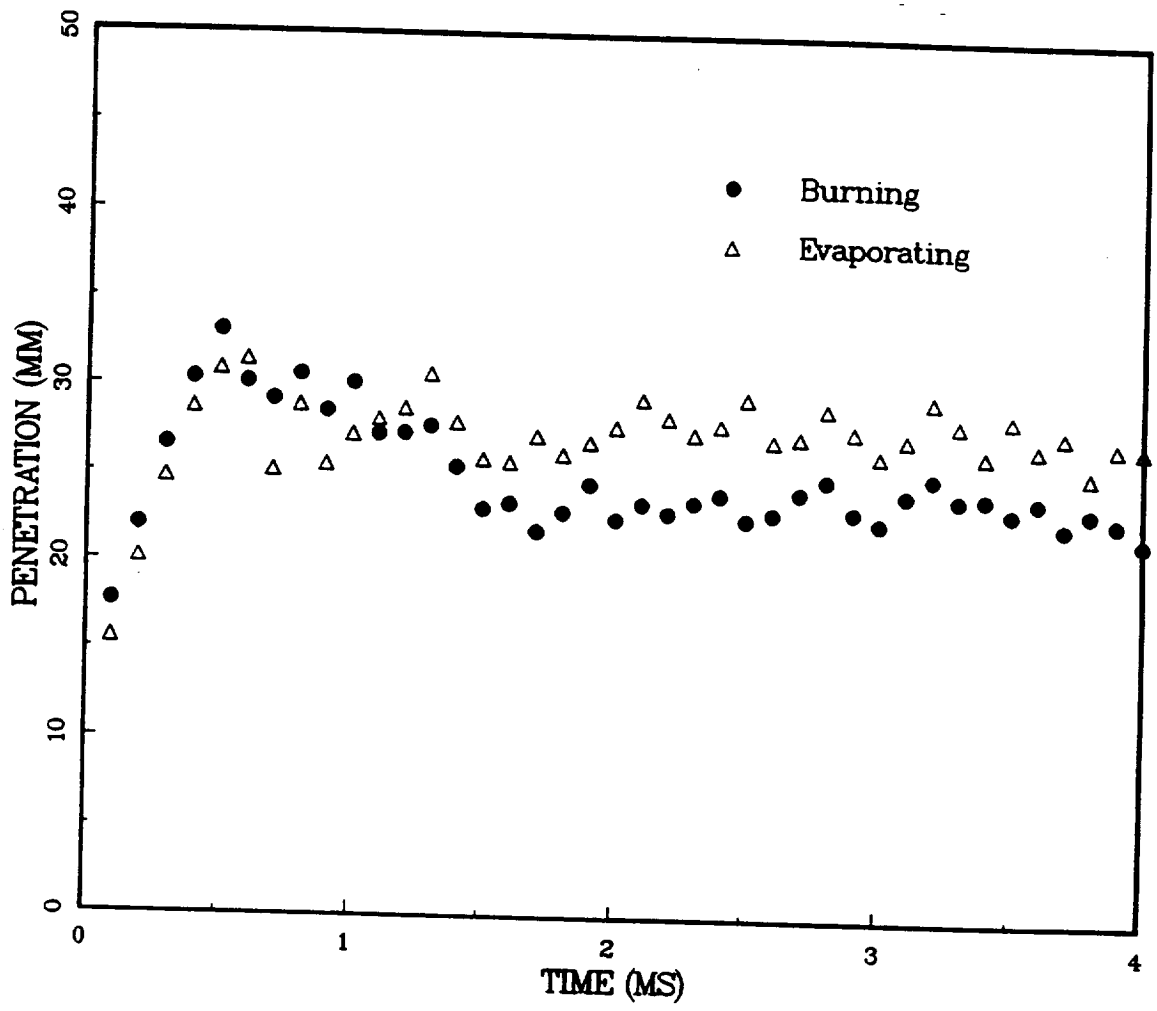

Figure IV.51: Comparison of penetration lengths for burning and evaporating sprays.

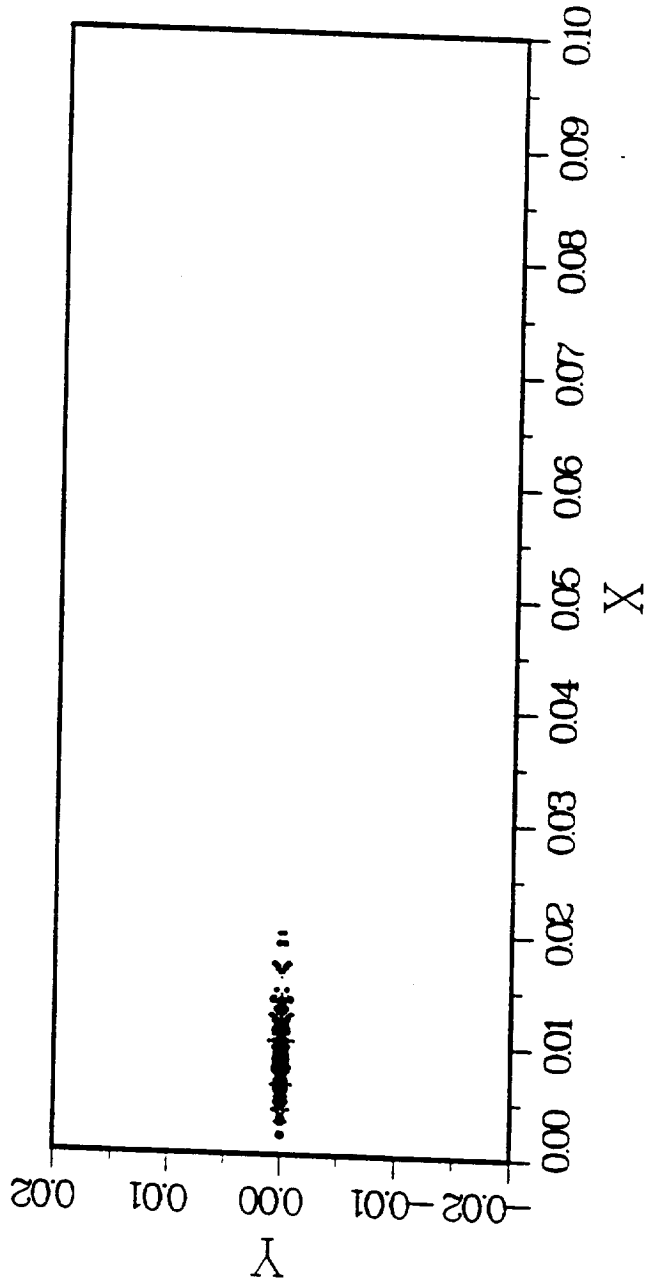

Figure IV.53: Spray parcel distribution in a burning spray (Time=1.4ms)

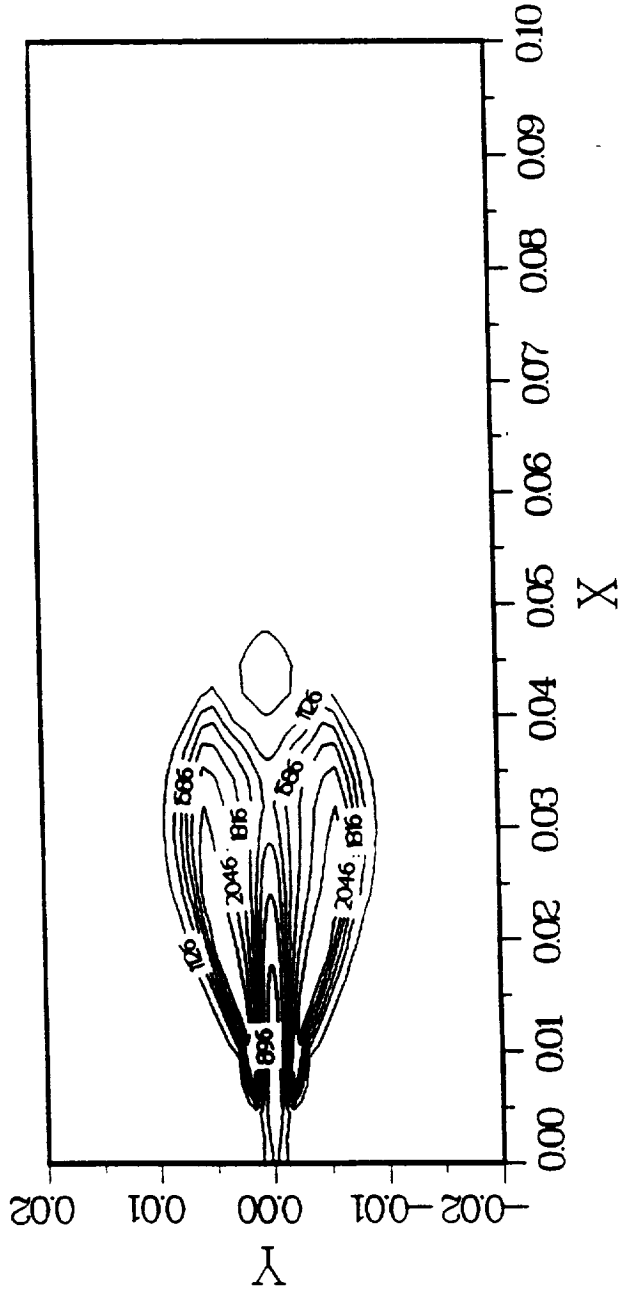

Figure IV.54: Contour of temperature in a burning spray (Time=1.4ms)

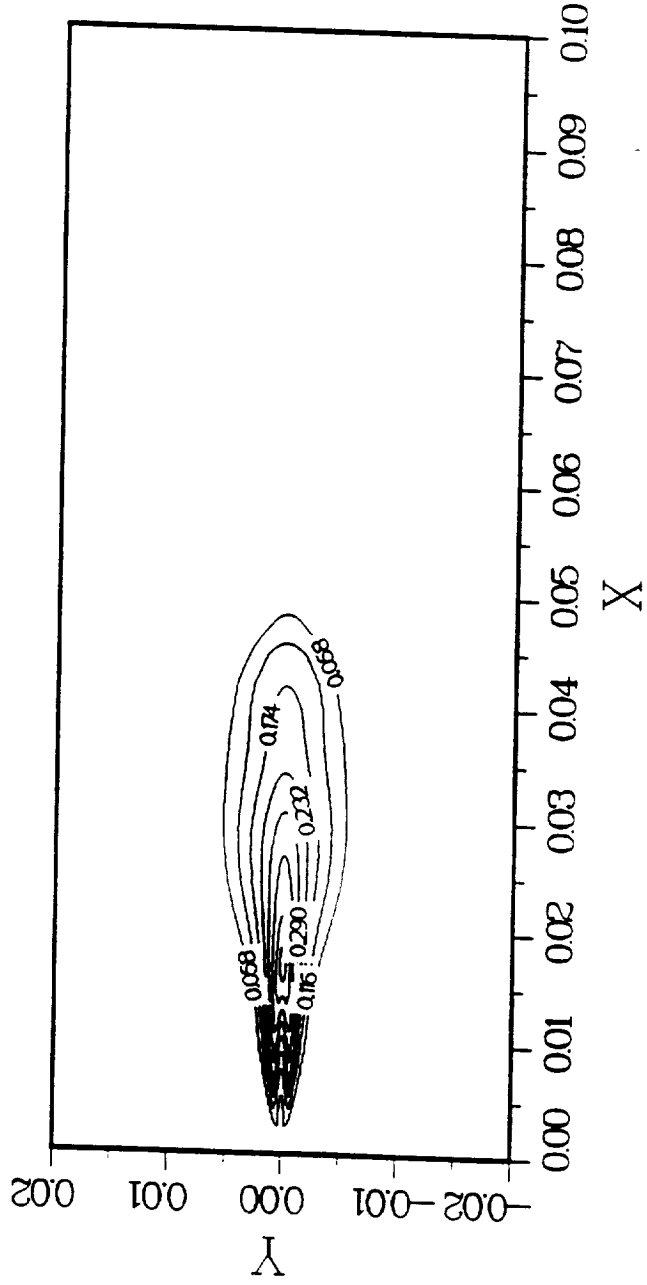

Figure IV.55: Contour of fuel mass fraction in a burning spray (Time=1.4ms)

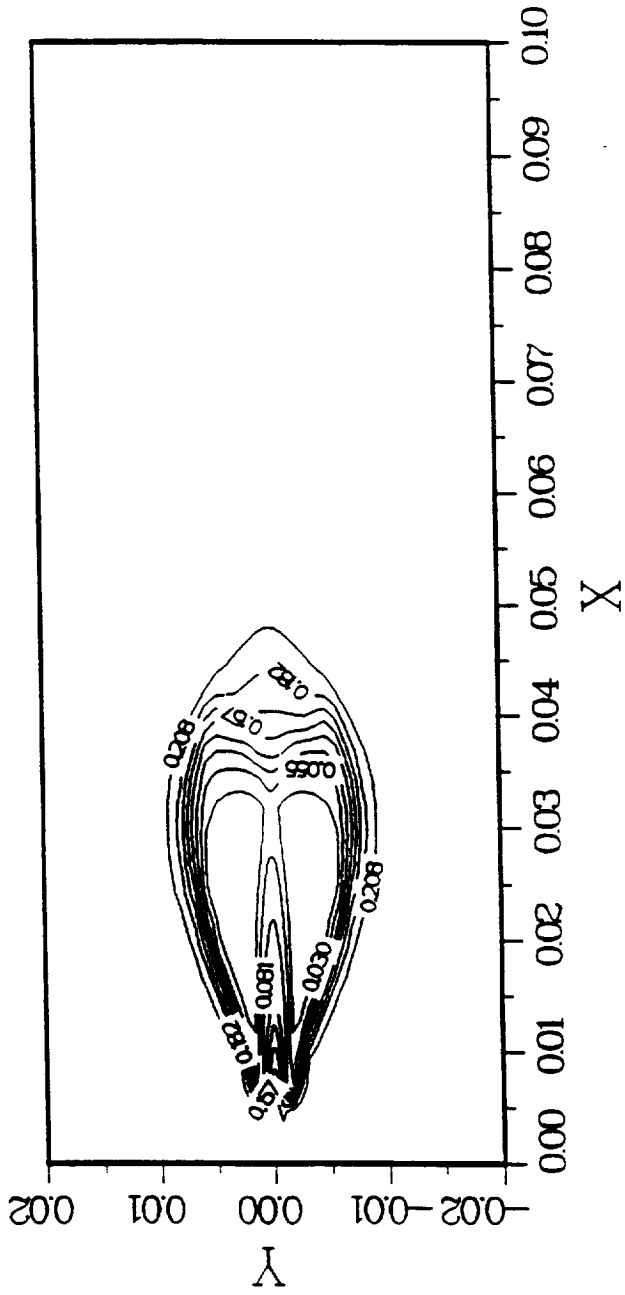

Figure IV.56: Contour of oxygen mass fraction in a burning spray (Time=1.4ms)

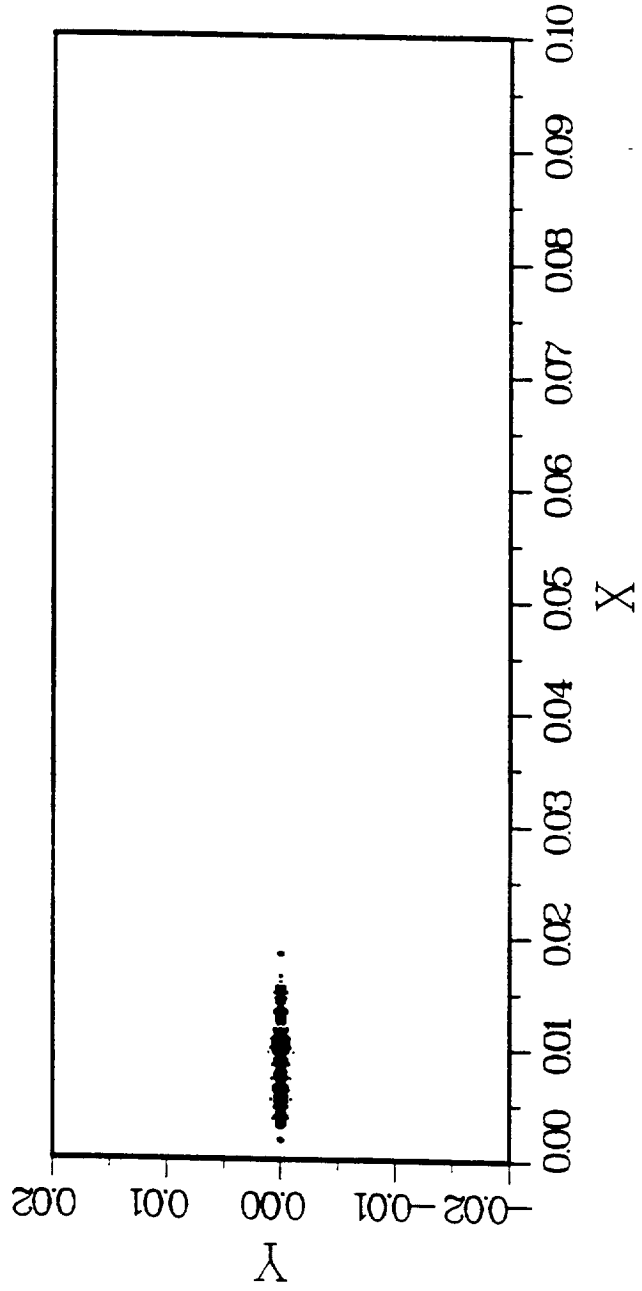

Figure IV.57: Spray parcel distribution in a burning spray (Time=2.6ms)

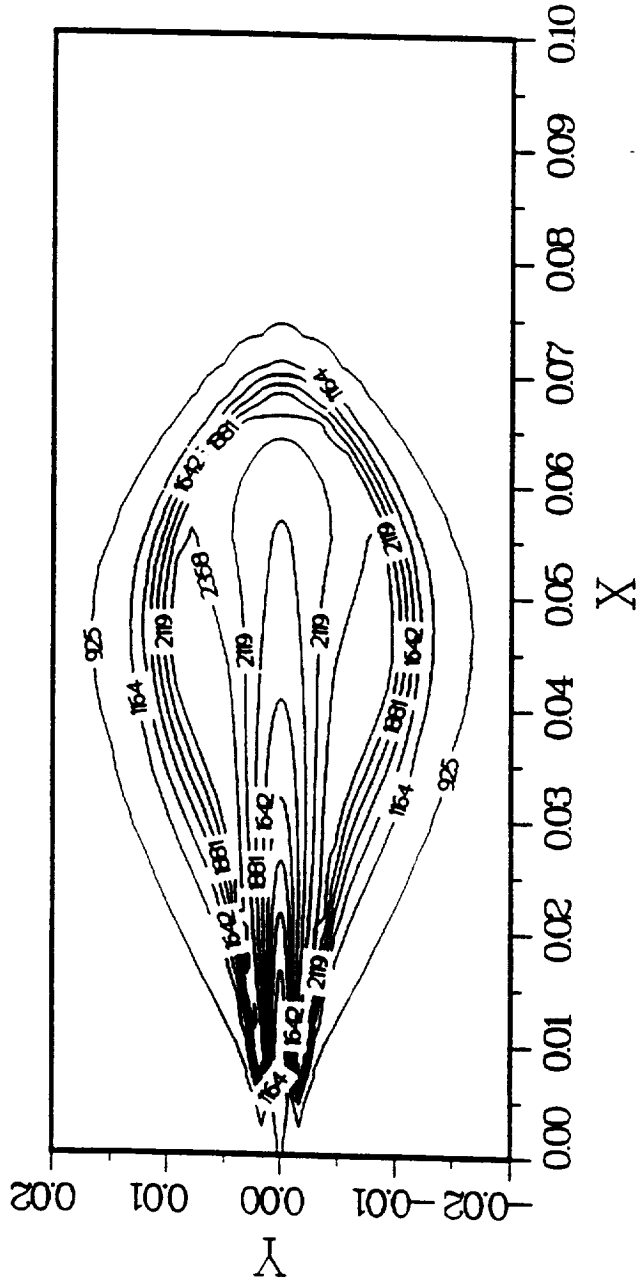

Figure IV.58: Contour of temperature in a burning spray (Time=2.6ms)

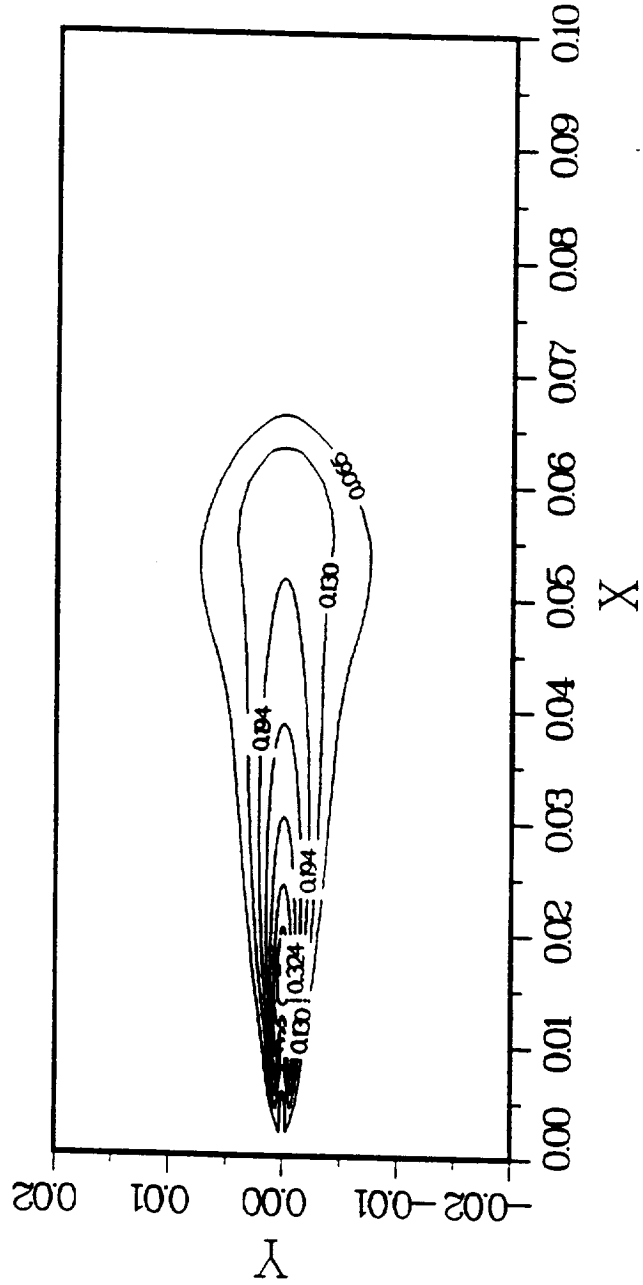

Figure IV.59: Contour of fuel mass fraction in a burning spray (Time=2.6ms)

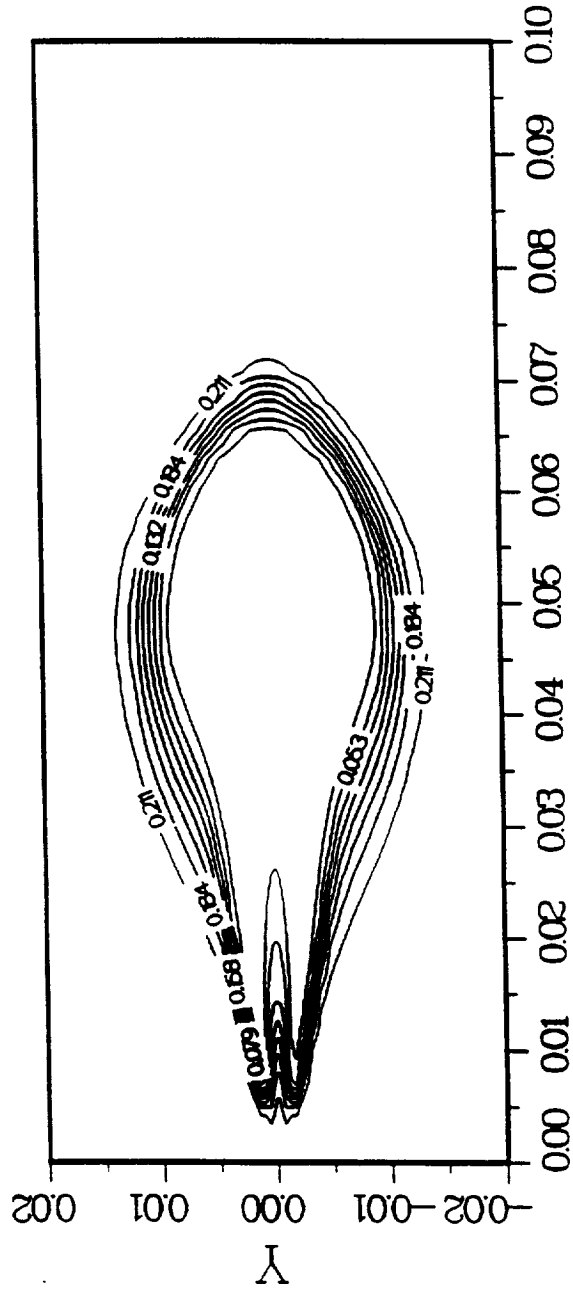

Figure IV.60: Contour of oxygen mass fraction in a burning spray (Time=2.6ms)

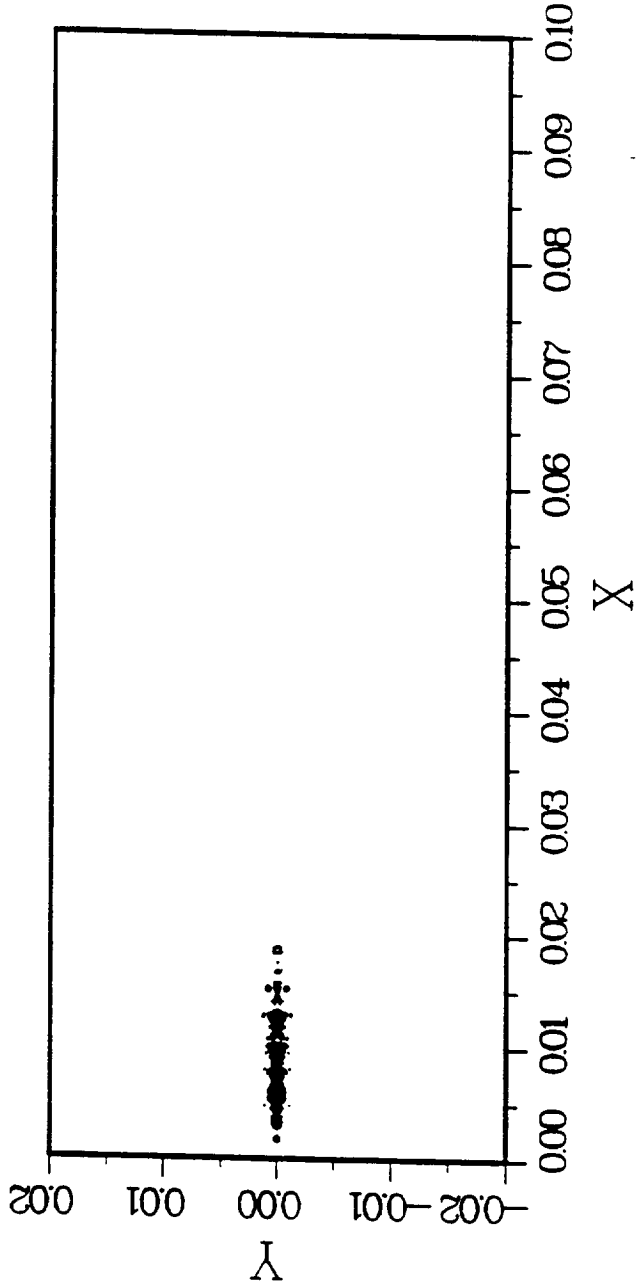

Figure IV.61: Spray parcel distribution in a burning spray (Time=3.8ms)

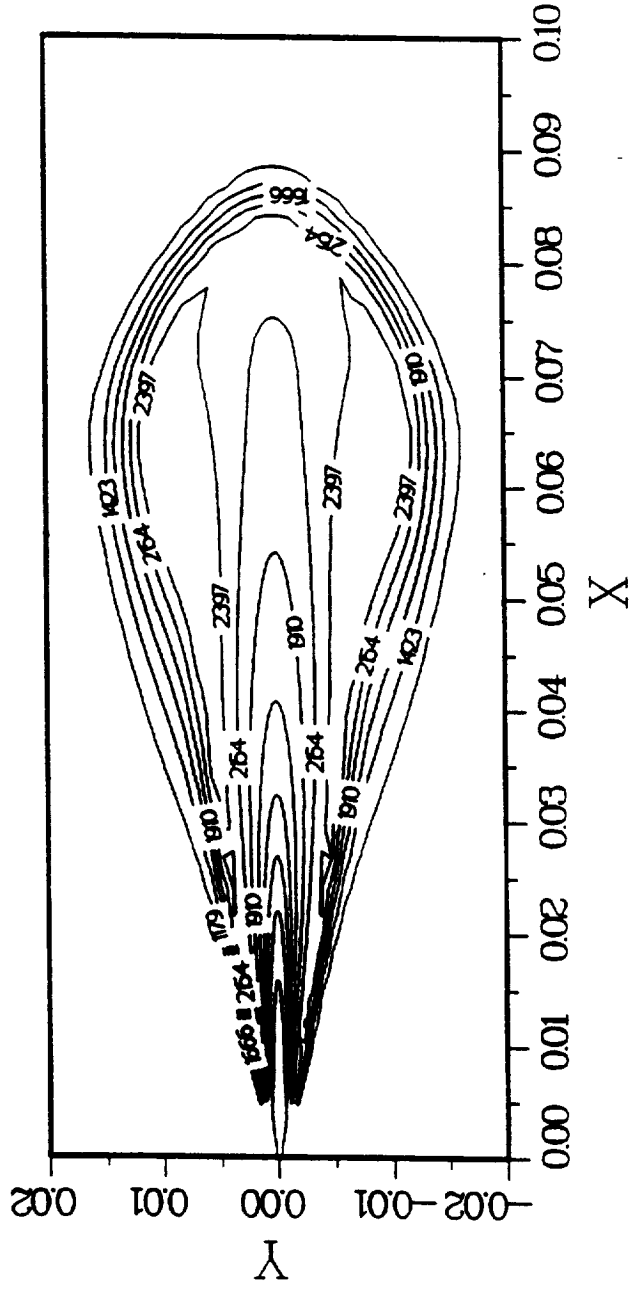

Figure IV.62: Contour of temperature in a burning spray (Time=3.8ms)

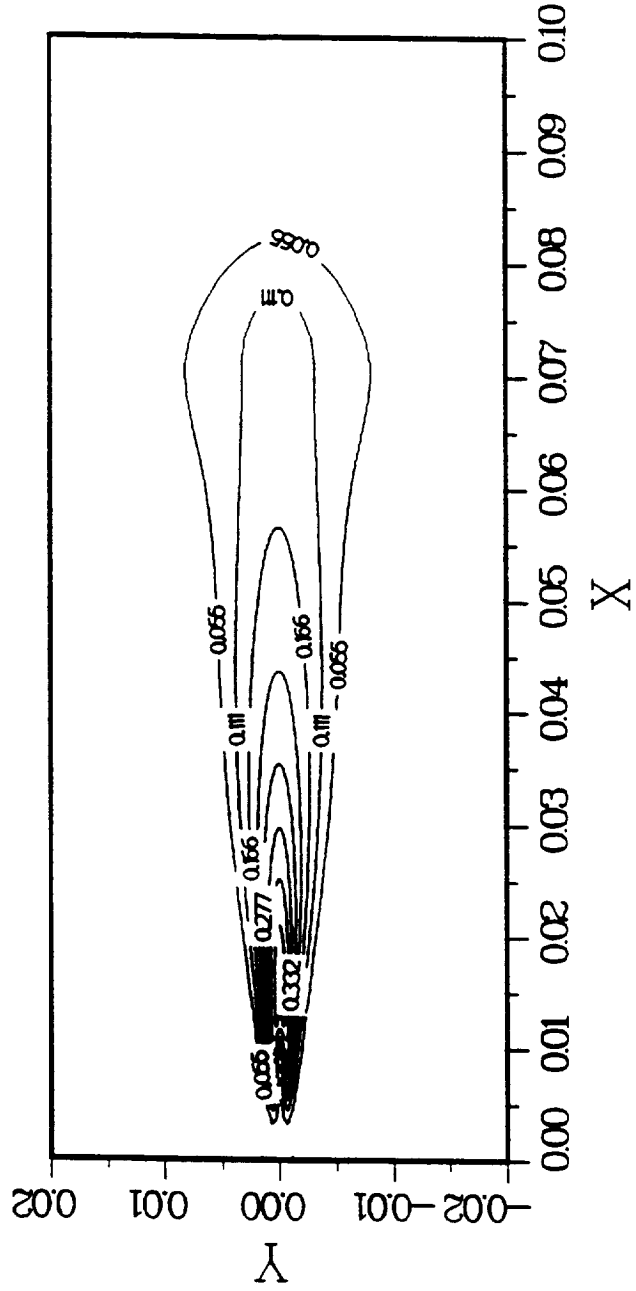

Figure IV.63: Contour of fuel mass fraction in a burning spray (Time=3.8ms)

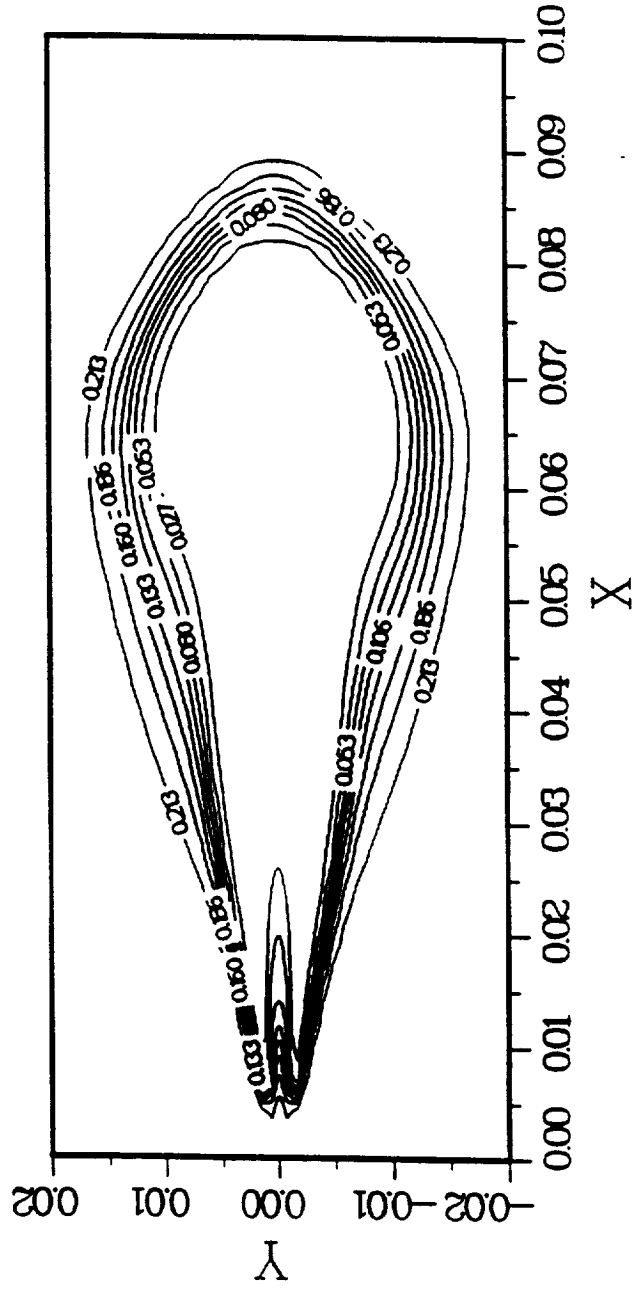

Figure IV.64: Contour of oxygen mass fraction in a burning spray (Time=3.8ms)

reaction and eddy breakup model mentioned in Section (II.2.4) is employed here. The reaction for tridecane can be expressed as:

$$C_{13}H_{28} + 20O_2 = 13CO_2 + 14H_2O \tag{IV.8}$$

The chemically controlled reaction rate for the fuel, given by the usual Arrhenius formula [119], can be written as following after units changed from cm-mole to m-kg system,

$$R_{che} = A(W_f \cdot 1000)(\frac{\rho Y_f}{W_f \cdot 1000})^a(\frac{\rho Y_{O2}}{W_{O2} \cdot 1000})^b exp(-\frac{E}{RT}) \tag{IV.9}$$

where the units of R_{che} is $kg/(m^3 \cdot s)$, ρ is kg/m^3, E/R is Kelvin and molecular weight is $kg/kmol$. The constants used above are listed on Table IV.9. Due to the conservation of atoms, only two mass fractions need to be solved. Fuel and oxygen mass fractions are chosen as dependent variables and the remaining ones are determined from the stoichiometric relations in Section (II.2.4). The stoichiometric constant s is calculated as:

$$s = 20\frac{W_{O2}}{W_f} = 3.48 \tag{IV.10}$$

Table IV.9: Constants in Arrhenius law

W_f	184 $kg/kmol$	A	3.2×10^{11}	a	0.25
W_{O2}	32 $kg/kmol$	E/R	15,100 K	b	1.50

When liquid fuel jet is injected from nozzle, a spray is produced and droplets evaporate resulting fuel vapor accumulated. Ignition is accompanied following rich

vapor environment and high-temperature. The net heat release rate of fuel vapor in whole flow field is calculated and shown in Figure IV.51. Before time=1.0 ms, the net heat release rate is very low and that means no combustion occurs. It increases dramatically after time=1.0 ms and reaches its maximum value which is much lager than the fuel supply rate. This should be attributed to the accumulated fuel vapor reacting with oxygen rapidly after the occurrence of ignition. The predicted ignition time 1.0 ms is in good agreement with the experimental results observed from the Schlieren photographs. The net heat release rate decreases from t=1.3 ms to 2.0 ms, that means accumulated vapor consumes a lot due to the rapid spreading of combustion wave. The increase of the net heat release rate after reaching its minimum value can be explained to the enhanced droplet evaporation rate by higher ambient temperature after the combustion.

Figure IV.52 compares the penetration lengths of evaporating and burning sprays. Before time=1.0 ms of ignition occurring, both penetration lengths are almost the same because the gas properties of nitrogen and air are quite similar. The burning spray penetration length decreases after of ignition due to the higher ambient temperature promotes droplet evaporation rate. Both lengths keep almost uniform values after certain times, that means quasi-steady states are reached for liquid sprays even though the fuel vapors and temperatures still penetrate with respect to time.

Figures IV.53, IV.54, IV.55, IV.56, IV.57, IV.58, IV.59, IV.60, IV.61, IV.62, IV.63 and IV.64 show the spray parcel distribution, the contours of fuel mass fraction, temperature and oxygen mass fraction at different times of injection for burning sprays. These figures clearly illustrate the relative locations of the cold core region,

reaction zone and spray boundary of a coaxial spray diffusion flame, and their development with time progressing. The liquid jet leaving the injector fully breakups very quickly and the spray is highly nonuniform with small droplet evaporating up after a short distance from the injector due to high temperature environment. Near the injector exit, the two-phase slip velocity is the greatest and the momentum of the spray is transferred to the gas over an extended axial distance. The small droplets around the periphery of the spray exchange the momentum with the gas and cause the spray jet to entrain surrounding gas, which also providing oxidizer for fuel vapor combustion. At the same time, the small droplets evaporate rapidly to provide fuel vapor which is consumed near the outer portion of the turbulent diffusion flame. The computed configuration of a spray flame has the overall agreement with the experimental observations. The comparisons of the predicted flame front movement with time for this transient spray combustion flow also show reasonable agreement with the experimental Schlieren photographs.

In the experimental study, a considerable level of soot was observed near the spray tip where the equivalence ratio is low and the temperature is high due to the progressed turbulent mixing. Therefore, the soot model should be incorporated to improve the prediction capability of the present burning dense spray model. Future studies may include the detailed comparison with the local properties available in the experiment.

V

Conclusions and Recommendations

V.1 Summary

An efficient numerical model has been developed and the related sub-physical models also have been incorporated for calculating transient two-phase combustion flows. The gas-phase equations are written in an Eulerian coordinate and solved using a control-volume based finite-difference method on an unsteady fashion. Spatial differences are formed on a curvilinear general coordinate with all gas phase variables stored at the same grid point. Second order accurate central differencing scheme is used for the diffusion terms and second order upwind scheme is used for the convection terms. Whereas, the liquid-phase is presented in Lagrangian coordinates. This hybrid algorithm has flexibilities in handing poly-dispersed sprays in combustion devices and assigning individual particle properties. The two-way coupling between the two phases is described by the interaction source terms which represent the rates of momentum, mass and heat exchange. A strongly coupling numerical procedure based on $PISO$ algorithm with predictor/multi-corrector stages is developed and implemented into a computer code for multiphase all-speed transient flows in complex geometries ($MAST$).

A two-equation $k-\epsilon$ turbulence model is used to characterize the gas phase mean and fluctuating flow properties. The particle turbulent modulation effect to gas phase is modeled within the stochastic framework. Several modulation models are tested and the numerical results are compared with available experimental data. Particle motion equation is the simplified B-B-O equation and solved in Lagrangian coordinates for the present separated flow models. Particle dispersion by turbulent fluctuations is modelled by allowing particles to interact with a succession of eddies using a random-walk or Monte Carlo method. Parcel PDF model is used to improve computational efficiency. Poly-disperse is achieved by using size distribution function through Monte Carlo simulation or generated by breakup model. Droplet evaporation and heat transfer are calculated using Frossling correlation and Ranz-Marshall correlation respectively. Accurate calculation of mass and heat transfer is achieved by automatic reductions in the timestep when the exchange rate becomes large. The variable thermophysical properties are obtained from $JANAF$ data bank. A turbulent diffusion flame and single step chemical reaction model is used for spray combustion. Dense spray effects are accounted for by a droplet breakup and collision model. Two breakup models including a Taylor analogy breakup (TAB) model and a wave instability model are incorporated and compared. The incorporated collision model stochastically calculates the outcome of every collision, either coalescence or grazing collision.

Several particle dispersions in homogeneous and nearly-homogeneous turbulent flows are studied to calibrate the stochastic method for particle-turbulence interactions, and to evaluate the present parcel PDF model. The computations were performed for the solid particle dispersion in nearly-homogeneous turbulence and a

particle laden round jet in inhomogeneous turbulence. To account for dense spray effects, droplet breakup and collision models were employed for non-evaporating transient and steady sprays. Turbulence modulation effect was tested at a steady solid-cone spray. A transient hollow-cone spray showed complicated two-phase interactions. Finally, transient evaporating and burning sprays incorporating droplet evaporation and eddy-breakup combustion models demonstrated the sophisticated structures of such polydispersed sprays.

All the calculations were performed on a CRAY X-MP/24 supercomputer.

V.2 Conclusions

The numerical models have been developed and tested for the analysis of dilute and dense spray-combustion flows. The major conclusions of the present numerical studies are as follows:

1. A non-iterative numerical technique for computing time-dependent spray combustion flows has been developed and incorporated with existing sophisticated sub-physical models. The method is a fully interacting combination of Eulerian fluid and Lagrangian particle calculations. The interaction calculations between the two phases are formulated on a pressure-velocity coupling procedure based on the operator-splitting technique. This procedure eliminates the global iterations required in conventional PSIC procedure and, hence, is efficient for transient calculations.

2. A new set of constants for eddy life time and length scale have been evaluated. Comparing with dilute nearly-homogeneous particle turbulent dispersion experimental data, the present particle dispersion calculation

procedure has the flexibility of taking into account both of the gravity effect and the non-Stokesian drag law and gives more satisfactory result.

3. For non-evaporating, evaporating, and burning dense spray cases, the predictions show a reasonably good agreement with available experimental results in terms of spray penetration, drop sizes, and overall configuration of a burning-spray flame. However, quantitative differences exist especially at near nozzle exit locations. The discrepancies observed in the results are attributed mainly to uncertainties in the initial spray particle size and velocity distributions, the single-step fast chemistry employed by the combustion model, and the deficiencies of the $k-\epsilon$ turbulence model dealing with the dense and combustion sprays.

4. Three turbulence modulation models are evaluated and compared with standard $k-\epsilon$ turbulence model and dense spray experimental data. The analysis indicates that the direct contribution of particles to gas phase turbulence properties is important for this dense spray case. This effect is attributed to the slip velocities between two phases at the fluctuation level. The addition of particles in the two-phase flows damps the turbulence intensities of the gas phase. Favorable agreement with experimental data is achieved when modulation effect is included properly. Predictions based on the model of Mostafa and Mongia [83] have a best agreement with the measurements of Wu et al. [120] .

5. The present implementation of the parcel PDF model has successfully demonstrated the capability of accurately representing dispersion in nearly-homogeneous and inhomogeneous turbulent flows with improved efficiency

over the delta function SSF model. The numerical results also indicate that the present parcel PDF model has the capability of accurately representing drop dispersion in dense spray situations with manageable number of computational parcels.

V.3 Recommendations

The present study has presented a comprehensive numerical model for spray combustion flows. There is, however, a wide scope for further improvements in both numerical aspects and physical models for spray combustion processes should be further investigated due to their complicated physical phenomena. The following recommendations are intended as suggestions for improvements and extensions of the present spray combustion modelling.

1. Development of strong interphase coupling procedure by combining multiple pressure correction procedure and Volume of Fluid (VOF) method. The present study does not include the effect due to the volume occupied by the particle phase which perhaps plays an important role in the atomization region. In liquid rocket engine case, the atomization process takes place over an extended region within the combustion chamber and sub-scale numerical models are needed to simulate this process.

2. The droplet evaporation calculation procedure following KIVA-II [4] is used in this study. Droplets located in the same control volume are evaporating one by one and see different intermediate gas temperature and vapor mass fraction. In high evaporating case, both gas temperature and vapor mass fraction change a lot in the calculation time step, that will

result in different evaporation history for each droplet even with same physical properties just due to different calculation sequences. This numerical procedure induced difference needs to be avoided through more precise numerical consideration.

3. Incorporations of equilibrium and finite rate chemistry packages for efficient transient reacting flow calculations. The strong coupling between the flow fields and chemical reactions makes large variations in gas density, temperature and velocity etc.. More comprehensive operator-splitting techniques are required to accurately and efficiently predict reacting flows, especially for fast transient ones involving complex and stiff chemical kinetics.

4. More studies on turbulence modulation effect by particles, non-isotropic turbulence model such as the algebraic stress model and the second-moment closures for two-phase combustion flows are desirable.

5. The present evaporation model does not include the supecritical temperature and pressure effect. In fact, this effect would be a major contributor to spray combustion dynamics in liquid rockets engines such as the space shuttle main engines (SSME) and advanced gas turbine combustors etc.. Droplets exposed to sufficiently high temperatures under supercritical pressures may be heated to the critical state or be gasified upon reaching critical point. Such mechanisms require extensive experimental inputs and the related researches are currently underway. At the same time, the present model does not take into account the group effect for droplet evaporation/combustion. In the group combustion model of Chiu et al.

[26], four combustion modes may occur for a droplet cloud. Bellan et al. [13] also proposed a group evaporation model to account for the dense spray effect. How to define the group parameters based on the spray dynamics and to incorporate these models into CFD code are receiving more researching attentions [54].

Appendix A

Particle Turbulent Dispersion From a Circle

$$P(x,y) = \{\frac{1}{2\pi\sigma^2}\oint exp(-[(x-x_0)^2+(y-y_0)^2]/(2\sigma^2)\ ds\}/\oint ds$$

$$= \{\frac{1}{2\pi\sigma^2}\oint exp(-[(x-x_0)^2+(y-y_0)^2]/(2\sigma^2)\ ds\}/(2\pi r_0) \quad \text{(A.1)}$$

Let's change to cylindrical coordinate,

$$\begin{aligned} x_0 &= r_0 cos\alpha \\ y_0 &= r_0 sin\alpha \\ ds &= r_0 d\alpha \\ x &= r cos\theta \\ y &= r sin\theta \end{aligned} \quad \text{(A.2)}$$

Substituting above relations into equation A.1 yields

$$P(r,\theta) = \frac{1}{(2\pi\sigma)^2}\int_0^{2\pi} exp\{-[r^2+r_0^2-2rr_0cos(\alpha-\theta)]/(2\sigma^2)\}d\alpha$$

$$= \frac{exp[-(r^2+r_0^2)/(2\sigma^2)]}{(2\pi\sigma)^2}\int_0^{2\pi} exp[rr_0cos(\alpha-\theta)/(2\sigma^2)]d\alpha \quad \text{(A.3)}$$

Substituting $\beta = \alpha - \theta$ into equation A.3 yields

$$P(r,\theta) = \frac{exp[-(r^2+r_0^2)/(2\sigma^2)]}{(2\pi\sigma)^2}\int_{-\theta}^{2\pi-\theta} exp(rr_0cos\beta/\sigma^2)d\beta \qquad (A.4)$$

From residual theory of complex integration theory, we obtain

$$\int_{-\theta}^{2\pi-\theta} exp(rr_0cos\beta/\sigma^2)d\beta = 2\pi i \oint_{|z|=1} exp[rr_0(z+1/z)/(2\sigma^2)]\frac{dz}{iz}$$

$$= 2\pi \oint_{|z|=1} [1 + \frac{\frac{rr_0z}{2\sigma^2}}{1!} + \cdots + \frac{(\frac{rr_0z}{2\sigma^2})^n}{n!} + \cdots] \cdot [1 + \frac{\frac{rr_0}{2\sigma^2z}}{1!} + \cdots + \frac{(\frac{rr_0}{2\sigma^2z})^n}{n!} + \cdots] \cdot \frac{dz}{z}$$

$$= 2\pi \sum_{n=0}^{\infty} [\frac{(\frac{rr_0}{2\sigma^2})^n}{n!}]^2 \qquad (A.5)$$

Hence, we obtain probability density function of particle position distribution for its turbulent dispersion from a circle with radius r_0,

$$P(r,\theta) = \frac{exp[-(r^2+r_0^2)/(2\sigma^2)]}{2\pi\sigma^2}\sum_{n=0}^{\infty}[\frac{(\frac{rr_0}{2\sigma^2})^n}{n!}]^2 \qquad (A.6)$$

Note, this function is inependent of θ. For particle dispersion from a point source, where $r_0 = 0$, $P(r,\theta)$ is simplified to

$$P(r,\theta) = \frac{exp[-r^2/2\sigma^2]}{(2\pi\sigma^2)} \qquad (A.7)$$

Bibliography

[1] S. K. Aggarwal. Modeling of a dilute vaporizing mlticomponent fuel spray. *International Journal of Heat and Mass Transfer*, 30:1949, 1987.

[2] M.G. Allen and R.K. Hanson. Digital imaging of species concentration fields in spray flames. 21st Symp.-(International) on Combustion, pp.1755-1762, 1986.

[3] M.G. Allen and R.K. Hanson. Planar laser-induced-fluorescence monitoring of OH in a spray flame. *Optical Engineering*, 25(12):1309, 1986.

[4] A. A. Amsden, P. J. O'Rourke, and T. D. Butler. KIVA-II: A computer program for chemically reactive flows with sprays. LA-11560-MS, 1985.

[5] D. A. Anderson, J. C. Tannehill, and R. H. Pletcher. *Computational Fluid Mechanics and Heat Transfer.* Hemisphere, Washington, D.C., 1984.

[6] M. Arai, M. Tabata, H. Hiroyasu, and M. Shimizu. Disintegrating process and spray characterization of fuel jet injected by a diesel nozzle. SAE Technical Paper 840275, 1984.

[7] J. P. Asheim and J. E. Peters. Alternative fuel spray behavior. *Journal of Propulsion and Power*, 5:391, 1989.

[8] Y. El Banhawy and J. M. Whitelaw. Calculation of the flow properties of a confined kerosene-spray flames. *AIAA Journal*, 18:1503, 1980.

[9] R. M. Beam and R. F. Warming. An implicit finite-difference algorithm for hyperbolic systems in conservation law form. *Journal of Computational Physics*, 22:87, 1976.

[10] J. Bellan and R. Cuffel. A theory of nondilute spray evaporation based upon multiple drop interactions. *Combustion and Flame*, 51:55, 1983.

[11] J. Bellan and K. Harstad. Evaluation of the importance of the relative velocity during evaporation of drops in sprays. *International Journal of Heat and Mass Transfer*, 29(4):647, 1986.

[12] J. Bellan and K. Harstad. Analysis of the convective evaporation of nondilute clusters of drops. *International Journal of Heat and Mass Transfer*, 30(1):125, 1987.

[13] J. Bellan and K. Harstad. The details of the convective evaporation of dense and dilute clusters of drops. *International Journal of Heat and Mass Transfer*, 31(8):1655, 1988.

[14] J. Bellan and K. Harstad. Turbulence effects during evaporation of drops in clusters. *International Journal of Heat and Mass Transfer*, 31(8):1655, 1988.

[15] F.V. Bracco. Modeling of engine sprays. SAE Paper 850394, 1985.

[16] K. N. C. Bray and J. B. Moss. A unified statistical model for the premixed turbulence flame. *Acta Astornaut.*, 2:291, 1977.

[17] W. R. Briley and H. McDonald. Solution of the mutidimensional compressible Navier-Stokes equations by a generalized implicit method. *Journal of Computational Physics*, 24:372, 1977.

[18] A.C. Buckingham and W.J. Siekhaus. Interaction of moderately dense particle concentrations in turbulent flow. AIAA-81-0346, 1981.

[19] S. R. Chakravarthy and S. Osher. A new class of high accuracy TVD schemes for hyperbolic conservation laws. AIAA-85-0363, 1985.

[20] A.U. Chatwani and F.V. Bracco. Computation of dense spray jets. ICLASS-85, London, 1985.

[21] C. P. Chen, H. M. Shang, and Y. Jiang. A novel gas-droplet numerical method for spray combustion. AIAA-91-0286, 29th Aerospace Science Meeting, Reno, Nevada, 1991, to be appeared in the Int. J. Numer. Meth. Fluids, 1992.

[22] C. P. Chen and P. E. Wood. Turbulence closure modeling of the dilute gas particle axisymmetric jet. *AIChE Journal*, 32:163, 1986.

[23] Y. S. Chen. Viscous flow computations using a second-order upwind differencing scheme. AIAA-88-0417, 1988.

[24] N.A. Chigier, C.P. Mao, and V. Oechsle. Structure of air-assist atomizer spray. Paper 7-6A, CSS/WSS/Combustion Institute Spring Meeting, April, 1985.

[25] H. H. Chiu. Recent advances in interfacial exchange processes in two-phase flow systems. Proceedings Symposium on Transport Phenomena and Applications, Taipei, August 1991.

[26] H. H. Chiu, H. Y. Kim, and E. J. Croke. Internal group combustion of liquid droplets. Presented at 19th Symposium (International) on Combustion /The Combustion Institute, pp.971-980, 1982.

[27] D. Choi and C. L. Merkle. Application of time-iterative schemes to incompressible flow. *AIAA Journal*, 23:1518, 1985.

[28] C. T. Crowe and M. P. Sharma. The particle source in cell method for gas-droplet flows. *Journal of Fluid Engineering*, 99:325, 1977.

[29] W.M. Connoley D. Howard and J.S. Rollett. Unsymmetric conjugate gradient methods and sparse direct methods in finite element flow simulation. *Int. J. Numerical Meth. Fluids*, 10:925–945, 1990.

[30] J. P. Van Doormaal, G. D. Raithby, and B. H. McDonald. The segregated approach to predicting viscous compressible fluid flows. *Journal of Turbomachinery*, 109:268, 1987.

[31] J. K. Dukowicz. A particle-fluid numerical model for liquid sprays. *Journal of Computational Physics*, 35:229, 1980.

[32] G. L. Hubbard et al. Droplet vaporization: Effects of transient and variable properties. *International Journal of Heat and Mass Transfer*, 18:1003, 1975.

[33] G. M. Faeth. Current status of droplet and liquid combustion. *Prog. Energy Comb. Sci.*, 3:191–224, 1977.

[34] G. M. Faeth. Evaporation and combustion of sprays. *Prog. Energy Comb. Sci.*, 9:1, 1983.

[35] G. M. Faeth. Mixing, transport and combustion in spray. *Prog. Energy Comb. Sci.*, 13:293, 1987.

[36] A. Fashola and C. P. Chen. Modeling of confined turbulent fluid-particle flows using eulerian and lagrangian schemes. *International Journal of Heat and Mass Transfer*, 33:691, 1990.

[37] N. Frossling. On the evaporation of falling droplets. *Gerlands Beltrage Zur Geophysik*, 52:170, 1938.

[38] M. A. Gonzalez and R. D. Reitz. A study of diesel cold starting using both cycle analysis and multidimensional calculations. SAE Technical Paper 910180, 1991.

[39] A. D. Gosman and E. Ioannides. Aspects of computer simulation of liquid fueled combustors. AIAA-81-0323, 1981.

[40] H. Hanjalic, B. E. Launder, and R. Schistel. Multiple-time-scale concepts in turbulent transport modeling. Proc. Turbulent Shear Flows, Vol.2, pp.10.31-10.36.

[41] F. H. Harlow and J. E. Welch. Numerical calculation of time dependent viscous incompressible flow with free surfaces. *Physics of Fluids*, 8(12):2182, 1965.

[42] A. Harten. High resolution schemes for hyperbolic conservation laws. *Journal of Computational Physics*, 49:357, 1983.

[43] H. Hiroyasu and T. Kadota. Fuel droplet size distribution in diesel combustion chamber. SAE Paper 740715.

[44] C.W. Hirt, B. D. Nichols, and N.C. Romero. SOLA - a numerical solution algorithm for transient fluid flows. Los Alamos Scientific Laboratory Report LA-5852, 1975.

[45] C.P. Chen H.M. Shang and Y. Jiang. Multiple-scale turbulence effects on an evaporating spray. Proc. of 6th Miami Int. Symp. on Heat and Mass Transfer, Ed. T.N. Veziroglu, Hemisphere, 1991.

[46] C.P. Chen H.M. Shang and Y. Jiang. Turbulence modulation effect on evaporating spray characterization. 26th Joint Propulsion Conference, Orlando, AIAA paper 90-2442, July, 1990.

[47] R. I. Issa. Solution of the implicitly discretised fluid flow equations by operator-splitting. *Journal of Computational Physics*, 62:40, 1985.

[48] R. I. Issa, B. Ahmadi-Befrui, K. R. Beshay, and A. D. Gosman. Solution of the implicitly discretised reacting flow equation by operator-splitting. *Journal of Computational Physics*, 93:388, 1991.

[49] R. I. Issa, A. D. Gosman, and A. P. Watkins. The computation of compressible and incompressible recirculating flows by a non-iterative implicit scheme. *Journal of Computational Physics*, 62:66, 1985.

[50] D. S. Jang, R. Jetliu, and S. Acharya. Comparison of the PISO, SIMPLER, and SIMPLEC algorithms for the treatment of the pressure-velocity coupling in steady flow problems. *Numerical Heat Transfer*, 10:209, 1986.

[51] S. D. Jang and H. H. Chiu. Theory of renormalized droplet: Ii non-steady vaporization of droplet in non-dilute sprays. AIAA-88-0639, AIAA 26th Aerospace Sciences Meeting, January 11-14, 1988/Reno, Nevada.

[52] T. L. Jiang and H. H. Chiu. Advanced modelling of spray combustion processes in airbreathing propulsion combustors. AIAA-87-0067, AIAA 25th Aerospace Sciences Meeting, January 12-15, 1987/Reno, Nevada.

[53] T. L. Jiang and H. H. Chiu. Theory of bipropellant combustion, part ii - conjugate, normal and composite combustion in a liquid propellant rocket combustion chamber. AIAA-86-0221, AIAA 24th Aerospace Sciences Meeting, January 6-9, 1986/Reno, Nevada.

[54] T. L. Jiang and W. J. Hsu. Comparison of droplet combustion models in spray combustion. AIAA-91-2203-CP.

[55] Y. Jiang. Ph. D. Dissertation, University of Alabama in Huntsville, in preparation.

[56] Y. Jiang, C. P. Chen, and H. M. Shang. A new pressure-velocity coupling procedure for inviscid and viscous flows at all speeds. Proc. of 4th International Symposium on Computational Fluid Dynamics, Sep. 9-12, 1991, Davis, California.

[57] W. P. Jones. Models for turbulent flows with variable density and combustion. in W. Kollman (ed.), Prediction Method for Turbulent Flows, Hemisphere Publishing, London, pp. 379-422, 1980.

[58] W. P. Jones and B. E. Launder. The prediction of laminarization with a two-equation model of turbulence. *International Journal of Heat and Mass Transfer*, 15, 1972.

[59] S. W. Kim and C. P. Chen. A multiple-time-scale turbulence model based on variable partitioning of the turbulent kinetic energy spectrum. *Numerical Heat Transfer*, 16:193, 1989.

[60] Y. M. Kim, C. P. Chen, and J. P. Ziebarth. Numerical simulation of combustion instability in liquid-fueled engines. AIAA-92-0775, 30th Aerospace Sciences Meeting and Exhibit, January, 1992/Reno,NV.

[61] Y. M. Kim, T. J. Chung, and K. S. Chang. Finite element model for turbulent spray combustion. AIAA 90-0359, 1990.

[62] Y. M. Kim, H. M. Shang, and C. P. Chen. Non-isotropic turbulence effects on spray combustion. AIAA-91-2196, 27th Joint Propulsion Conference, Sacramento, CA, June 24-26, 1991.

[63] Y. M. Kim, H. M. Shang, C.P. Chen, J.P. Ziebarth, and T. S. Wang. Numerical modelling in spray combustion. Proc. of 4th International Symposium on Computational Fluid Dynamics, Sep. 9-12, 1991, Davis, California.

[64] K. K. Kuo. *Principles of Combustion.* John Wiley & Sons, Inc., 1986.

[65] D. Kwak, J. L. C. Chang, S. P. Shanks, and S. R. Chakravarthy. A three dimensional incompressible navier-stokes solver using primitive variables. *AIAA Journal*, 23:390, 1985.

[66] B. R. Latimer and A. Pollard. Comparison of pressure-velocity coupling solution algorithms. *Numerical Heat Transfer*, 8:635, 1985.

[67] B. E. Launder. Second-moment closure and its use in modelling turbulent industrial flows. *International Journal for Numerical Methods in Fluids*, 9:963, 1989.

[68] B. E. Launder. Second-moment closure: Present... and future? *International Journal of Heat and Fluid Flow*, 10(4):282, 1989.

[69] B. E. Launder, G. J. Reece, and W. Rodi. Progress in the development of a reynolds stress turbulence closure. *Journal of Fluid Mechanics*, 68:537, 1975.

[70] B. E. Launder and D. B. Spalding. The numerical computation of turbulent flows. *Computer Methods in Applied Mechanics and Engineering*, 3:269, 1974.

[71] C. K. Law. Recent advances in droplet vaporization and combustion. *Prog. Energy Comb. Sci.*, 8:171, 1982.

[72] A. H. Lefebvre. *Atomization and Sprays.* Hemisphere Publishing Corporation, 1989.

[73] P.Y. Liang. ARICC-IJ user's manual. RI/RD89-235, Rocketdyne, A division of Rockwell International, August, 1989.

[74] R. J. Litchford and S. M. Jeng. On the efficiency of a statistical transport model for turbulent particle dispersion. to be appeared in AIAA J., 1992.

[75] R. J. Litchford and S. M. Jeng. Efficient statistical transport model for turbulent particle dispersion in sprays. *AIAA Journal*, 29(9):1443, 1991.

[76] B. F. Magnussen and B. H. Hjertager. On mathematical modeling of turbulent combustion with special emphasis on soot formation and combustion. 16th Symposium on Combustion, p. 719, 1977.

[77] L. Martinelli, R.D. Reitz, and F.V. Bracco. Comparison of computed and measured dense spray jets. 9th International Colloquium on Dynamics of Explosions and Reactive System, Poitiers, France, 1983.

[78] K. Meintjes. Engine combustion modeling: Prospects and challenges. *CRAY CHANNELS, Winter Issue*, page 12, 1987.

[79] R. Mellor, N. A. Chigier, and J. M. Beer. Pressure jet spray in air stream. ASME Paper 70-GT-101.

[80] A. A. Mostafa and H. C. Mongia. On the modeling of turbulent evaporating sprays: Eulerian versus lagrangian approach. *International Journal of Heat and Mass Transfer*, 30:2583, 1987.

[81] A.A. Mostafa and S.E. Elghobashi. A two-equation turbulence model for jet flows laden with vaporizing droplets. *International Journal of Multiphase Flow*, 11:515, 1985.

[82] A.A. Mostafa and H.C. Mongia. On the modeling of turbulent evaporation sprays: Eulerian versus lagrangian approach. *International Journal of Heat and Mass Transfer*, 30(12):2583, 1987.

[83] A.A. Mostafa and H.C. Mongia. On the interaction of particles and turbulent fluid flow. *International Journal of Heat and Mass Transfer*, 31(10):2063, 1988.

[84] J. D. Naber and R. D. Reitz. Modeling engine spray/wall impingement. SAE Technical Paper 880107, 1988.

[85] K. Nakabe, Y. Mizutani, S. Tanimura, and T. Hirao. Burning characteristics of premixed sprays in gas-liquid coburning mixtures. *Combustion and Flame*, 74:39, 1988.

[86] R. H. Nichols. The effect of particle dynamics on turbulence measurement withng characte the laser velocimeter. in Numerical Methods for Multiphase flows, ASME FED, Vol.91, ASME, New York, 1990, pp.35-45.

[87] P. J. O'Rourke. Collective drop effects on vaporizing liquid sprays. Los Alamos Scientific Laboratory Rept. LA-9069-T, 1981.

[88] P. J. O'Rourke. Statistical properties and numerical implementation of a model for droplet dispersion in a turbulent gas. *Journal of Computational Physics*, 83:345, 1989.

[89] P. J. O'Rourke and A. A. Amsden. The TAB method for numerical calculation of spray droplet breakup. SAE Technical Paper 870289 (1987).

[90] S. V. Patankar. *Numerical Heat Transfer and Fluid Flow.* Hemisphere, Washington, D.C., 1980.

[91] S. V. Patankar and D. B. Spalding. A calculation procedure for heat, mass, and momentum transfer in three-dimensional parabolic flows. *International Journal of Heat and Mass Transfer*, 15:1787, 1972.

[92] F. Pourahmadi and J.A.C. Humphrey. Modeling of solid-fluid turbulent flows with application to predicting erosive wear. *Int. J. Physicochem. Hydrodyn.*, 4:191, 1983.

[93] T. H. Pulliam and J. L. Steger. Recent improvements in efficiency, accuracy, and convergence for implicit approximate factorization algorithms. AIAA-85-0360, AIAA 23rd Aerospace Sciences Meeting, January 1985, Reno, NV.

[94] M. S. Raju and W. A. Sirignano. Multicomponent spray computations in a modified centerbody combustor. *Journal of Propulsion and Power*, 6:97, 1990.

[95] R. D. Reitz. Modeling atomization processes in high-pressure vaporizing sprays. in Atomization and Spray Technology, vol.3.

[96] R. D. Reitz and R. Diwakar. Effect of drop breakup on fuel sprays. SAE Technical Paper 860469 (1986).

[97] R. D. Reitz and R. Diwakar. Structure of high-pressure fuel sprays. SAE Technical Paper 870598 (1987).

[98] C. M. Rhie. A pressure based navier-stokes solver using the multigrid method. AIAA-86-0207, 1986.

[99] C. M. Rhie and S. T. Stowers. Navier-stokes analysis for high speed flows using a pressure correction algorithm. *Journal of Propulsion and Power*, Nov.-Dec.:564, 1988.

[100] W. Rodi. A new algebraic relation for calculating the reynolds stresses. *ZAMM*, 56:T219, 1976.

[101] P. L. Roe. Characteristic-based schemes for the euler equations. Annual Review of Fluid Mechanics, pp.337-356, 1986.

[102] P. L. Roe. Some contributions to the modeling of discontinuous flows. Lecture in Applied Mathematics, Vol. 22, 1985.

[103] J. S. Sabins and F. J. de Jong. Calculation of the two-phase flow in an evaporating spray using an eulerian-lagrangian analysis. AIAA-90-0447, 1990.

[104] See. Poc. int. conference on mechanics of two-phase flows,. Eds. S. L. Lee and F. Durst, Taipei, Taiwan, 1989.

[105] A. J. Shearer and E. G. Groff. Injection system effects on oscillating-poppet-injector sprays. Proceedings of the ASME Diesel and Gas Engine Power Division Conference, New York, 1984, pp. 33-42.

[106] W. Shi, M.-H. Chen, and C.-S. Sun. A pressure-based fmg/fas algorithm for flow at all speeds. AIAA-92-0548, 1992.

[107] J. S. Shuen. A theoretical and experimental investigation of dilute particle-laden turbulent gas jet. Ph. D. Dissertation, Pennsylvania State University, May, 1984.

[108] J. S. Shuen. Prediction of the structure of fuel sprays in cylindrical combustion chambers. *Journal of Propulsion*, 3(2):105, 1987.

[109] J. S. Shuen, L. D. Chen, and G. M. Faeth. Evaluation of a stochastic model of particle dispersion in a turbulent round jet. *AIChE Journal*, 29:167, 1983.

[110] J. S. Shuen, A. S. P. Solomom, Q. F. Zhang, and G. M. Faeth. Structure of particle-laden jets: Measurements and predictions. *AIAA Journal*, 23:396, 1985.

[111] J. S. Shuen, A.S.P. Solomon, and G.M. Faeth. Drop-turbulence interactions in a diffusion flame. *AIAA Journal*, 24:101, 1986.

[112] W. A. Sirignano. Fuel droplet vaporization and spray combustion. *Prog. Energy Comb. Sci.*, 9:291, 1983.

[113] W. H. Snyder and J. L. Lumley. Some measurements of particle velocity autocorrelation functions in a turbulent flow. *Journal of Fluid Mechanics*, 48:41, 1971.

[114] S. L. Soo. *Fluid Dynamics of Multiphase Systems.* Blaisdell Publishing Co., 1967.

[115] D.B. Spalding. Development of the eddy-breakup model of turbulent combustion. 16th Symposium on Combustion, p. 643.

[116] D. R. Stull and H. Prophet. JANAF thermochemical table, 2nd edition, n. w. chase et al. *J. Phys. Chem. Ref. Data*, 3:311, 1974.

[117] J. H. Tuttle, R. A. Shisler, and A. M. Mellor. Investigation of liquid fueled turbulent diffusion flames. *Combustion Science and Technology*, 14:229, 1976.

[118] L. H. J. Wachters and N. A. Westerling. The heat transfer from a hot wall to imping water drops in the spheroidal state. *Chem. Eng. Sci.*, 21:1047–1056, 1966.

[119] C. K. Westbrook and F. L. Dryer. Chemical kinetic modelling of hydrocarbon combustion. *Prog. Energy Comb. Sci.*, 10:1, 1984.

[120] K. J. Wu, D. A. Santavicca, and F. V. Bracco. LDV measurements of drop velocity in disel-type sprays. *AIAA Journal*, 22(9):1263–1270, 1984.

[121] H. Q. Yang, M. Z. Pindera, A.J. Przekwas, and K. Tucker. A study of pressure-based methodology for resonant flows in non-linear combustion instabilities. AIAA-92-0779, 30th Aerospace Sciences Meeting and Exhibit, January, 1992/Reno,NV.

[122] H. Yokota, T. Kamimoto, and H. Kobayashi. A study of disel spray and flame by an image processing technique. *Bulletin of JSME*, 54:71, 1988.

[123] S. Yuu, N. Yasukouchi, Y. Hirosawa, and T. Jotaki. Particle turbulent diffusion in a dust laden round jet. *AIChE Journal*, 24(3):509, 1974.

[124] Q. Zhou and S. C. Yao. Group modeling of impacting spray dynamics. *International Journal of Heat and Mass Transfer*, 35(1):121, 1992.